

PRECISION ATTITUDE CONTROL OF SYMMETRIC SPINNING BODIES

by
Kenneth R. Lorell
Benjamin Lange

April 1971

Approved for public release;
distribution unlimited.

SUDAAR No. 422

This work was performed for
United States Air Force
Air Force Avionics Laboratory
Wright-Patterson AFB, Ohio 45433
under
Contract F33615-70-C-1637

~~Department of Aeronautics and Astronautics~~
Stanford University
Stanford, California

Contrails

FOREWORD


The work reported here was performed under Contracts F33615-67-C-1245 and F33615-70-C-1637, Project 5102, Task 510215 at the Center for Systems Research, Guidance and Control Laboratory, Stanford, California.

This report has been issued as Department of Aeronautics and Astronautics document SUDAAR NO. 422.

This program is monitored by Mr. H. P. Kohlmann, Air Force Avionics Laboratory (AFAL/NVE).

Publication of this report does not constitute Air Force approval of the report's findings or conclusions. It is published only for the exchange and stimulation of ideas.

This technical report has been reviewed and is approved for publication.



WILLIAM J. DELANEY
Lt Colonel, USAF
Chief, Navigation &
Guidance Division

Contrails

ABSTRACT

Motivated by the arc-second pointing requirement of the Unsupported Gyroscope experiment and other satellite applications, this research investigates the problems associated with the precision attitude control of symmetric spinning bodies. An attitude control system is synthesized and then is studied by analog simulation. Controller performance and limitations are evaluated, using a laboratory model called the Spinning Vehicle Simulator (SVS).

A technique devised at Stanford University in 1966 that simplifies the design of spinning-vehicle attitude controllers is used to select controller gains. The resulting system, simulated on an analog computer, produces excellent response characteristics and is insensitive to vehicle parameter or gain changes. The magnitude of the attitude error is shown to have zero-frequency and spin-frequency components proportional to the magnitude of body-fixed and inertially fixed moments, respectively.

An Automatic Mass Trim System (AMTS), consisting of two pairs of masses that move on axes parallel to the nominal spin axis, is proposed as a means of eliminating zero-frequency attitude errors caused by moments fixed in the body and sensor-vehicle misalignments. By correctly positioning the trim masses, a moment (or a product of inertia) is created to compensate for the disturbance (or misalignment). The equations of motion for a spinning rigid body with internal moving masses are developed and used to analyze the trim system. A series of root loci, plotted for the attitude-stabilized vehicle with an AMTS, is the basis for trim-system gain selection.

The laboratory portion of the investigation deals with two problems: first, mechanization of the attitude controller and AMTS and second, determination of those factors that limit control-system performance. A spinning-vehicle attitude controller on a three-degree-of-freedom spherical air bearing was developed, which damps large initial conditions, acquires a laboratory reference mirror (for the autocollimator used as an attitude sensor), maintains precision attitude control during CMG momentum dumping, and automatically trims the effects of body-fixed moments and sensor-vehicle misalignments. The effects of sensor

Contrails

noise, electronic noise, and the laboratory environment on the control system were measured.

A pointing accuracy of ± 2.5 arc seconds was achieved. An analysis of error sources indicates that the laboratory environment (including torques from gravity effects, air bearing, earth rate, and air currents) is the major factor in limiting the system. By extrapolating these results using previously developed disturbance torque models, the performance of a controller similar to that used on the SVS is predicted for the orbital environment.

Contrails

CONTENTS

	<u>Page</u>
I. INTRODUCTION	1
A. Statement of Problem	1
B. Description of Experiment	2
C. Previous Related Results	3
D. Contributions of this Research	5
II. EQUATIONS OF MOTION	7
A. Equations of Motion of a Spinning Body with Internal Moving Masses	7
B. Equations of Motion of a Rotating Two-Degree- of-Freedom Gyroscope	19
1. The Gyro as an Attitude Reference	23
2. The Gyro as a CMG	26
C. Output Equations of a Rotating Two-Axis Autocollimator	28
III. DESIGN OF A PRECISION ATTITUDE CONTROLLER FOR A SYMMETRIC SPINNING BODY	33
A. Similarities between a Gyrostat Controller and a Spinning-Vehicle Control Law Derived from Frequency Symmetry	33
B. Control of an Automatic Mass Trim System	39
C. Controller Stability with Saturation Nonlinearities	49
IV. DESCRIPTION OF EXPERIMENT	57
A. Simulator Description and Experimental Setup	57
1. Description of Simulator	57
2. Experimental Setup	60
B. Controller Mechanization	62
1. Dynamic Range and Multiple Control-Loop Operation	62
2. Controller Components	63
3. Modes of Operation	65
C. Two-Degree-of-Freedom Control Moment and Vertical Reference Gyroscope	67
1. Attitude Sensing	67
2. Control Torquing	73

CONTENTS (Cont)

	<u>Page</u>
D. Two-Axis Autocollimator	75
1. Requirements	75
2. Optics	75
3. Electronics	78
E. Gas-Jet System	80
F. Automatic Mass Trim System	81
1. Mechanical Components	81
2. Electronics	81
3. Operation	82
G. Electronic Subsystem	82
1. Main Electronics Rack	83
2. Power Supplies	85
3. External Equipment	85
V. EXPERIMENTAL RESULTS	87
A. SVS Performance in the Laboratory Environment	87
1. Normal Operation	87
2. Operation without Automatic Mass Trimming	90
3. Conclusions	90
B. Electronic Noise	92
1. Autocollimator Noise	92
2. Combined Electronics and Autocollimator Noise	92
3. Conclusions	92
C. Environmental Disturbances	96
1. Sources of Disturbing Moments	96
2. Conclusions	97
D. Extrapolation of Laboratory Results to Performance in the Orbital Environment	99
VI. CONCLUSIONS	101
A. Conclusions	101
1. Design of Precision Attitude Controllers for Spinning Vehicles	101
2. Laboratory Performance of the Control System	101
B. Recommendations	102
1. Improvements in Existing Techniques and Equipment	102
2. Areas for Further Investigation	102

Contrails

CONTENTS (Cont)

	<u>Page</u>
Appendix. SPECIFICATIONS OF THE SPINNING VEHICLE SIMULATOR . . .	105
REFERENCES	125
ADDITIONAL BIBLIOGRAPHY	126

Contrails

ILLUSTRATIONS

<u>Figure</u>	<u>Page</u>
1. Body-fixed coordinate system and coordinates for an internal moving mass	10
2. Geometry of vertical moving masses	12
3. Components of \vec{a} in body coordinates	18
4. Two-degree-of-freedom gyroscope	20
5. Two-axis autocollimator	29
6. Symmetric gyrostat	34
7. Spinning-vehicle controller simulation without disturbing moments	40
8. Spinning-vehicle controller simulation with body-fixed and inertial disturbing moments	40
9. Root locus of characteristic equation of (3.14) vs K_M	43
10. Root locus of characteristic equation of (3.14) vs K_M	44
11. Root locus of characteristic equation of (3.14) vs K_M	45
12. Root locus of characteristic equation of (3.14) vs K_M	46
13. Automatic mass trim system response	47
14. Root locus of characteristic equation of (3.14) vs K_M without attitude control loop	48
15. Effect of torquer saturation on K_p	50
16. Root locus of characteristic equation of (3.14) vs K_M with $K_p = 1.44 \text{ sec}^{-1}$ to approximate controller torque saturation at $\gamma = 200$ arc seconds	51
17. Root locus of characteristic equation of (3.14) vs K_M with $K_p = 0.144 \text{ sec}^{-1}$ to approximate controller torque saturation at $\gamma = 2000$ arc seconds	52
18. Root locus of characteristic equation of (3.14) vs K_M with $K_p = 0.144 \text{ sec}^{-1}$	53
19. Nonlinear control-system computer simulation	54
20. Automatic mass trim system response	55

ILLUSTRATIONS (Cont)

<u>Figure</u>		<u>Page</u>
21.	Cutaway view of spinning vehicle simulator	58
22.	Spinning vehicle simulator	59
23.	Spinning vehicle simulator and support equipment	61
24.	Coarse erection loop	68
25.	Fine erection loop	69
26.	Fine control loop	70
27.	Automatic mass trim system control loop	71
28.	Gyro unload loop	72
29.	Kearfott T4101 vertical gyro and power amplifier	74
30.	Autocollimator used on the spinning vehicle simulator	76
31.	Cross section of autocollimator	77
32.	End-on view of autocollimator sensing head	78
33.	Block diagram of autocollimator electronics	79
34.	Main electronics rack	84
35.	Telemetry output during typical SVS operation	88
36.	Telemetered autocollimator output during SVS mode-4 operation	89
37.	Telemetered autocollimator output during SVS mode-4 operation; AMTS off	91
38.	Power spectrum of autocollimator signal	93
39.	Autocollimator noise equivalent angle	94
40.	Attitude error signal, no environmental disturbances	94
41.	Hybrid simulation	95
42.	Power spectra of attitude error signals	98
43.	External control box	113

Contracts

ILLUSTRATIONS (Cont)

<u>Figure</u>		<u>Page</u>
44.	Vehicle control panel	116
45.	Sequencing logic	120
46.	High-thrust loop	121
47.	AMTS loops	122
48.	Low-thrust loops	123
49.	Gyro loops	124

TABLES

<u>Number</u>		
1.	Spinning vehicle simulator, mode definitions	64
2.	Laboratory disturbance sources	99
3.	Notation for sequencing logic	119

Contrails

Contrails

LIST OF SYMBOLS

A	ratio of bearing-friction coefficient to gyro-spin angular momentum f/h
a	time constant of AMTS spin-frequency filter
\vec{a}	eigenvector of moment of inertia tensor \vec{I}
$a_{x,y,z}$	components of \vec{a}
$b_{x,y}$	misalignment between synchro null and vehicle axis of maximum inertia
\vec{E}	unit tensor
E_s	Schmitt trigger pulse magnitude
E_T	Schmitt trigger "ON" threshold
e_i	input to PWWF modulator
e_o	output of PWWF integrator
e_r	output of PWWF modulator
f	coefficient of viscous bearing friction
g	magnitude of acceleration caused by gravity
\vec{H}	system angular momentum
\vec{H}_m	angular momentum of internal moving masses
$\vec{H}_{IG}, H_{IGx,y,z}$	angular momentum of gyro inner gimbal
$\vec{H}_{OG}, H_{OGx,y,z}$	angular momentum of gyro outer gimbal
h	$ \vec{h} $
\vec{h}	spin angular momentum
\vec{I}	moment of inertia tensor

Contrails

I_{ij}	$i, j = x, y, z$	elements of \vec{I} (moments and products of inertia)
I_s		spin axis (maximum) moment of inertia
I_t		transverse (intermediate) moment of inertia
$I_{IGx, y, z}$		gyro inner-gimbal principal moments of inertia
$I_{OGx, y, z}$		gyro outer-gimbal principal moments of inertia
I_{ws}, I_{wt}		gyro wheel spin axis and transverse axis moments of inertia
$j_{1, 2, 3, 4}$		light intensity on autocollimator sensing head
j		$\sqrt{-1}$
K_{ac}		autocollimator scale factor
K_M		acceleration gain for AMTS loop
$K_p, K_{PA}, K_{PG}, K_\delta$		position gains
$K_v, K_{VA}, K_{VG}, K_\rho$		velocity gains
K_T		scale factor
K_U		CMG unload-loop gain
K_{xc}, K'_{xc}		cross-coupling gain
$\vec{M}, M_{x, y}$		moment
$\vec{M}_C, M_{Cx, y}$		control moments
$\vec{M}_{DB}, M_{DBx, y}$		disturbing moments fixed in the body
$\vec{M}_{DI}, M_{DIx, y}$		disturbing moments fixed in the laboratory
$\vec{M}_{IG}, \vec{M}_{OG}, M_{IGx, y}, M_{OGx, y}$		moments applied to the gyro inner and outer gimbals

Contrails

m	moment of inertia ratio $(I_s - I_t)/I_t$
m_i	mass of particle i
n	moment of inertia ratio I_s/I_t
$P_{1,2,3,4}$	autocollimator preamp outputs
$\vec{Q}, Q_{x,y}$	ratio \vec{M}/I_t
$\vec{Q}_C, Q_{Cx,y}$	ratio \vec{M}_C/I_t
$\vec{Q}_D, \vec{Q}_{DB}, \vec{Q}_{DI}$	ratios $\vec{M}_D/I_t, \vec{M}_{DB}/I_t, \vec{M}_{DI}/I_t$
Q_T	$2\mu R\beta^2/I_t$
R	distance of movable mass in X_B-Y_B plane from vehicle symmetry axis
\vec{r}, r_x, r_y, r_z	radius vector and components
S	Laplace variable
t	time
t_{ON}, t_{OFF}	PWPF "on" and "off" pulse duration
v_i	velocity of particle i
W	PWPF pulse width
X_B, Y_B, Z_B	axes of an orthogonal coordinate system fixed in the body
X_I, Y_I, Z_I	axes of an orthogonal coordinate system fixed in inertial space
X_{IG}, Y_{IG}, Z_{IG}	axes of an orthogonal coordinate system fixed in the gyro inner gimbal
X_{OG}, Y_{OG}, Z_{OG}	axes of an orthogonal coordinate system fixed in the gyro outer gimbal

Contrails

x_i, y_i, z_i	position of particle i
$Z_{x,y}, Z_{x+}, Z_{x-}, Z_{y+}, Z_{y-}$	vertical distance of the $\pm x$ and $\pm y$ AMTS trim masses from the $X_B - Y_B$ plane
$\alpha_{x,y}$	misalignment between autocollimator null axis and vehicle axis of maximum inertia
β	spin angular velocity
$\gamma_{x,y}$	autocollimator (star-tracker) attitude angles for a spinning vehicle (measured)
$\gamma'_{x,y}$	$\gamma_{x,y} + \alpha_{x,y}$
$\delta_{x,y}$	gyro gimbal angles (measured)
$\delta'_{x,y}$	$\delta_{x,y} + b_{x,y}$
$\zeta_{1,2}$	damping coefficients
$\eta_{x,y}$	autocollimator (star tracker) attitude angles for a gyrostat
θ	$\tan^{-1} a_y/a_x$
μ	mass of one AMTS trim mass
ν	PWPF frequency
$\xi_{x,y}$	$\eta_{x,y}$ transformed into rotating coordinates
ρ	$ \vec{a} \tan \phi$
σ	variable of integration (time)
τ	torque
ϕ	$\cos^{-1} a_z/ \vec{a} $
$\omega_{x,y,z}$	angular velocity components along body x, y, z axes

Contrails

$\vec{\omega}^{B-I}, \vec{\omega}^{IG-OG},$ $\vec{\omega}^{OG-B}, \vec{\omega}^{IG-I}, \vec{\omega}^{OG-I}$	angular velocities of body and inner and outer gimbal frames
$\omega^{IGx, y, z}$	components of $\vec{\omega}^{IG-I}$
$\omega^{OGx, y, z}$	components of $\vec{\omega}^{OG-I}$
$\omega_{n1, 2}$	gyro nutation frequencies
$(\vec{\quad})$	vector
$(\vec{\vec{\quad}})$	tensor
$\overset{I}{(\dot{\vec{\quad}})}$	time derivative of vector in inertial frame
$\overset{B}{(\dot{\vec{\quad}})}$	time derivative of vector in body frame
$\overset{IG}{(\dot{\vec{\quad}})}$	time derivative of vector in gyro inner-gimbal frame
$\overset{OG}{(\dot{\vec{\quad}})}$	time derivative of vector in gyro outer-gimbal frame
$\vec{\omega}^{A-B}$	angular velocity of frame A with respect to frame B
$(\vec{\quad}) \times (\vec{\quad})$	cross product
$ (\quad) $	absolute value of a quantity
$(\dot{\quad})$	time derivative of a quantity

Contrails

ACKNOWLEDGMENT

The author is indebted to his advisor, Professor Benjamin Lange, for his continued support and encouragement during the course of this research. The advice and constructive criticism of Professor Daniel DeBra and the thorough review of the manuscript by Professor Donald Baganoff are also greatly appreciated. The author is particularly grateful to Mr. David Steelman for his design of the electronic system and to the late Mr. James Mathiesen for his consultation on numerous mechanical design problems. Special thanks go to Richard Van Patten, Robert Clappier, Geoffrey Jones, and Robert Kaltenberg for assistance in building the electronics and to Howard Frosch, Gerard DeWerk, Leslie Fisher, and Karl Neumacher for their craftsmanship in constructing the mechanical portion of the apparatus. Appreciation is also extended to the many friends and associates at Stanford University whose assistance and helpful suggestions were invaluable.

This research was carried out under Air Force Contracts F33615-67-C-1245 and F33615-70-C-1637. Particular gratitude is expressed for the financial support provided by the Air Force and the Guidance and Control Laboratory.

Contrails

Chapter I

INTRODUCTION

A. Statement of Problem

An experiment has been proposed by Lange [1,2] to study the random drift performance of an unsupported gyroscope in earth orbit. By operating the satellite in the drag-free mode,[†] all support forces, and hence the primary sources of random drift, can be eliminated from the gyro rotor. Drift performance of this gyroscope is predicted to be from five to six orders of magnitude better than the current state of the art.

Rotor drift is measured by comparing the angle between a "fixed" star and the position of an optical flat on the rotor, located perpendicular to the axis of maximum inertia. To point a telescope at the stellar reference, the attitude of the satellite must be controlled with a precision on the order of 1 arc second. The satellite is spun because frequency separation of instrument bias errors is necessary to attain the precision required for the experiment. The benefits of a single-axis control system and the inherent stability of a gyroscope also result from spinning the satellite.

In addition to the unsupported gyroscope, other satellite applications also demand precision attitude control. Weather satellites that point cameras at small sections of the earth's surface, satellites that communicate with a ground station or another satellite using a narrow laser beam, space astronomy satellites, and earth resources satellites that pinpoint geographical features all may require a pointing accuracy of 1 arc second or less.

Motivated by the need for precision attitude control in the Unsupported Gyroscope experiment as well as in other satellite applications,

[†] A drag-free satellite has a proof mass inside an internal cavity and is controlled in translation so that the proof mass never touches the cavity walls. The outer satellite thus follows the proof mass which, because it is shielded from all external forces, flies a "drag free" orbit.

the problem addressed by this investigation is the design of a precision-pointing system for a spinning satellite. Using a laboratory simulator, it includes an examination of those factors limiting control-system performance.

B. Description of Experiment

To test the theoretical work accomplished regarding control-system design and to study the problems and limitations of precision attitude control, a laboratory model called the Spinning Vehicle Simulator (SVS) was constructed. The SVS consists of a framework to which the components of the attitude control system are attached. The vehicle is supported at its center of mass by a spherical air bearing that provides three degrees of rotational freedom and simulates the gravity-free orbit environment. The simulator spins about its symmetry axis, and the control system attempts to align this axis with the perpendicular to a reference mirror fixed in the laboratory.

In typical operation, the attitude error varies from initial conditions of 0.1 rad to a steady-state value of 10^{-5} rad (2.0 arc seconds). The problem of controlling over this large dynamic range was solved by introducing five modes of control. The sensors and actuators are changed according to the mode of the controller; each new mode is selected as the limitation of the operating range of the current mode is reached.

A two-axis vertical gyro is employed for coarse attitude sensing. When the attitude error is damped below 0.02 rad, a two-axis autocollimator can acquire the laboratory reference mirror. The autocollimator is employed for attitude information during the remaining modes of controller operation.

The large control torques necessary to damp initial conditions are provided by electrically controlled gas jets. Because the simulator is intended to demonstrate the capability of long-term precision control, continual expulsion of gas by control jets would be impractical. For this reason, torquing during precision control is done by a Control Moment Gyroscope (CMG) which is the same two-axis vertical gyro previously used as an attitude sensor. CMG momentum dumping is accomplished

by simultaneously torquing the gyro and firing gas jets, a process that results in a net zero torque on the vehicle.

Moments fixed in the body, which would ordinarily cause a steady-state attitude error, are eliminated by an automatic trim system. This system consists of four movable masses whose positions are controlled to provide an equal and opposite offset to any body-fixed torques. The trim system also makes the controller insensitive to misalignments between the axis of maximum inertia and the sensor null axis. Moving the internal masses causes the principal axes of inertia to move relative to the body; thus, the maximum inertia axis can be aligned with the sensor axis by the correct location of the trim masses.

Experimental data are obtained from a five-channel telemetry system on the simulator. These data are displayed in real time on a multichannel strip-chart recorder.

C. Previous Related Results

Since the early 1960's, numerous papers have discussed the dynamics of spinning axisymmetric bodies and the problem of designing attitude control systems for spinning satellites. Typically, control mechanization is analyzed theoretically and performance is obtained through computer simulations. Other papers are more general in their analysis and deal solely with the attitude motion; the type of control is unspecified. Laboratory simulators have been constructed and used primarily to study the relationship between control-system parameters and vehicle inertial properties.

An early paper by Cole, Ekstrand, and O'Neil [3] describes the attitude motions of rigid spinning axisymmetric bodies. Kane and Barba [4] and Wallace and Meirovitch [5] examine the theory of spinning satellites in elliptic orbits and analyze the full nonlinear equations of motion to determine the regions of stability. Hughes [6] also investigates the theoretical advantages of spin-stabilizing a satellite.

Control systems using CMGs as the source of control torque have been proposed by a number of authors. Lange, Fleming, and Parkinson [7] devised a unique method of obtaining the control law for a spinning vehicle

Contrails

and use it to design a controller with a CMG. Mingori and Kane [8] discuss the dynamics of a spinning satellite stabilized by gyroscopic devices and investigate the parameters governing the stability of the coupled bodies and the maximizing of damping rates. Chang and Yarber [9] and Jacot and Liska [10] also discuss the theoretical aspects of CMGs used to control spinning bodies. References 8 and 9 include computer simulations of the full nonlinear equations.

Numerous other authors [11,12,13,14] propose CMGs as actuators. Although Sarnecki [15] claims accuracies of "a fraction of a degree" for an analog simulation of a reaction jet controller, Sorenson [11] points out that true precision control (10 arc second pointing error or less) is accomplished usually by employing CMGs, momentum wheels, or magnetic torquing.

Mechanization schemes for precision attitude controllers, using coils to torque against the earth's magnetic field, were presented by Wheeler [16] and Sorenson [11]. Sorenson computes the orbital disturbing forces caused by aerodynamic, solar radiation, gravity gradient, and magnetic effects and predicts 0.01 arc second performance for his design.

Experimental work has been performed to verify various control mechanizations and to study the controlled vehicle dynamics. Adams [17] and Kurzhals and Adams [13] built simulators to investigate the relationship between controlled behavior and the vehicle inertia ratios; no attempt was made at precision control. After studying the use of CMGs for spinning and nonspinning vehicles, Jacot and Liska [10] constructed a twin CMG controller. Using a novel suspension to eliminate cross-coupling effects, they obtained ± 0.15 arc second laboratory performance for their nonspinning control system.

The effects of internal moving masses on spinning bodies have been examined. Rossi et al [18] and Kane [19] investigated instabilities resulting from small oscillating internal masses. Michelini et al [20] analyzed the sloshing of fuel in spinning satellites and found a quasi-steady-state solution and conditions for which oscillations can be induced in a body with no initial angular rates. Kurzhals and Adams [13] included a small oscillating mass in their vehicle to

simulate a man walking inside a rotating space station. Adams [17] used manually adjustable masses to change the inertia ratio of his simulator and to create products of inertia. The author knows of no previous analytical or experimental work dealing with an automatic mass trim system.

D. Contributions of this Research

Contributions of this research fall into two categories: (1) analysis of the control problem and synthesis of a theoretical controller and (2) laboratory mechanization of the controller, its experimental demonstration, and an investigation of the factors limiting its performance.

New results in the first category are

- (1) a study of the effects of internal moving masses on the dynamics of a symmetric spinning body, specialized to the geometry of the Spinning Vehicle Simulator
- (2) an interpretation of the Frequency Symmetry control-law synthesis technique, using the transformation of gyrostat gains
- (3) synthesis of a controller that eliminates the effects of body-fixed moments and sensor-vehicle misalignments

In the second category, the new results are

- (1) experimental verification of the Frequency Symmetry design technique
- (2) demonstration of an automatic mass trim system that eliminates the effects of dynamic imbalance and sensor-vehicle misalignments
- (3) design, construction, and demonstration of a two-axis autocollimator suitable for precision attitude control applications
- (4) demonstration of the precision attitude control of a symmetric spinning body with an average error of 2.5 arc seconds in the laboratory environment

Contrails

- (5) development of a controller that maintains precision attitude control during CMG momentum dumping, including a technique for calibrating gas-jet and gyro torques
- (6) development of a multimode attitude controller with an error-signal dynamic range of 10^4
- (7) investigation of problems of an actual spinning satellite controlled to a 0.1 to 5.0 arc second pointing accuracy and an extrapolation of laboratory results to performance in the orbital environment

Chapter II

EQUATIONS OF MOTION

The equations of motion of a spinning body with internal moving masses are derived in Section A, followed by simplifying assumptions that lead to a linear model. In Section B, the equations of a rotating two-degree-of-freedom gyroscope are derived, and the model is modified to cover both the attitude-sensor and control-actuator cases. The output equations of a rotating two-axis autocollimator are presented in Section C.

A. Equations of Motion of a Spinning Body with Internal Moving Masses

The equations of motion of a rigid spinning body are

$$\overset{I}{\vec{H}} = \overset{B}{\vec{H}} + \vec{\omega}^{B-I} \times \vec{H} \quad (2.1)$$

where

$\vec{H} \triangleq$ system angular momentum

$\vec{\omega}^{B-I}$ = angular velocity of the body, relative to inertial space

For a rigid body, \vec{H} also can be written as $\vec{H} = \vec{I} \cdot \vec{\omega}^{B-I}$, where \vec{I} is a diagonal matrix when the principal axes of inertia are the coordinate system of the body. This substitution leads to the classical Euler equations.

When the body is not rigid, \vec{H} is no longer equal to $\vec{I} \cdot \vec{\omega}^{B-I}$. Because \vec{H} is formally defined as

$$\vec{H} \triangleq \sum_{i=1}^n \vec{r}_i \times m_i \overset{I}{\vec{r}}_i$$

Contrails

and

$$\vec{r}^I = \vec{r}^B + \vec{\omega}^{B-I} \times \vec{r}^I$$

(where $\vec{r}^B \neq 0$ for a nonrigid body), a term must be added to $\vec{I} \cdot \vec{\omega}^{B-I}$ to account for the angular momentum of the mass inside the body, moving relative to some arbitrary body-fixed coordinate system. An equation first given by Liouville in 1858 [21], and used by geophysicists to describe the motion of the earth with its nonrigid crust, defined this additional angular momentum as

$$\vec{H}_m \triangleq \sum_{i=1}^n \vec{r}_i \times m_i \vec{r}_i^B \quad (2.2)$$

The system angular momentum becomes

$$\vec{H} = \vec{I} \cdot \vec{\omega}^{B-I} + \vec{H}_m \quad (2.3)$$

and

$$\vec{H} = \vec{I} \cdot \vec{\omega}^{B-I} + \vec{I} \cdot \vec{\omega}^{B-I} + \vec{\omega}^{B-I} \times \vec{I} \cdot \vec{\omega}^{B-I} + \vec{H}_m + \vec{\omega}^{B-I} \times \vec{H}_m \quad (2.4)$$

where the components of \vec{I} are

$$\begin{bmatrix} I_{xx} & I_{xy} & I_{xz} \\ I_{yx} & I_{yy} & I_{yz} \\ I_{zx} & I_{zy} & I_{zz} \end{bmatrix}$$

As a result, additional terms in (2.4) not found in (2.1) arise because of \vec{H}_m and the fact that \vec{I} is no longer diagonal or constant with time.

Contrails

The full equations of motion are obtained by expanding Eq. (2.4) coordinatized in the body, as shown in Fig. 1.

$$\begin{aligned}
 M_{Bx} &= \dot{I}_{xx} \omega_x + \dot{I}_{xy} \omega_y + \dot{I}_{xz} \omega_z + I_{xx} \dot{\omega}_x + I_{xy} \dot{\omega}_y + I_{xz} \dot{\omega}_z + (I_{zz} - I_{yy}) \omega_y \omega_z \\
 &\quad + (I_{zx} \omega_x + I_{zy} \omega_y) \omega_y - (I_{yx} \omega_x + I_{yz} \omega_z) \omega_z + \dot{H}_{mx} + H_{mz} \omega_y - H_{my} \omega_z \\
 M_{By} &= \dot{I}_{yx} \omega_x + \dot{I}_{yy} \omega_y + \dot{I}_{yz} \omega_z + I_{yx} \dot{\omega}_x + I_{yy} \dot{\omega}_y + I_{yz} \dot{\omega}_z + (I_{xx} - I_{zz}) \omega_x \omega_z \\
 &\quad + (I_{xy} \omega_y + I_{xz} \omega_z) \omega_z - (I_{zx} \omega_x + I_{zy} \omega_y) \omega_x + \dot{H}_{my} + H_{mx} \omega_z - H_{mz} \omega_x \\
 M_{Bz} &= \dot{I}_{zx} \omega_x + \dot{I}_{zy} \omega_y + \dot{I}_{zz} \omega_z + I_{zx} \dot{\omega}_x + I_{zy} \dot{\omega}_y + I_{zz} \dot{\omega}_z + (I_{yy} - I_{xx}) \omega_x \omega_y \\
 &\quad + (I_{yx} \omega_x + I_{yz} \omega_z) \omega_x - (I_{xy} \omega_y + I_{xz} \omega_z) \omega_y + \dot{H}_{mz} + H_{my} \omega_x - H_{mx} \omega_y
 \end{aligned} \tag{2.5}$$

The relationship between Eqs. (2.5) and the rigid body equations can be seen by separating the terms caused by the products of inertia and the dynamics of mass motion. For the products of inertia,

$$\begin{bmatrix} M_{PIx} \\ M_{PIy} \\ M_{PIz} \end{bmatrix} = \begin{bmatrix} I_{xy} \dot{\omega}_y + I_{xz} \dot{\omega}_z + (I_{zx} \omega_x + I_{zy} \omega_y) \omega_y - (I_{yx} \omega_x + I_{yz} \omega_z) \omega_z \\ I_{yx} \dot{\omega}_x + I_{yz} \dot{\omega}_z + (I_{xy} \omega_y + I_{xz} \omega_z) \omega_z - (I_{zx} \omega_x + I_{zy} \omega_y) \omega_y \\ I_{zx} \dot{\omega}_x + I_{zy} \dot{\omega}_y + (I_{yx} \omega_x + I_{yz} \omega_z) \omega_x - (I_{xy} \omega_y + I_{xz} \omega_z) \omega_y \end{bmatrix} \tag{2.6}$$

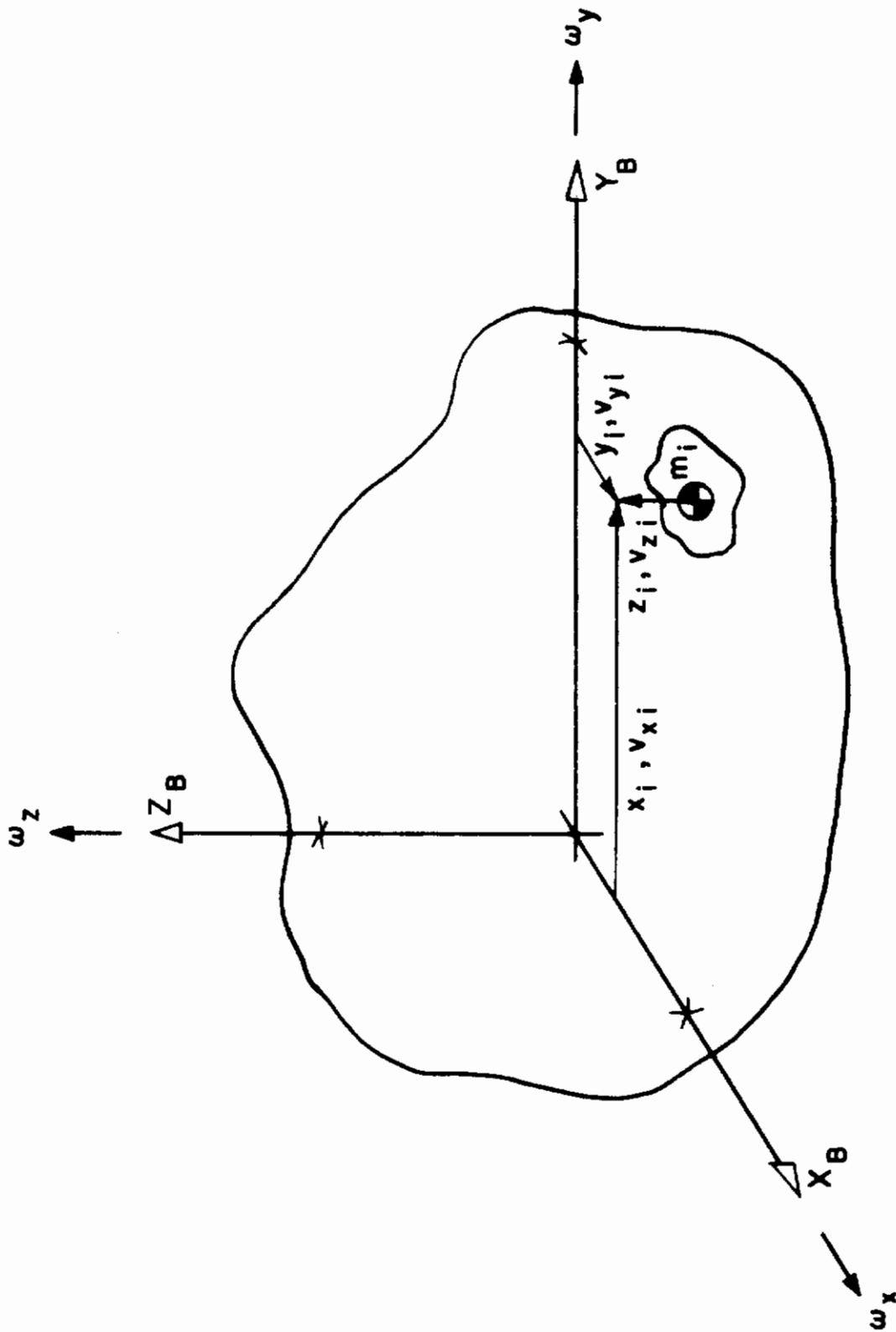


Fig. 1. BODY-FIXED COORDINATE SYSTEM AND COORDINATES FOR AN INTERNAL MOVING MASS.

and for the dynamics of mass motion,

$$\begin{bmatrix} M_{MDx} \\ M_{MDy} \\ M_{MDz} \end{bmatrix} = \begin{bmatrix} \dot{I}_{xx} \omega_x + \dot{I}_{xy} \omega_y + \dot{I}_{xz} \omega_z + \dot{H}_{mx} + H_{mz} \omega_y - H_{my} \omega_z \\ \dot{I}_{xy} \omega_x + \dot{I}_{yy} \omega_y + \dot{I}_{yz} \omega_z + \dot{H}_{my} + H_{mx} \omega_z - H_{mz} \omega_x \\ \dot{I}_{xz} \omega_x + \dot{I}_{yz} \omega_y + \dot{I}_{zz} \omega_z + \dot{H}_{mz} + H_{my} \omega_x - H_{mx} \omega_y \end{bmatrix} \quad (2.7)$$

Thus, Eqs. (2.5) become

$$\begin{bmatrix} M_{Bx} - M_{PIx} - M_{MDx} \\ M_{By} - M_{PIy} - M_{MDy} \\ M_{Bz} - M_{PIz} - M_{MDz} \end{bmatrix} = \begin{bmatrix} I_{xx} \dot{\omega}_x - (I_{yy} - I_{zz}) \omega_y \omega_z \\ I_{yy} \dot{\omega}_y - (I_{zz} - I_{xx}) \omega_x \omega_z \\ I_{zz} \dot{\omega}_z - (I_{xx} - I_{yy}) \omega_y \omega_x \end{bmatrix} \quad (2.8)$$

The right side of (2.8) is Euler's equations for a rigid spinning body, and the left side can be thought of as a forcing function arising from the nonrigid property.

By making a set of assumptions regarding the inertial properties of the vehicle and the geometry of the moving masses, Eq. (2.8) can be simplified considerably. With reference to Fig. 2 and Chapter I.B, the following assumptions can be made.

- (1) The vehicle, without trim masses, is axisymmetric:
 $I_{xx} = I_{yy} = I_t \quad I_{zz} = I_s \quad I_s > I_t.$
- (2) $I_{yz}/I_t, I_{xz}/I_t$ are first-order small.
- (3) The axis of travel of the internal moving masses is parallel to the nominal spin (maximum inertia) axis.
- (4) The moving masses are located along the two nominal intermediate axes of inertia at equal distances R from the vehicle spin axis.

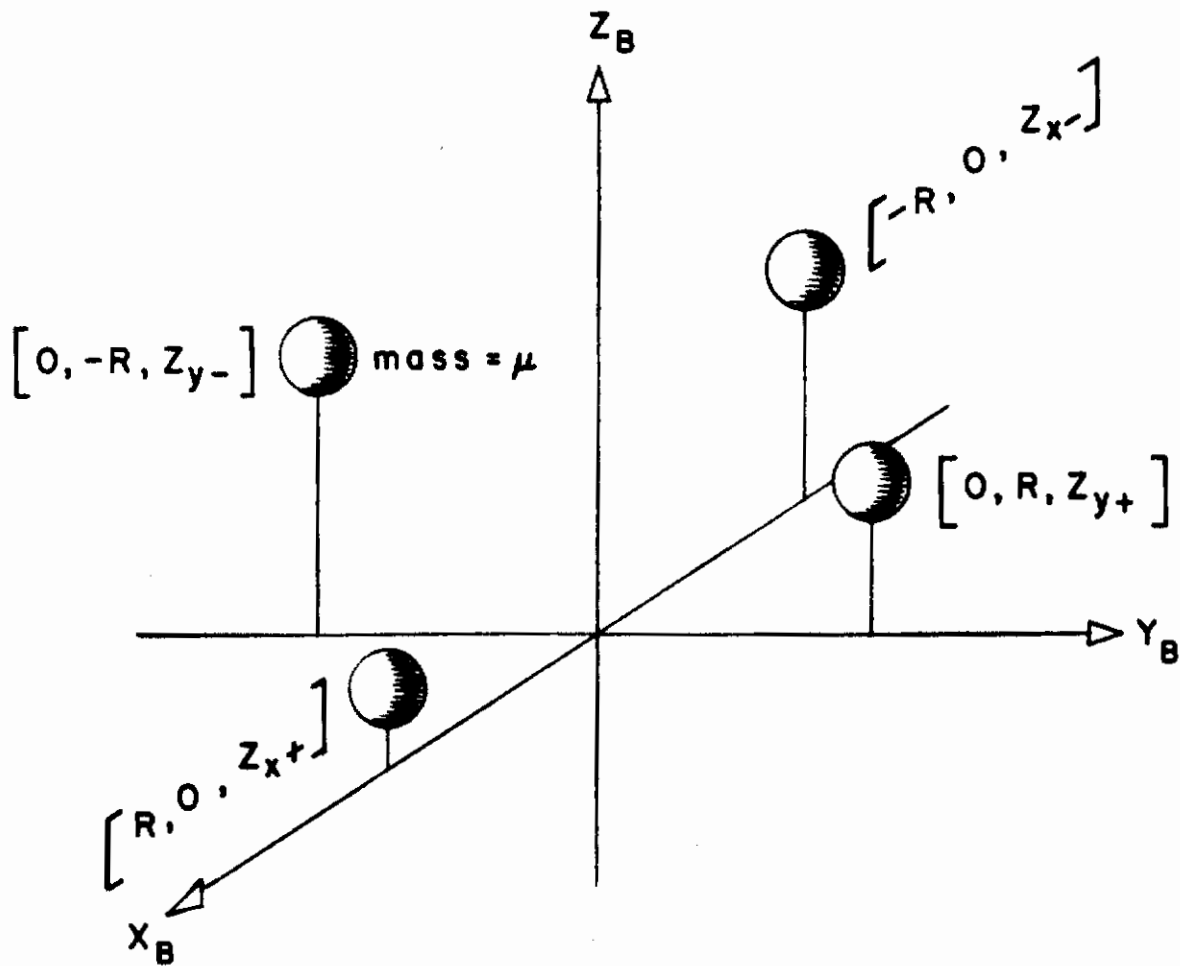


Fig. 2. GEOMETRY OF VERTICAL MOVING MASSES.

Contrails

- (5) All four masses are of equal value μ .
- (6) The vehicle spins nominally about the Z_B axis with constant rate β .
- (7) ω_x/β , ω_y/β , $\dot{\omega}_x/\beta$, $\dot{\omega}_y/\beta$ are first-order small.

Before applying these assumptions, \vec{H}_m is first expanded in body coordinates. Referring to Fig. 1,

$$\begin{bmatrix} H_{mx} \\ H_{my} \\ H_{mz} \end{bmatrix} = \begin{bmatrix} \sum_{i=1}^n m_i (r_{yi} v_{zi} - r_{zi} v_{yi}) \\ \sum_{i=1}^n m_i (r_{zi} v_{xi} - r_{xi} v_{zi}) \\ \sum_{i=1}^n m_i (r_{xi} v_{yi} - r_{yi} v_{xi}) \end{bmatrix}$$

Assumptions (1) to (6) lead to

$$\begin{bmatrix} H_{mx} \\ H_{my} \\ H_{mz} \end{bmatrix} = \begin{bmatrix} \mu R (\dot{z}_{y+} - \dot{z}_{y-}) \\ -\mu R (\dot{z}_{x+} - \dot{z}_{x-}) \\ 0 \end{bmatrix} \quad (2.9)$$

and the moment of inertia tensor \vec{I} has components,

$$I_{xx} = \mu (z_{x+}^2 + z_{x-}^2 + z_{y+}^2 + z_{y-}^2 + 2R^2) + I_t$$

Contrails

$$I_{xy} = I_{yx} = 0$$

$$I_{xz} = I_{zx} = -\mu R(Z_{x+} - Z_{x-})$$

$$I_{yy} = \mu \left(Z_{x+}^2 + Z_{x-}^2 + Z_{y+}^2 + Z_{y-}^2 + 2R^2 \right) + I_t$$

$$I_{yz} = I_{zy} = -\mu R(Z_{y+} - Z_{y-})$$

$$I_{zz} = 4\mu R^2 + I_s$$

If the requirement is imposed that the vehicle center of mass remains stationary during trim mass motion (because of the importance of minimizing gravity torques in the laboratory by keeping the mass center at the center of support), then

$$Z_{x-} = -Z_{x+} \triangleq -Z_x \quad \dot{Z}_{x-} = -\dot{Z}_{x+} \triangleq -\dot{Z}_x$$

$$Z_{y-} = -Z_{y+} \triangleq -Z_y \quad \dot{Z}_{y-} = -\dot{Z}_{y+} \triangleq -\dot{Z}_y$$

Equations (2.6) and (2.7) are now

$$\begin{bmatrix} M_{PIx} \\ M_{PIy} \\ M_{PIz} \end{bmatrix} = \begin{bmatrix} 2\mu R Z_y \beta^2 \\ -2\mu R Z_x \beta^2 \\ 0 \end{bmatrix} \quad (2.10a)$$

and

$$\begin{bmatrix} M_{MDx} \\ M_{MDy} \\ M_{MDz} \end{bmatrix} \doteq \begin{bmatrix} 4\mu(\dot{Z}_x Z_{xx} + \dot{Z}_y Z_{yy})\omega_x + 2\mu R\ddot{Z}_y \\ 4\mu(\dot{Z}_x Z_{xx} + \dot{Z}_y Z_{yy})\omega_y - 2\mu R\ddot{Z}_x \\ -4\mu R(\dot{Z}_x \omega_x + \dot{Z}_y \omega_y) \end{bmatrix} \quad (2.10b)$$

Although the nonlinear terms in the M_{MD} equations could have significance, the $4\mu(\dot{Z}_x Z_{xx} + \dot{Z}_y Z_{yy})$ term is three orders of magnitude below the $2\mu R\beta^2$ term in this mechanization and thus can be ignored. As a result, the M_{MD} equations reduce to

$$\begin{bmatrix} M_{MDx} \\ M_{MDy} \\ M_{MDz} \end{bmatrix} \doteq \begin{bmatrix} 2\mu R\ddot{Z}_y \\ -2\mu R\ddot{Z}_x \\ 0 \end{bmatrix}$$

and the linearized form of Eq. (2.8) is

$$\begin{bmatrix} \frac{M_{Bx}}{I_t} - \frac{2\mu R Z_y \beta^2}{I_t} - \frac{2\mu R \ddot{Z}_y}{I_t} \\ \frac{M_{By}}{I_t} + \frac{2\mu R Z_x \beta^2}{I_t} + \frac{2\mu R \ddot{Z}_x}{I_t} \end{bmatrix} \doteq \begin{bmatrix} \dot{\omega}_x - \frac{I_t - I_s}{I_t} \beta \omega_y \\ \dot{\omega}_y - \frac{I_s - I_t}{I_t} \beta \omega_x \end{bmatrix} \quad (2.11)$$

where $M_{Bx,y}$ represent disturbing moments and, in the case of a controlled body, the control torques as well.

Contrails

Equations (2.11) represent the terms in Eq. (2.5) created by products of inertia and mass motion as torques on a rigid body. Another equally valid representation is that the mass motion inside the body has the effect of reorienting the principal axis set with respect to the original ($t = 0$) coordinate system. Because it is not possible to align the null axis of the attitude sensor with the maximum axis of inertia as precisely as is necessary (less than 10^{-4} rad) for this control problem, it is of great practical importance to be able to move the principal axes relative to the body.

To size a trim-system design correctly, knowledge of the range through which the principal axis set may be moved is useful. This angle, measured from the $t = 0$ principal axis set, can be calculated by re-diagonalizing \vec{I} ,

$$\vec{I}(t > 0) = \begin{bmatrix} I_{xx} & 0 & I_{xz} \\ 0 & I_{yy} & I_{yz} \\ I_{zx} & I_{zy} & I_{zz} \end{bmatrix}$$

This is equivalent to solving for the orientation of the eigenvector \vec{a} in the equation

$$\vec{I} \cdot \vec{a} = \lambda \vec{E} \cdot \vec{a} \quad (2.12)$$

Expanding (2.12),

$$\begin{aligned} (I_{xx} - \lambda)a_x + I_{xz}a_z &= 0 \\ (I_{yy} - \lambda)a_y + I_{yz}a_z &= 0 \\ (I_{zz} - \lambda)a_z + I_{zx}a_x + I_{zy}a_y &= 0 \end{aligned} \quad (2.13)$$

Contrails

and referring to Fig. 3,

$$\tan \phi = \frac{\rho}{a_z} \quad \tan \theta = \frac{a_y}{a_x} \quad \rho = \left(a_x^2 + a_y^2 \right)^{1/2}$$

Noting that

$$I_{xx} = I_{yy}$$

$$I_{zx} = I_{xz}$$

$$I_{yz} = I_{zy}$$

Eqs. (2.13) lead to

$$\tan \phi = \frac{2 \left(I_{xz}^2 + I_{yz}^2 \right)^{1/2}}{\left(I_{zz} - I_{xx} \right) + \left[\left(I_{zz} - I_{xx} \right)^2 + 4 \left(I_{xz}^2 + I_{yz}^2 \right) \right]^{1/2}} \quad (2.14)$$

$$\tan \theta = \frac{I_{yz}}{I_{xz}}$$

Substituting values for the components of $\vec{\Gamma}$ calculated previously into Eqs. (2.14),

$$\tan \phi \doteq \frac{4R\mu \left(Z_x^2 + Z_y^2 \right)^{1/2}}{I_t} \left\{ \left[m^2 + \frac{16R^2\mu^2}{I_t^2} \left(Z_x^2 + Z_y^2 \right) \right]^{1/2} + m \right\}^{-1} \quad (2.15)$$

$$\tan \theta \doteq \frac{Z_y}{Z_x} \quad m \triangleq \frac{I_s - I_t}{I_t}$$

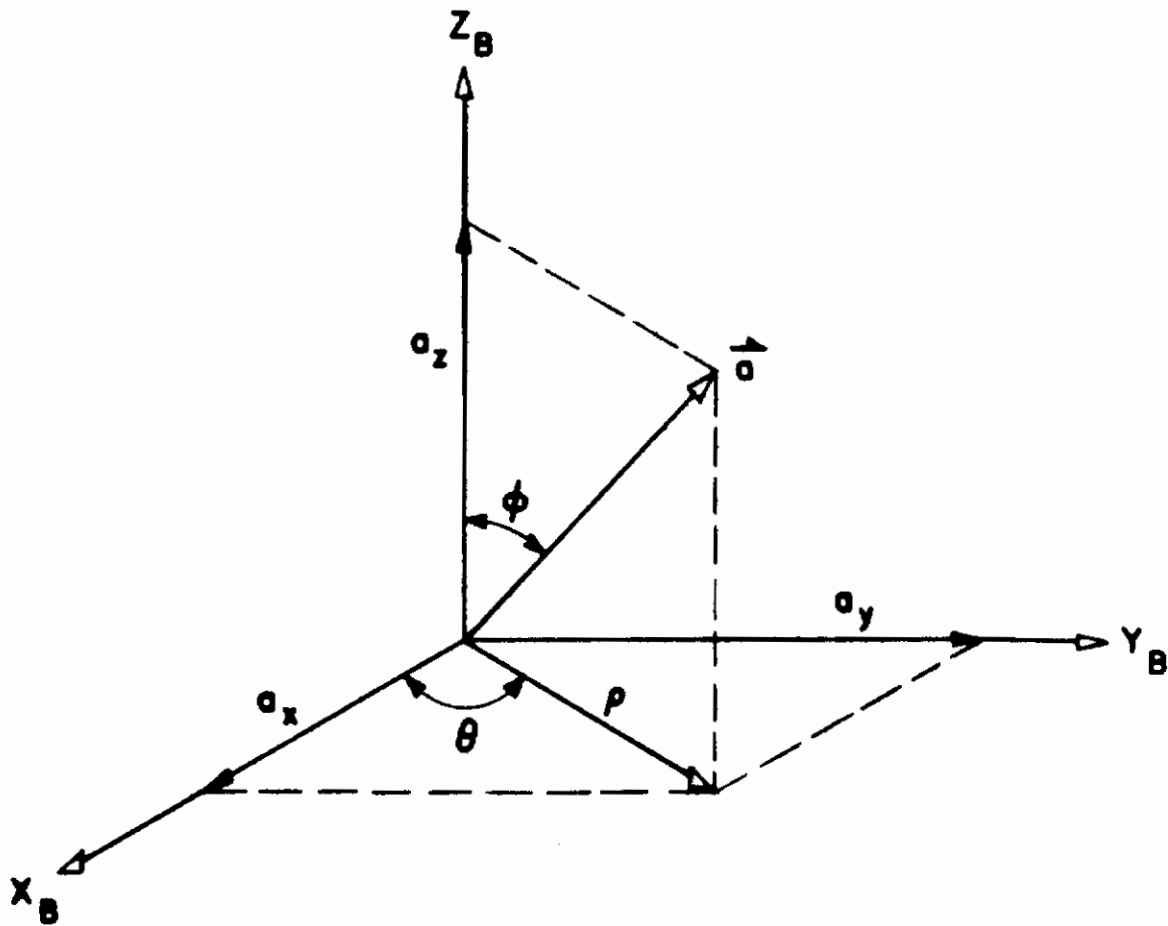


Fig. 3. COMPONENTS OF \vec{a} IN BODY COORDINATES.

The maximum ϕ through which the SVS trim system can move the principal axes is 0.04 rad (2.3°).

B. Equations of Motion of a Rotating Two-Degree-of-Freedom Gyroscope

The gyroscope in the SVS control system is used as an attitude reference (controller modes 1 and 2) and as a control actuator (controller modes 4 and 5). It is important to understand the characteristics of the gyro as related to these applications. Gimbal friction can cause a drift unacceptably large for use as an attitude reference. Interaction between the vehicle and the nutation of the gyro could cause disturbing moments large enough to affect control precision. This section models the gyro, including gimbal inertias, bearing friction, and null offset, and investigates their effects on attitude errors.

Figure 4 illustrates the gyro gimbal angles δ'_x and δ'_y in relation to a body coordinate set. The null offsets b_x and b_y are caused by a misalignment between the gyro null axis and the Z_B axis and are related to δ_x and δ_y by

$$\begin{aligned}\delta'_x &= \delta_x + b_x & \delta'_y &= \delta_y + b_y \\ \dot{\delta}'_x &= \dot{\delta}_x & \dot{\delta}'_y &= \dot{\delta}_y\end{aligned}$$

For the inner gimbal,

$$\overset{I}{\vec{H}}_{IG} = \overset{IG}{\vec{H}}_{IG} + \vec{\omega}^{IG-I} \times \overset{IG}{\vec{H}}_{IG} \quad (2.16)$$

where

$$\vec{\omega}^{IG-I} = \vec{\omega}^{IG-OG} + \vec{\omega}^{OG-B} + \vec{\omega}^{B-I} \quad (2.17)$$

$$\overset{I}{\vec{H}}_{IG} = \overset{IG}{\vec{I}}_{IG} \cdot \vec{\omega}^{IG-I} + \overset{IG}{\vec{H}}$$

Contrails

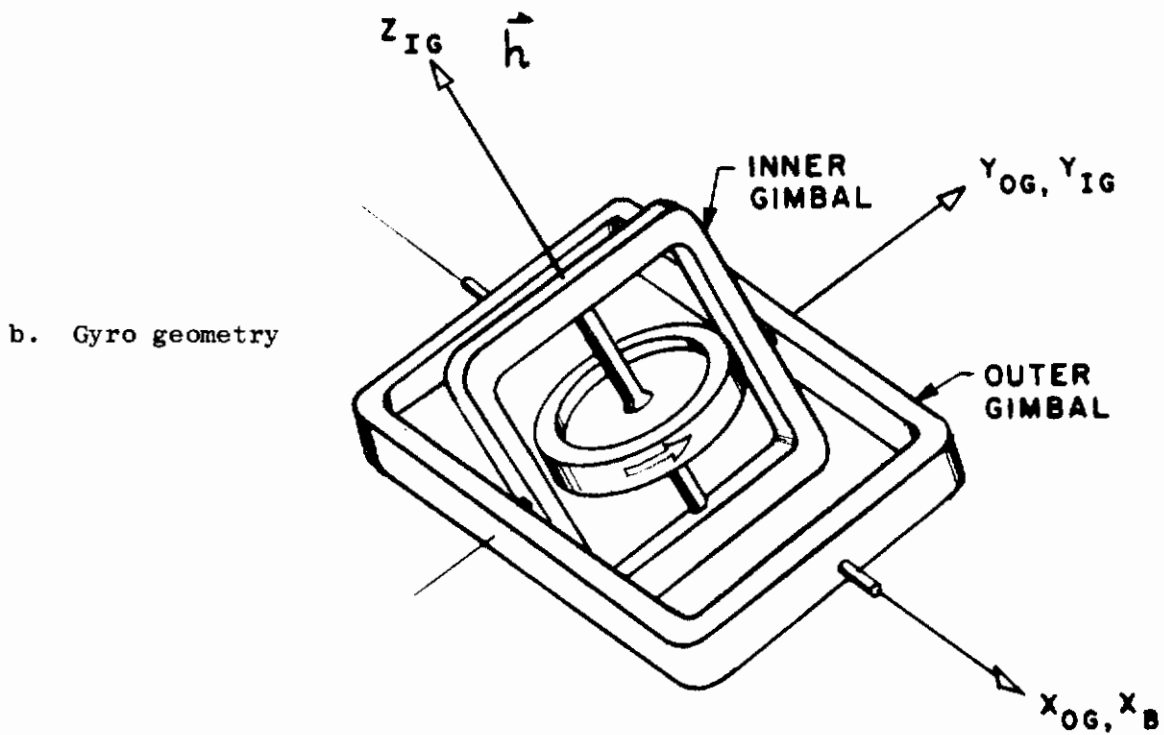
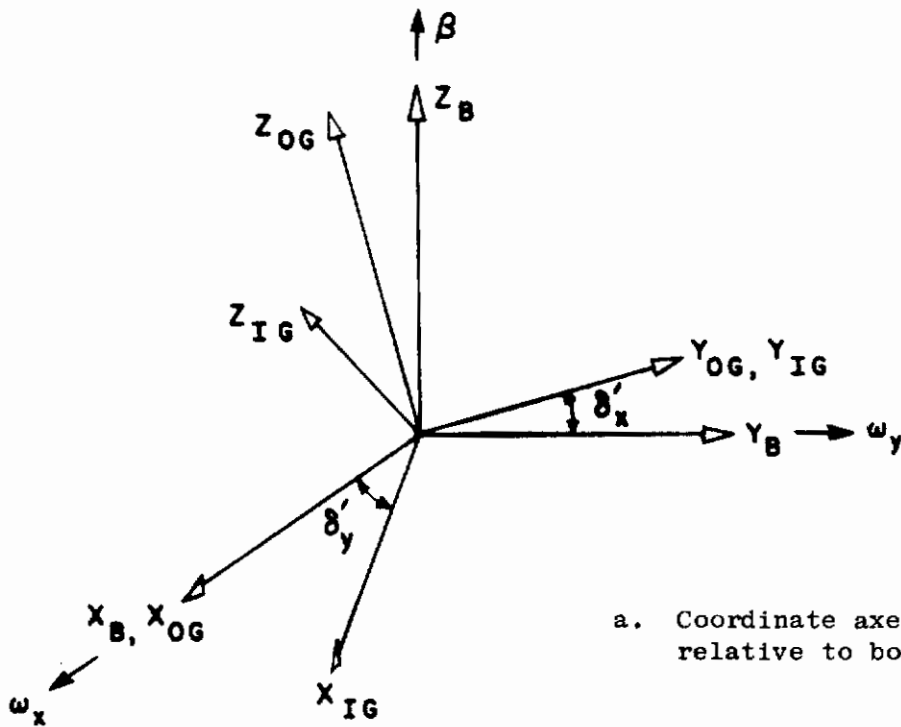


Fig. 4. TWO-DEGREE-OF-FREEDOM GYROSCOPE.

Expanding Eqs. (2.17) coordinatized in the inner-gimbal reference frame, $\vec{\omega}_{IG-I}$ has the components

$$\begin{bmatrix} \omega_{IGx} \\ \omega_{IGy} \\ \omega_{IGz} \end{bmatrix} = \begin{bmatrix} 0 \\ \dot{\delta}_y \\ 0 \end{bmatrix} + \begin{bmatrix} \dot{\delta}_x \cos \delta_y \\ 0 \\ -\dot{\delta}_x \sin \delta_y \end{bmatrix} \quad (2.18)$$

$$+ \begin{bmatrix} \omega_x \cos \delta'_y + \omega_y \sin \delta'_x \sin \delta'_y - \beta \cos \delta'_x \sin \delta'_y \\ \omega_y \cos \delta'_x + \beta \sin \delta'_x \\ \omega_x \sin \delta'_y - \omega_y \sin \delta'_x \cos \delta'_y + \beta \cos \delta'_x \cos \delta'_y \end{bmatrix}$$

and the components of \vec{H}_{IG} are

$$\begin{bmatrix} H_{IGx} \\ H_{IGy} \\ H_{IGz} \end{bmatrix} = \begin{bmatrix} (I_{IGx} + I_{wt})\omega_{IGx} \\ (I_{IGy} + I_{wt})\omega_{IGy} \\ (I_{IGz} + I_{ws})\omega_{IGz} \end{bmatrix} + \begin{bmatrix} 0 \\ 0 \\ h \end{bmatrix} \quad (2.19)$$

where I_{wt} and I_{ws} are the wheel transverse and spin-axis moments of inertia, respectively.

Equation (2.16) now can be expanded in the inner-gimbal coordinate system:

$$\begin{bmatrix} M_{IGx} \\ M_{IGy} \\ M_{IGz} \end{bmatrix} = \begin{bmatrix} (I_{IGx} + I_{wt})\dot{\omega}_{IGx} + (I_{ws} + I_{IGz} - I_{wt} - I_{IGy})\omega_{IGy}\omega_{IGz} + h\omega_{IGy} \\ (I_{IGy} + I_{wt})\dot{\omega}_{IGy} + (I_{wt} + I_{IGx} - I_{ws} - I_{IGz})\omega_{IGx}\omega_{IGz} - h\omega_{IGx} \\ (I_{IGz} + I_{ws})\dot{\omega}_{IGz} + (I_{IGy} - I_{IGx})\omega_{IGy}\omega_{IGx} \end{bmatrix} \quad (2.20)$$

The equations for the outer gimbal corresponding to (2.16) and (2.17) are

$$\vec{H}_{OG}^I = \vec{H}_{OG}^{OG} + \vec{\omega}^{OG-I} \times \vec{H}_{OG}$$

where

$$\vec{\omega}^{OG-I} = \vec{\omega}^{OG-B} + \vec{\omega}^{B-I} \quad (2.21)$$

$$\vec{H}_{OG} = \vec{I}_{OG} \cdot \vec{\omega}^{OG-I}$$

Coordinatized in the outer-gimbal reference axes, Eqs. (2.21) can be expanded to give

$$\begin{bmatrix} \omega_{OGx} \\ \omega_{OGy} \\ \omega_{OGz} \end{bmatrix} = \begin{bmatrix} \dot{\delta}_x \\ 0 \\ 0 \end{bmatrix} + \begin{bmatrix} \omega_x \\ \omega_y \cos \delta'_x + \beta \sin \delta'_x \\ \beta \cos \delta'_x - \omega_y \sin \delta'_x \end{bmatrix} \quad (2.22a)$$

and

$$\begin{bmatrix} M_{OGx} \\ M_{OGy} \\ M_{OGz} \end{bmatrix} = \begin{bmatrix} I_{OGx} \dot{\omega}_{OGx} + (I_{OGz} - I_{OGy}) \omega_{OGy} \omega_{OGz} \\ I_{OGy} \dot{\omega}_{OGy} + (I_{OGx} - I_{OGz}) \omega_{OGx} \omega_{OGz} \\ I_{OGz} \dot{\omega}_{OGz} + (I_{OGy} - I_{OGx}) \omega_{OGx} \omega_{OGy} \end{bmatrix} \quad (2.22b)$$

Because the two gimbal bearings are along the $Y_{OG} - Y_{IG}$ and $X_{OG} - X_B$ axes, δ_x and δ_y can be solved for most easily by examining the equations for M_{OGx} and M_{IGy} . Define M_{Cx} and M_{Cy} as the control torques applied to the vehicle by the gyro torquers and f as the coefficient of viscous bearing friction.[†] From (2.20) and (2.22) for the CMG application,

$$M_{OGx} = -M_{Cx} - f \dot{\delta}_x - M_{IGy} \cos \delta_y - M_{IGz} \sin \delta_y \quad (2.23)$$

$$M_{IGy} = -M_{Cy} - f \dot{\delta}_y - M_{OGy}$$

In the attitude-sensor case, \vec{M}_C would be zero.

To simplify the expanded forms of Eqs. (2.23), assumptions can be made regarding the importance of various terms. When using a gyro as a vertical reference, the primary concern is drift caused by bearing friction; the effects of finite gimbal inertias are secondary. When the gyro is used as a CMG, interaction between the nutating gyro and the motion of the controlled vehicle is significant; consequently, simplifying assumptions specific to each application will be made.

1. The Gyro as an Attitude Reference

When the gyro is used as an attitude reference,

$$(1) \quad \sin \delta' \doteq \delta' \quad \cos \delta' \doteq 1$$

[†] Experimental data have shown that the gyro is adequately described without modeling bearing stiction.

$$(2) \quad \frac{|\omega_{x,y}|}{|\delta_{x,y}|} \doteq 1$$

$$(3) \quad \frac{I_{OG}}{h}, \quad \frac{I_{IG}}{h}, \quad \frac{I_{wt,s}}{h} \quad \text{are first-order small}$$

Thus,

$$\begin{bmatrix} \omega_{OGx} \\ \omega_{OGy} \\ \omega_{OGz} \end{bmatrix} \doteq \begin{bmatrix} \dot{\delta}_x + \omega \\ \omega_y + \beta \dot{\delta}_x' \\ \beta \end{bmatrix} \quad \begin{bmatrix} \omega_{IGx} \\ \omega_{IGy} \\ \omega_{IGz} \end{bmatrix} \doteq \begin{bmatrix} \dot{\delta}_x + \omega_x - \beta \dot{\delta}_y' \\ \dot{\delta}_y + \omega_y + \beta \dot{\delta}_x' \\ \beta \end{bmatrix}$$

and Eqs. (2.23) become

$$\begin{aligned} (I_{IGy} + I_{wt}) (\ddot{\delta}_y + \dot{\omega}_y + \beta \dot{\delta}_x) + f \dot{\delta}_y + (I_{wt} + I_{IGx} - I_{ws} - I_{IGz}) (\beta \dot{\delta}_x + \beta \omega_x - \beta^2 \dot{\delta}_y) \\ - h (\dot{\delta}_x + \omega_x - \beta \dot{\delta}_y) = \left[(I_{wt} + I_{IGx} - I_{ws} - I_{IGz}) \beta - h \right] \beta b_y \end{aligned} \quad (2.24a)$$

and

$$\begin{aligned} (I_{OGx} + I_{wt} + I_{IGx}) (\ddot{\delta}_x + \dot{\omega}_x) + f \dot{\delta}_x + (I_{OGz} + I_{ws} + I_{IGz} - I_{OGy} - I_{wt} - I_{IGy}) \\ (\omega_y \beta + \beta^2 \dot{\delta}_x) + (I_{ws} + I_{IGz} - 2I_{wt} - I_{Gx} - I_{Gy}) \beta \dot{\delta}_y \\ + h (\dot{\delta}_y + \omega_y + \beta \dot{\delta}_x) = - \left[(I_{OGz} - I_{OGy} + I_{ws} + I_{IGz} - I_{wt} - I_{IGy}) \beta + h \right] \beta b_x \end{aligned} \quad (2.24b)$$

The damping torque has been included on the left-hand side while the offset bias of the synchro with respect to the body axes is written as a forcing function. The implication is that the biases act

Conrails

as driving torques, exciting the equations even in the case when the vehicle is spinning solely about its Z_B - axis.

The combined effect of bias and bearing friction can be obtained in closed form if it is further assumed that the body is spinning about its Z_B - axis; this is equivalent to assuming that $\beta \gg \omega_{x,y}$, a reasonable assumption for the simulator initial conditions. To first order, Eqs. (2.24) reduce to

$$\frac{-f}{h} \dot{\delta}_y + \dot{\delta}_x - \beta \delta_y = \beta b_y \quad (2.25)$$

$$\frac{-f}{h} \dot{\delta}_x - \dot{\delta}_y - \beta \delta_x = \beta b_x$$

After taking the Laplace transform with zero initial conditions for the δ ,

$$\delta_x(s) = \frac{-\beta}{s} \frac{\{(f/h)s + \beta\}b_x - b_y s}{\{(f/h)s + \beta\}^2 + s^2}$$
$$\delta_y(s) = \frac{-\beta}{s} \frac{\{(f/h)s + \beta\}b_y + b_x s}{\{(f/h)s + \beta\}^2 + s^2} \quad \frac{f}{h} \triangleq A$$

which transform to the time domain as

$$\delta_x(t) = b_y \exp\left(-\frac{A\beta t}{A^2 + 1}\right) \sin \frac{\beta t}{A^2 + 1} - b_x \left[1 - \exp\left(-\frac{A\beta t}{A^2 + 1}\right) \cos \frac{\beta t}{A^2 + 1}\right] \quad (2.26)$$

$$\delta_y(t) = -b_x \exp\left(-\frac{A\beta t}{A^2 + 1}\right) \sin \frac{\beta t}{A^2 + 1} - b_y \left[1 - \exp\left(-\frac{A\beta t}{A^2 + 1}\right) \cos \frac{\beta t}{A^2 + 1}\right]$$

The result of the bearing friction is to force the gimbals to align themselves with the body Z - axis because

$$\delta_x(t \rightarrow \infty) = -b_x \quad (2.27)$$

$$\delta_y(t \rightarrow \infty) = -b_y$$

If there were negligible bearing friction ($A \rightarrow 0$), then

$$\delta_x(t) = b_y \sin \beta t - b_x(1 - \cos \beta t)$$

$$\delta_y(t) = -b_x \sin \beta t - b_y(1 - \cos \beta t)$$

which is the expected coning motion.

Equations (2.27) indicate that bearing friction causes the gyro \vec{h} to align itself with the vehicle spin vector; as a result, use of the gyro as an attitude reference is dependent on the time required for the autocollimator to acquire the reference mirror, the value of the time constant $A\beta/(A^2+1)$, and $b_{x,y}$. If $b_{x,y} > 0.01$ rad and $A > 0.01 \text{ cm}^{-1}$, the gyro will drift enough in the approximately 150 sec required to initially stabilize the vehicle so that the angle between the mirror and autocollimator will be excessive. Experimental evidence has shown, however, that performance is marginal only when initial conditions are larger than 0.1 rad.

2. The Gyro as a CMG

When the gyro is used as a CMG, the gimbal inertias are of greater significance and the following assumptions are made:

- (1) $\sin \delta' \doteq \delta' \quad \cos \delta' \doteq 1$
- (2) $\omega_{x,y} \doteq 0$
- (3) $\beta = 1$

Linearizing Eqs. (2.24) and substituting numerical values for the gimbal inertias and $|\vec{h}|$,

Contrails

$$8.17 \times 10^{-4} \ddot{\delta}_y + A\dot{\delta}_y + \delta_y - \dot{\delta}_x = -b_y - \frac{M_{Cy}}{h} \quad (2.28)$$

$$1.14 \times 10^{-3} \ddot{\delta}_x + A\dot{\delta}_y + \delta_x + \dot{\delta}_y = -b_x - \frac{M_{Cx}}{h}$$

The characteristic equation for (2.28) yields the following values for the natural frequencies and damping coefficients:

$$\omega_{n1} = 28.8 \text{ rad/sec} \quad \omega_{n2} = 35.8 \text{ rad/sec}$$

$$\zeta_1 = 0.0159 \quad \zeta_2 = 0.0167 \quad A = 0.001$$

where $\omega_{n1,2}$ are the nutation frequencies and $\zeta_{1,2}$ the damping coefficients.

The conclusion drawn is that the nutation frequencies are so much greater than the spin frequency ($\beta = 1 \text{ rad/sec}$) or the polhode frequency ($\omega_p = m\beta = 0.804 \text{ rad/sec}$) that the gyro-vehicle interaction is negligible. Even if the frequencies were closer, the gimbal inertias are four orders of magnitude below the vehicle moments of inertia, making the gyro effect on the vehicle undetectable, other than as a body against which to torque.

For purposes of analog simulation, the dynamical model of the gyro thus can be simplified to

$$\beta\delta_y - \dot{\delta}_x = -\beta b_y - \frac{M_{Cy}}{h} \quad (2.29)$$

$$\beta\delta_x + \dot{\delta}_y = -\beta b_x - \frac{M_{Cx}}{h}$$

which reduce to the "Law of the Gyro" as $\beta \rightarrow 0$.

C. Output Equations of a Rotating Two-Axis Autocollimator

Precision-attitude error is measured optically by an autocollimator whose optical axis is parallel to the vehicle symmetry axis. The autocollimator reflects light off a mirror mounted in the laboratory and has an electrical output proportional to the angle of the return beam measured with respect to the perpendicular to the mirror surface. This angle is divided into two orthogonal components. The linear range of the autocollimator extends from 0.5 to 1000 arc seconds; a useful output is available out to 4000 arc seconds.

Figure 5 indicates the angles measured by the autocollimator γ'_x and γ'_y . The misalignments between the maximum axis of inertia and the autocollimator optical axis are α_x and α_y and are related to $\gamma'_{x,y}$ by

$$\gamma'_x = \gamma_x + \alpha_x \quad \dot{\gamma}'_x = \dot{\gamma}_x$$

$$\gamma'_y = \gamma_y + \alpha_y \quad \dot{\gamma}'_y = \dot{\gamma}_y$$

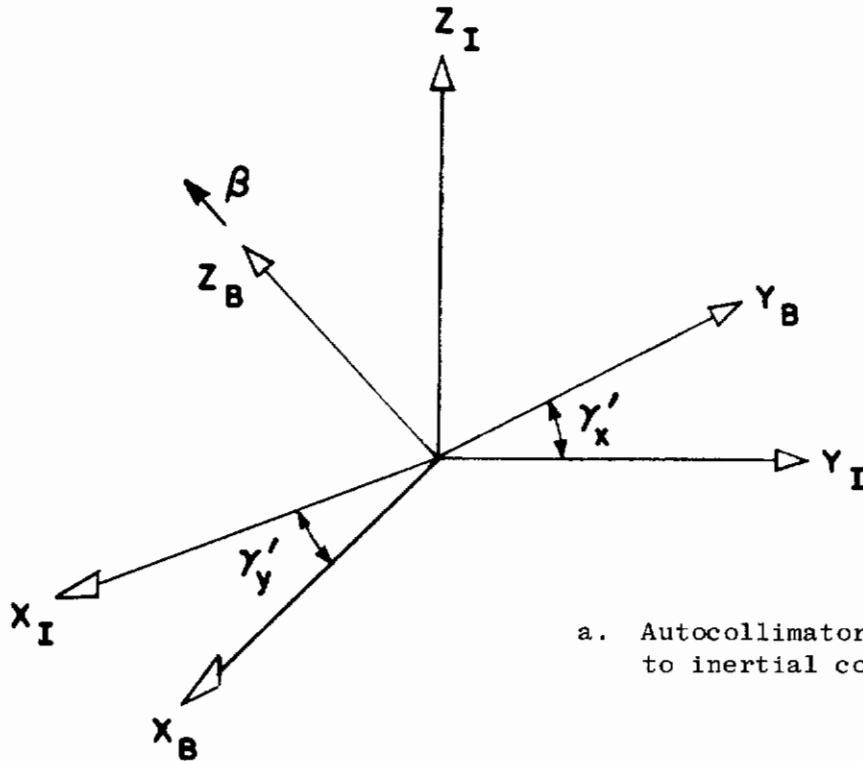
For $\gamma_{x,y}$ in the autocollimator linear region, $\dot{\gamma}'_{x,y}$ can be approximated as

$$\dot{\gamma}'_x = \omega_x + \beta\dot{\gamma}'_y \tag{2.30}$$

$$\dot{\gamma}'_y = \omega_y - \beta\dot{\gamma}'_x$$

Solving Eqs. (2.30) for $\omega_{x,y}$ and substituting into Eqs. (2.11),

$$\begin{bmatrix} \frac{M_{Bx}}{I_t} - \frac{2\mu R\beta^2 Z_y}{I_t} - \frac{2\mu R\ddot{Z}_y}{I_t} \\ \frac{M_{By}}{I_t} + \frac{2\mu R\beta^2 Z_x}{I_t} + \frac{2\mu R\ddot{Z}_x}{I_t} \end{bmatrix} = \begin{bmatrix} \ddot{\gamma}'_x - \beta\dot{\gamma}'_y - \frac{(I_t - I_s)}{I_t} \beta(\dot{\gamma}'_y + \beta\dot{\gamma}'_x) \\ \ddot{\gamma}'_y + \beta\dot{\gamma}'_x + \frac{(I_t - I_s)}{I_t} \beta(\dot{\gamma}'_x - \beta\dot{\gamma}'_y) \end{bmatrix} \tag{2.31}$$



a. Autocollimator angles, relative to inertial coordinate system

b. Autocollimator geometry

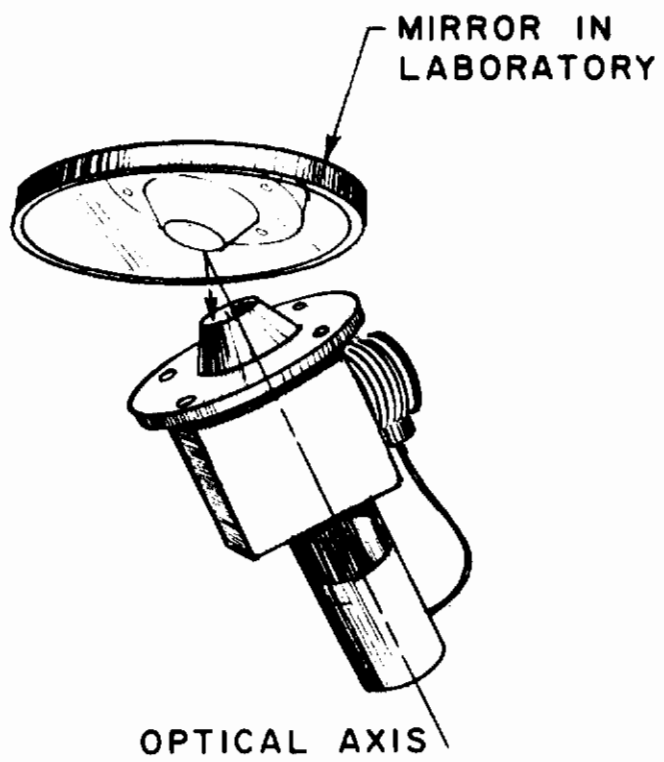


Fig. 5. TWO-AXIS AUTOCOLLIMATOR.

Contraails

Define $n \triangleq I_s/I_t$, $m \triangleq (I_s - I_t)/I_t$, and moments applied to the body, divided by I_t , as Q . Equation (2.31) then reduces to

$$\begin{aligned} \ddot{\gamma}_x + m\beta^2 \gamma_x - (2 - n)\beta \dot{\gamma}_y &= Q_x \\ \ddot{\gamma}_y + m\beta^2 \gamma_y + (2 - n)\beta \dot{\gamma}_x &= Q_y \end{aligned} \tag{2.32}$$

which are the output equations of a rotating autocollimator.

Closed-form solutions for $\gamma_{x,y}$ can be obtained by taking the Laplace transform of (2.32). For zero initial conditions on γ ,

$$\begin{aligned} \gamma_x(s) &= \frac{\left[Q_x(s) - (m\beta^2 \alpha_x/s) \right] (s^2 + m\beta^2) + \left[Q_y(s) - (m\beta^2 \alpha_y/s) \right] (2 - n) \beta s}{(s^2 + m\beta^2) + (2 - n)^2 \beta^2 s^2} \\ \gamma_y(s) &= \frac{\left[Q_y(s) - (m\beta^2 \alpha_y/s) \right] (s^2 + m\beta^2) + \left[Q_x(s) - (m\beta^2 \alpha_x/s) \right] (2 - n) \beta s}{(s^2 + m\beta^2) + (2 - n)^2 \beta^2 s^2} \end{aligned}$$

The effect of a misalignment of the axis of maximum inertia and the autocollimator null axis is

$$\begin{aligned} \gamma_x(t) &= \frac{\alpha_x}{n} \left(m \cos \beta t - \cos m\beta t - \frac{1}{n} \right) + \frac{\alpha_y}{n} \left(m \sin \beta t - \sin m\beta t \right) \\ \gamma_y(t) &= \frac{\alpha_y}{n} \left(m \cos \beta t - \cos m\beta t - \frac{1}{n} \right) - \frac{\alpha_x}{n} \left(m \sin \beta t - \sin m\beta t \right) \end{aligned} \tag{2.33}$$

Because there is no damping term as in the gyro equations, γ describes Lissajous figures indefinitely, with an offset of $-(\alpha_{x,y}/n^2)$. If a body-fixed moment is present, the solution would have an identical form, the offset being

Contrails

$$\frac{Q_{DBx,y} - m\beta\alpha_{x,y}}{mn^2\beta}$$

If the Q is fixed in inertial space,

$$Q_{DIX}(t) = Q_{DIX} \sin \beta t \quad Q_{DIY}(t) = Q_{DIY} \cos \beta t$$

the autocollimator output (no misalignment bias) would be

$$\begin{aligned} \gamma_x(t) = & \frac{Q_{DIX}}{n^2\beta^2(2-n)} \left[m(\cos \beta t - \cos m\beta t) + \frac{\beta n(2-n)t}{2} \sin \beta t \right] \\ & - \frac{Q_{DIY}}{n\beta^2(2-n)^2} \left[(\cos \beta t - \cos m\beta t) + \frac{\beta m(2-n)t}{2} \sin \beta t \right] \end{aligned} \quad (2.34)$$

$$\begin{aligned} \gamma_y(t) = & \frac{Q_{DIY}}{n^2\beta^2(2-n)} \left[m(\cos \beta t - \cos m\beta t) + \frac{\beta m(2-n)t}{2} \sin \beta t \right] \\ & + \frac{Q_{DIX}}{n\beta^2(2-n)^2} \left[(\cos \beta t - \cos m\beta t) + \frac{\beta n(2-n)t}{2} \sin \beta t \right] \end{aligned}$$

The major distinction between Eqs. (2.33) and (2.34) is the secular terms

$$\frac{Q_{DIX,y} t \sin \beta t}{2n\beta} \quad \text{and} \quad \frac{Q_{DIX,y} mt \sin \beta t}{2n\beta(2-n)}$$

in (2.34), which indicate that the attitude error grows with time in the presence of inertial moments. If the CMG supplies the control torque to the body, the gimbal angles will increase with time rather than the attitude error as the gyro absorbs angular momentum from the vehicle. At some point, the gyro will no longer be able to absorb the angular momentum and the gyro unload (CMG momentum dumping) process must occur.

Contrails

Chapter III

DESIGN OF A PRECISION ATTITUDE CONTROLLER FOR A SYMMETRIC SPINNING BODY

In Section A, the linear control law derived by Lange, Fleming, and Parkinson [7] is shown to be similar to a control law used for a gyro-wheel stabilized nonspinning vehicle (gyrostat); gain selections are made based on the results presented in Ref. 7. A control law for an automatic mass trim system is discussed in Section B, and attitude controller stability as a function of trim-system gains is analyzed. Stability of a controller with saturation nonlinearities studied by analog simulation is presented in Section C.

A. Similarities between a Gyrostat Controller and a Spinning-Vehicle Control Law Derived from Frequency Symmetry

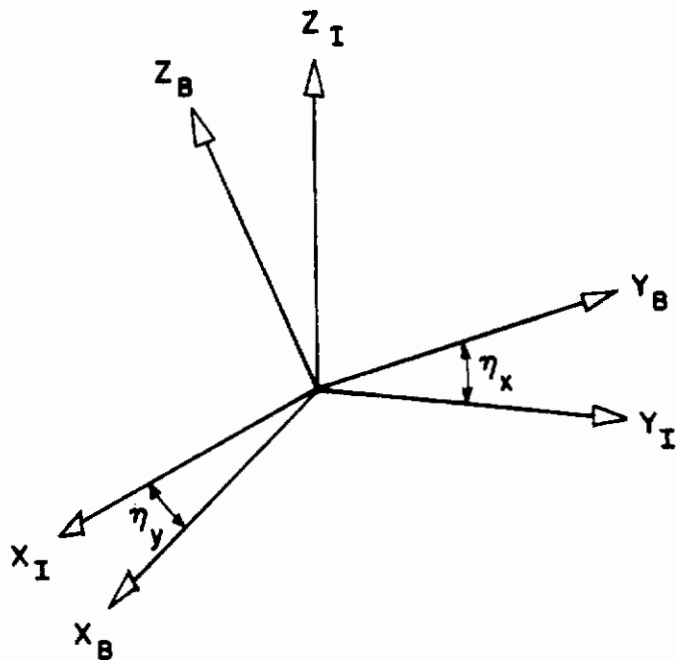
The control of a spinning symmetric body can be related to the problem of attitude control of a gyrostat. In each case, three gains must be chosen: the usual rate and position feedback typical of $1/S^2$ plant control plus a cross-coupling gain similar to the control law used to erect a gyro.

With reference to Fig. 6,

$$\vec{H} = \vec{I} \cdot \vec{\omega}^{B-I} + \vec{H}$$

In body coordinates,

$$\vec{I} \cdot \vec{\omega}^{B-I} = \begin{bmatrix} I_t \dot{\eta}_x \\ I_t \dot{\eta}_y \\ I_s \dot{\eta}_z \end{bmatrix}$$



a. Attitude error angles (small-angle approximation)

b. Gyrostat geometry

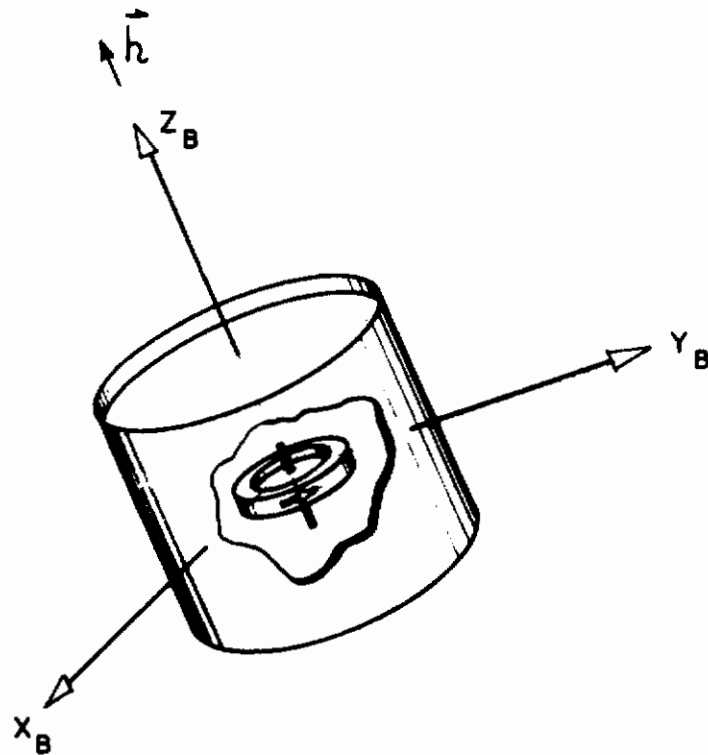


Fig. 6. SYMMETRIC GYROSTAT.

Controls

and

$$\begin{bmatrix} M_{Bx} \\ M_{By} \end{bmatrix} = \begin{bmatrix} I_t \ddot{\eta}_x + (I_s - I_t) \dot{\eta}_y \dot{\eta}_z - \dot{\eta}_y h \\ I_t \ddot{\eta}_y + (I_t - I_s) \dot{\eta}_x \dot{\eta}_z + \dot{\eta}_x h \end{bmatrix} \quad (3.1)$$

Postulating a control of the form

$$\begin{bmatrix} \frac{M_{Cx}}{I_t} \\ \frac{M_{Cy}}{I_t} \end{bmatrix} = \begin{bmatrix} -K_\delta & -K_\rho & +K_{xc} & 0 \\ -K_{xc} & 0 & -K_\delta & -K_\rho \end{bmatrix} \begin{bmatrix} \eta_x \\ \dot{\eta}_x \\ \eta_y \\ \dot{\eta}_y \end{bmatrix} \quad (3.2)$$

and assuming small body rates, Eq. (3.1) can be written as

$$\begin{bmatrix} Q_{Dx} \\ Q_{Dy} \end{bmatrix} = \begin{bmatrix} \ddot{\eta}_x + K_\rho \dot{\eta}_x + K_\delta \eta_x - \left(\frac{h}{I_t} \dot{\eta}_y + K_{xc} \eta_y \right) \\ \ddot{\eta}_y + K_\rho \dot{\eta}_y + K_\delta \eta_y + \left(\frac{h}{I_t} \dot{\eta}_x + K_{xc} \eta_x \right) \end{bmatrix} \quad (3.3)$$

The characteristic equation for (3.3) is

$$\left(s^2 + K_\rho s + K_\delta \right)^2 + \left(\frac{h}{I_t} s + K_{xc} \right)^2 = 0$$

Root loci can be plotted by varying the parameter $(h/I_t)^2$. The controlled system is least sensitive to changes in this parameter or to small gain changes when K_ρ , K_δ , and K_{xc} are chosen so that the

Contraails

locus is a vertical straight line. The two pairs of operating roots lie along this line and can move only vertically with changes in $(h/I_t)^2$; as a result, system time constants are insensitive to $(h/I_t)^2$.

A symmetric body spinning about its Z_B -axis with constant rate β has linearized attitude equations [from (2.32)],

$$\begin{bmatrix} Q_x \\ Q_y \end{bmatrix} = \begin{bmatrix} \ddot{\gamma}_x + m\beta^2 \gamma_x - (2-n) \beta \dot{\gamma}_y \\ \ddot{\gamma}_y + m\beta^2 \gamma_y + (2-n) \beta \dot{\gamma}_x \end{bmatrix} \quad (3.4)$$

To make use of the nonspinning control law of Eqs. (3.2), γ_x and γ_y must be coordinatized in a nonspinning coordinate frame:

$$\begin{bmatrix} \xi_x \\ \dot{\xi}_x \\ \xi_y \\ \dot{\xi}_y \end{bmatrix} = \begin{bmatrix} \gamma_x \cos \beta t - \gamma_y \sin \beta t \\ (\dot{\gamma}_x + \beta \gamma_y) \cos \beta t - (\dot{\gamma}_y - \beta \gamma_x) \sin \beta t \\ \gamma_y \cos \beta t + \gamma_x \sin \beta t \\ (\dot{\gamma}_y - \beta \gamma_x) \cos \beta t + (\dot{\gamma}_x + \beta \gamma_y) \sin \beta t \end{bmatrix} \quad (3.5)$$

Multiplying by the control gains K_ρ , K_δ , and K_{xc} and recoordinating in the spinning reference axes, the control law becomes

$$\begin{bmatrix} Q_{Cx} \\ Q_{Cy} \end{bmatrix} = \begin{bmatrix} \cos \beta t & \sin \beta t \\ -\sin \beta t & \cos \beta t \end{bmatrix} \begin{bmatrix} -K_\delta & -K_\rho & 0 & +K_{xc} \\ -K_{xc} & 0 & -K_\delta & -K_\rho \end{bmatrix} \begin{bmatrix} \xi_x \\ \dot{\xi}_x \\ \xi_y \\ \dot{\xi}_y \end{bmatrix} \quad (3.6)$$

so that

$$\begin{bmatrix} Q_{Cx} \\ Q_{Cy} \end{bmatrix} = \begin{bmatrix} -K_{\delta}\dot{\gamma}_x - K_{\rho}\dot{\gamma}_x + (K_{xc} - K_{\rho}\beta)\dot{\gamma}_y \\ -K_{\delta}\dot{\gamma}_y - K_{\rho}\dot{\gamma}_y - (K_{xc} - K_{\rho}\beta)\dot{\gamma}_x \end{bmatrix} \quad (3.7)$$

and, for the controlled system, Eq. (3.4) becomes

$$\begin{bmatrix} Q_{Dx} \\ Q_{Dy} \end{bmatrix} = \begin{bmatrix} \ddot{\gamma}_x + K_{\rho}\dot{\gamma}_x + (K_{\delta} + m\beta^2)\gamma_x - ((2-n)\beta\dot{\gamma}_y + K'_{xc}\gamma_y) \\ \ddot{\gamma}_y + K_{\rho}\dot{\gamma}_y + (K_{\delta} + m\beta^2)\gamma_y + ((2-n)\beta\dot{\gamma}_x + K'_{xc}\gamma_x) \end{bmatrix} \quad (3.8)$$

where $K'_{xc} \triangleq K_{xc} - K_{\rho}\beta$. Therefore, the cross-coupling gain K'_{xc} for a spinning vehicle can be related directly to the gains used to control the equivalent gyrostator.

Equations (3.7) and (3.8) are identical in form to those derived in Ref. 7 for the control of a spinning symmetric body by use of the Frequency Symmetry technique. Those equations are written as

$$\begin{bmatrix} Q_{Cx} \\ Q_{Cy} \end{bmatrix} = \begin{bmatrix} -K_p & -K_v & K_v\beta\left(1 - \frac{n}{2}\right) & 0 \\ -K_v\beta\left(1 - \frac{n}{2}\right) & 0 & -K_p & -K_v \end{bmatrix} \begin{bmatrix} \gamma_x \\ \dot{\gamma}_x \\ \gamma_y \\ \dot{\gamma}_y \end{bmatrix} \quad (3.9)$$

and

$$\begin{bmatrix} Q_{Dx} \\ Q_{Dy} \end{bmatrix} = \begin{bmatrix} \ddot{\gamma}_x + K_v\dot{\gamma}_x + (K_p + m\beta^2)\gamma_x - (2-n)\beta\left(\dot{\gamma}_y + \frac{K_v}{2}\gamma_y\right) \\ \ddot{\gamma}_y + K_v\dot{\gamma}_y + (K_p + m\beta^2)\gamma_y + (2-n)\beta\left(\dot{\gamma}_x + \frac{K_v}{2}\gamma_x\right) \end{bmatrix} \quad (3.10)$$

Contrails

Frequency Symmetry has set the cross-coupling gain K'_{xc} at $(2-n)\beta K_v/2$. The advantage is that the operating roots of the characteristic equation of (3.10) vs $n\beta$ lie in a vertical line a distance $K_v/2$ from the $j\omega$ -axis for any choice of K_p and K_v . This is the condition that resulted in minimum system sensitivity to gain and h/I_t changes, found through trial and error for the gyrostat characteristic equation.

Lange, Fleming, and Parkinson point out the relative insensitivity of controlled system response to the choice of K_p and K_v . The criteria of stability, good damping, and short response time are met by keeping the ratio $24 > K_p/K_v > 1.2$, a range of 20:1. With reference to their results, K_p and K_v were set at 14.4 sec^{-2} and 10 sec^{-1} , respectively. Figure 7 illustrates the response of a linear control system with the above values of K_p and K_v as simulated on an analog computer.

Steady-state response to disturbing moments \vec{Q}_D was also investigated [7]. For an inertial torque,

$$Q_{DIx} = Q_{DI} \cos \beta t$$

$$Q_{DIy} = Q_{DI} \sin \beta t$$

and for a body-fixed torque,

$$Q_{DBx} = Q_{DB}$$

$$Q_{DBy} = Q_{DB}$$

the steady-state error in γ was found to be inversely proportional to K_p :

$$\gamma_x(t \rightarrow \infty) \doteq \frac{Q_{DB}}{K_p} + \frac{Q_{DI}}{K_p} \cos \beta t \quad (3.11)$$

$$\gamma_y(t \rightarrow \infty) \doteq \frac{Q_{DB}}{K_p} + \frac{Q_{DI}}{K_p} \sin \beta t \quad (3.11)$$

Cont.

The controller, therefore, can never completely eliminate errors caused by these disturbances. Q_{DB} also includes the first-order effects of products of inertia, as seen from Eqs. (2.6).

Figure 8 is an analog simulation of the linear controller responding to initial conditions, with Q_{DB} and Q_{DI} acting on the body. The steady-state error is an ellipse with axes of length Q_{DIx}/K_p and Q_{DIy}/K_p (in this case a circle because $Q_{DIx} = Q_{DIy}$) and whose center is displaced by Q_{DBx}/K_p and Q_{DBy}/K_p from the origin.

B. Control of an Automatic Mass Trim System

A control law of the type in Eq. (3.9) is unable to maintain zero-attitude error in the presence of body-fixed moments or products of inertia, as discussed above. Equations (2.14) and (2.33) related misalignments between the body axis of maximum inertia and the autocollimator null axis to apparent products of inertia and, consequently, these misalignments are also a source of steady-state error.

By positioning movable masses inside the vehicle to create off-setting moments, as shown in Eqs. (2.10), the steady-state error can be eliminated. A linear control law is proposed in this section for such a system. Mass velocity (speed and direction) rather than mass position are controlled. The necessity to estimate the magnitude and direction of the apparent body-fixed moment is thereby eliminated, and knowledge of the position of each mass is also unnecessary.

Because the zero-frequency components of the steady-state error are directly proportional to \vec{Q}_{DB} , a control law was chosen in the form of

$$\dot{z}_y = K_M \gamma_x e^{-at} \quad (3.12)$$

$$\dot{z}_x = -K_M \gamma_y e^{-at}$$

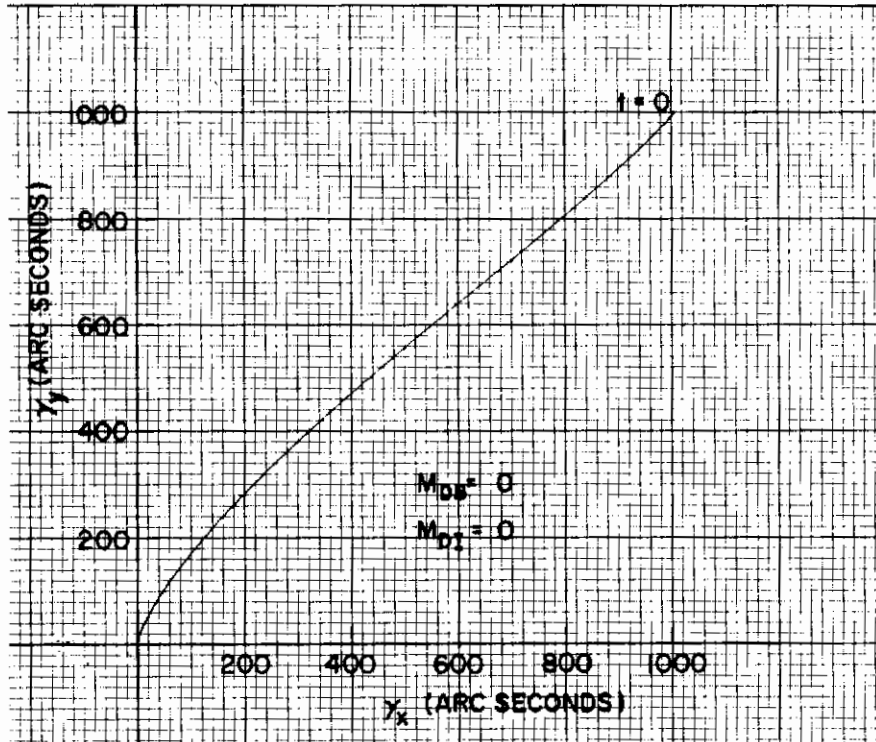


Fig. 7. SPINNING-VEHICLE CONTROLLER SIMULATION WITHOUT DISTURBING MOMENTS.

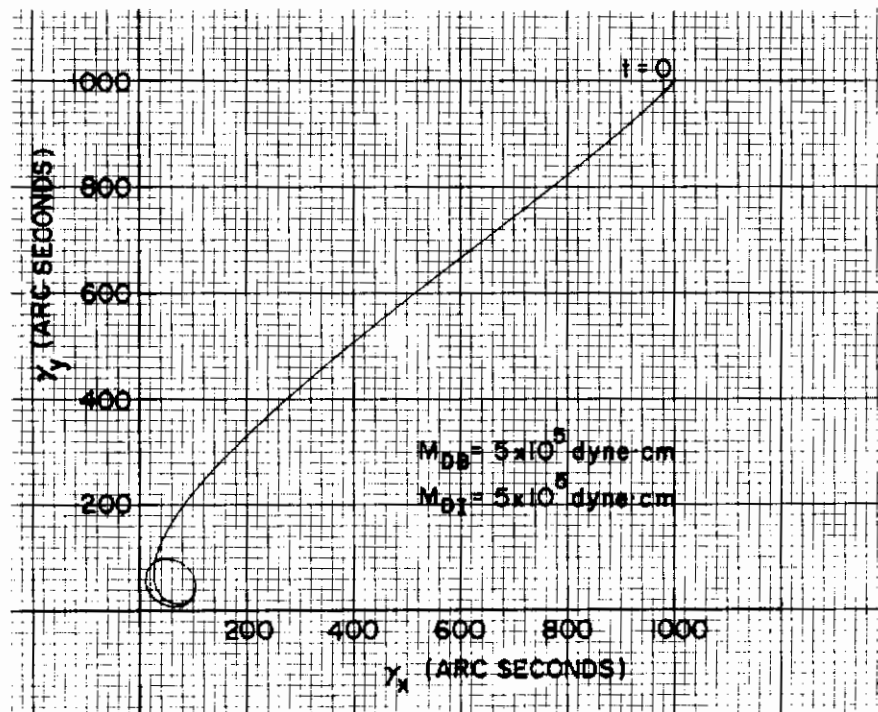


Fig. 8. SPINNING-VEHICLE CONTROLLER SIMULATION WITH BODY-FIXED AND INERTIAL DISTURBING MOMENTS.

Controls

where $Z_{x,y}$ refers to the notation in Fig. 2 and Eqs. (2.10). This results in an integral controller, described in Ref. 7 as a method of eliminating steady-state errors. The control moment applied by the mass pair is

$$\begin{bmatrix} Q_{Mx} \\ Q_{My} \end{bmatrix} = \begin{bmatrix} \frac{2\mu R\beta^2 K_M}{I_t} \int_0^t \gamma_x(\sigma) e^{-a\sigma} d\sigma \\ -\frac{2\mu R\beta^2 K_M}{I_t} \int_0^t \gamma_y(\sigma) e^{-a\sigma} d\sigma \end{bmatrix} \quad (3.13)$$

The e^{-at} term acts as a filter to separate the zero-frequency and spin-frequency components of γ .

The equations for the controlled body now become

$$\begin{bmatrix} Q_{Dx} \\ Q_{Dy} \end{bmatrix} = \begin{bmatrix} \ddot{\gamma}_x + \left(K_v + \frac{Q_T K_M}{\beta^2} e^{-at} \right) \dot{\gamma}_x + \left(K_p + m\beta^2 - \frac{aQ_T K_M}{\beta^2} e^{-at} \right) \gamma_x \\ + Q_T K_M \int_0^t \gamma_x(\sigma) e^{-a\sigma} d\sigma - (2-n)\beta \left(\dot{\gamma}_y + \frac{K_v}{2} \gamma_y \right) \\ \ddot{\gamma}_y + \left(K_v - \frac{Q_T K_M}{\beta^2} e^{-at} \right) \dot{\gamma}_y + \left(K_p + m\beta^2 + \frac{aQ_T K_M}{\beta^2} e^{-at} \right) \gamma_y \\ - Q_T K_M \int_0^t \gamma_y(\sigma) e^{-a\sigma} d\sigma + (2-n)\beta \left(\dot{\gamma}_x + \frac{K_v}{2} \gamma_x \right) \end{bmatrix} \quad (3.14)$$

where $Q_T \triangleq 2\mu R\beta^2 / I_t$.

The trim-system gains K_M and a can be chosen based on a root locus analysis. Because a is the spin-frequency filter time constant,

Conrails

its value can be limited to $0 < a < \beta$. Stability and response of the system then can be determined by plotting a series of K_M root loci, each for a different value of a .

Figures 9 to 12 are root loci for the eighth-order characteristic equation of (3.14). Calculated with a polynomial root-solver package on a Sigma V computer, the loci vs K_M were plotted for four selected values of a . Other system parameters are as follows:

$$\begin{aligned}K_p &= 14.4 \text{ sec}^{-2} & n &= 1.804 \\K_v &= 10.0 \text{ sec}^{-1} & \beta &= 1.0 \text{ rad/sec} \\m &= 0.804 & Q_T &= 1.981 \times 10^{-3} \text{ cm}^{-1} \text{ sec}^{-2}\end{aligned}$$

Selection of K_M is made once an appropriate a is chosen. To keep the trim system from tracking spin-frequency oscillations, a should be kept as small as possible. The root loci indicate that system stability and speed of response degrade as a is lowered; hence, a tradeoff value must be accepted.

Figure 13 is an analog simulation of trim-system response for $a = 0.2 \text{ sec}^{-1}$ and $K_M = 37 \text{ cm/sec}^2/\text{rad}$. The root locus for $a = 0.2 \text{ sec}^{-1}$ (Fig. 10) indicates the operating roots. Response to initial conditions and step inputs of inertial and body-fixed moments is satisfactory. The trim system oscillates only slightly, caused by the inertial torque. Under actual operating conditions, inertial torques are at least an order of magnitude less than those simulated here, making trim-system motion negligible.

The basic instability of a moving mass trim system is illustrated in Fig. 14 which is a root locus vs K_M with K_p and $K_v = 0$. This instability is caused by the $Q_T \ddot{z}_{x,y}/\beta^2$ terms. Stability of a vehicle with an automatic mass trim system, therefore, is dependent on the attitude control loop to damp these disturbing moments.

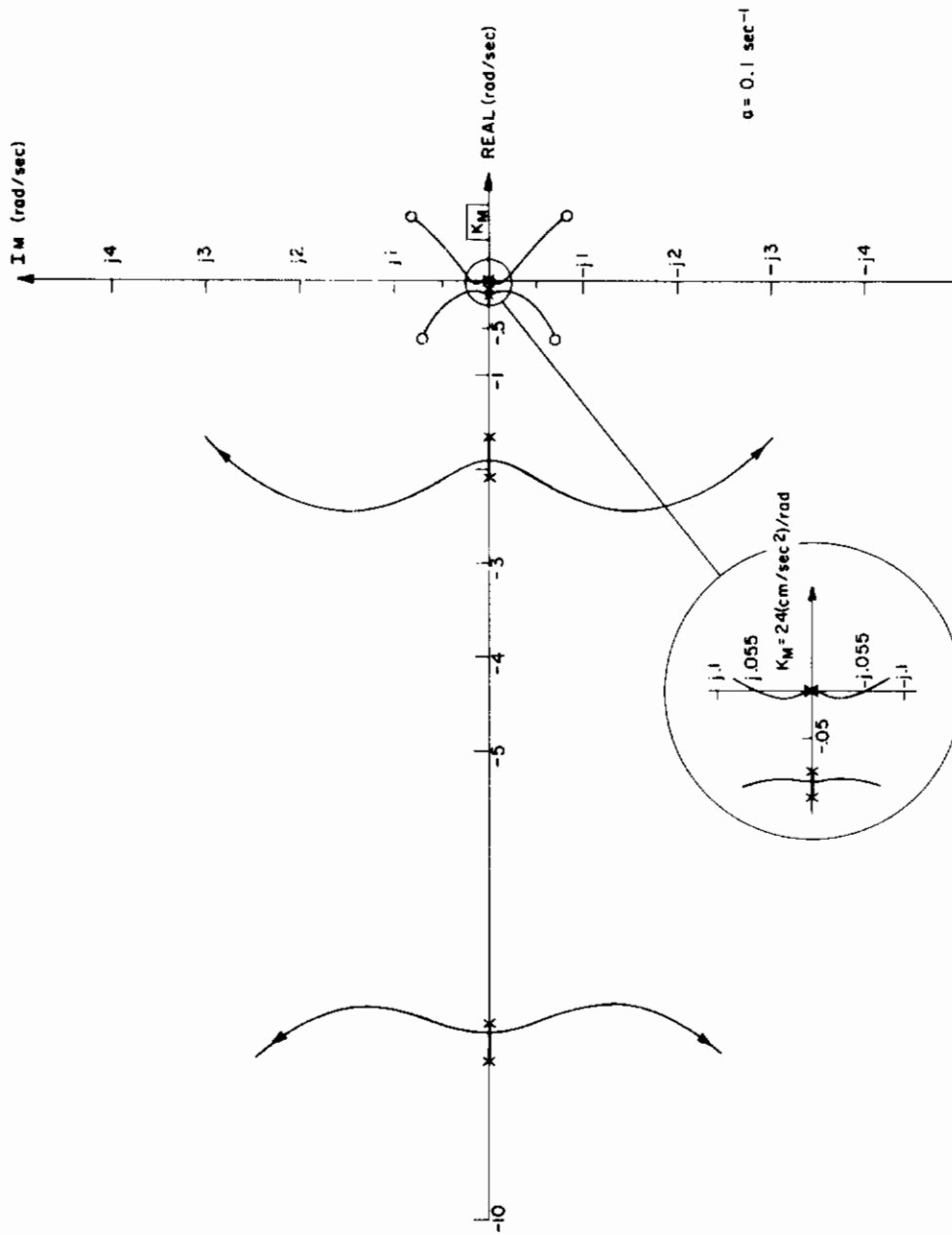


Fig. 9. ROOT LOCUS OF CHARACTERISTIC EQUATION OF (3.14) VS K_M .

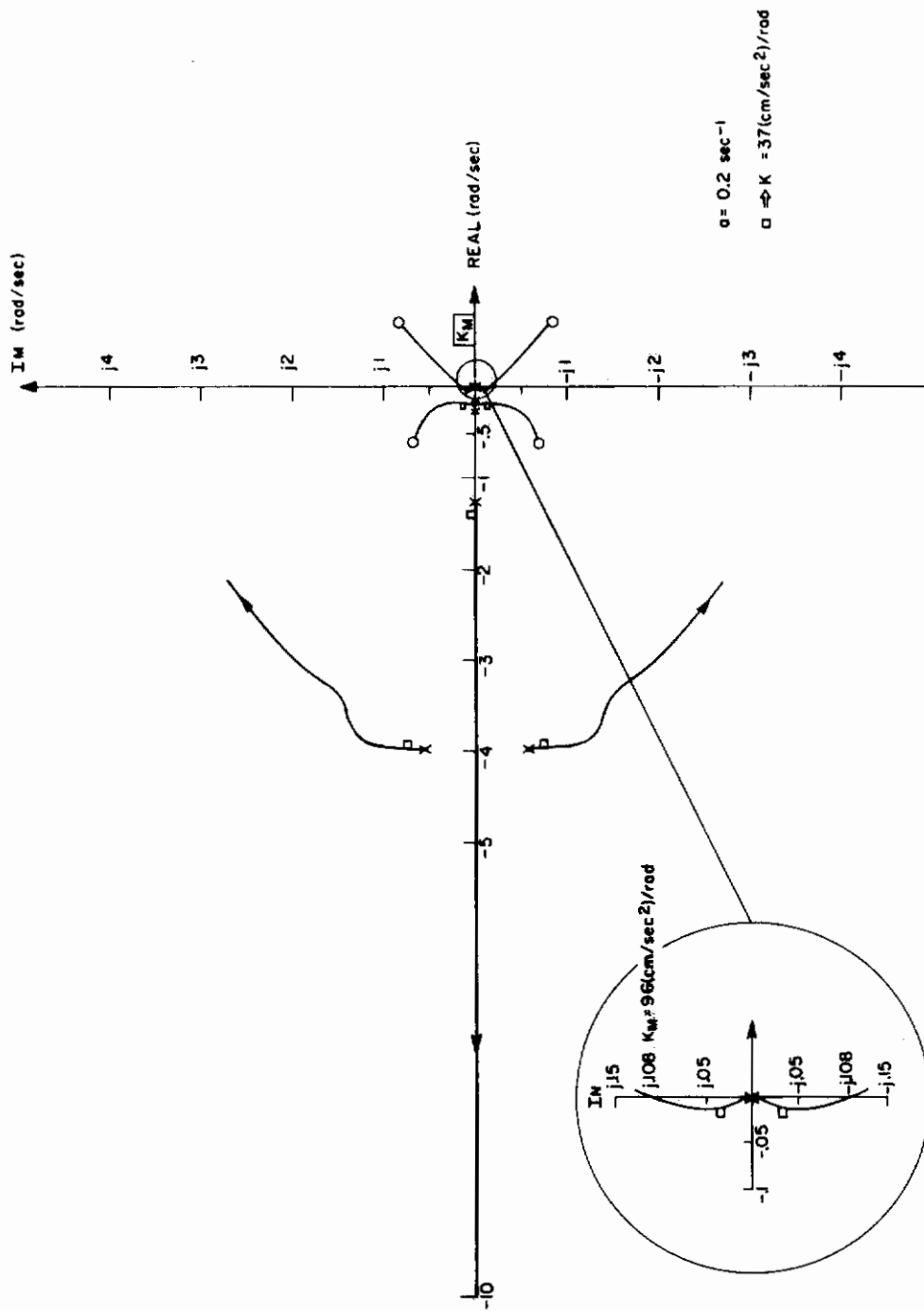


Fig. 10. ROOT LOCUS OF CHARACTERISTIC EQUATION OF (3.14) VS K_M .

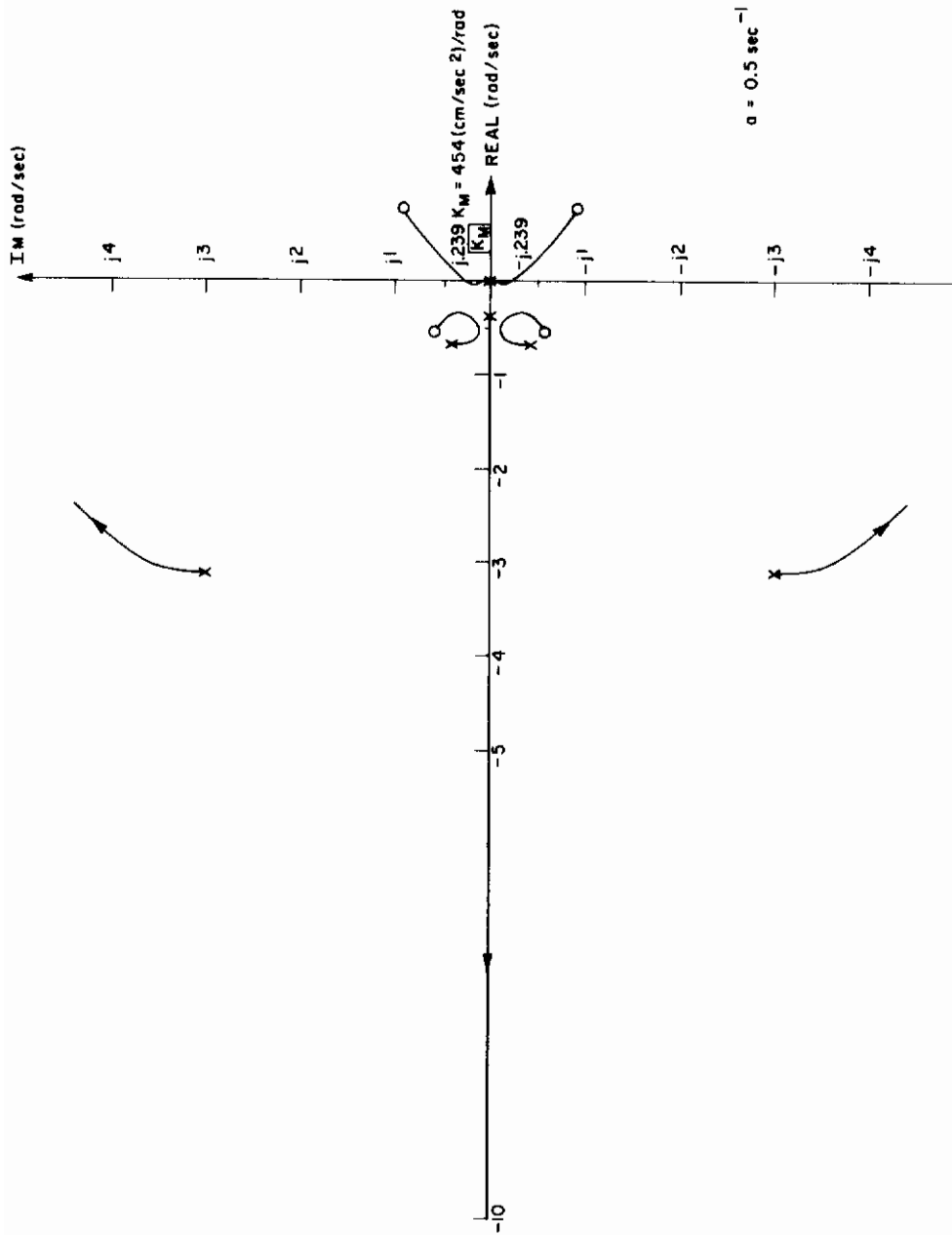


Fig. 11. ROOT LOCUS OF CHARACTERISTIC EQUATION OF (3.14) VS K_M .

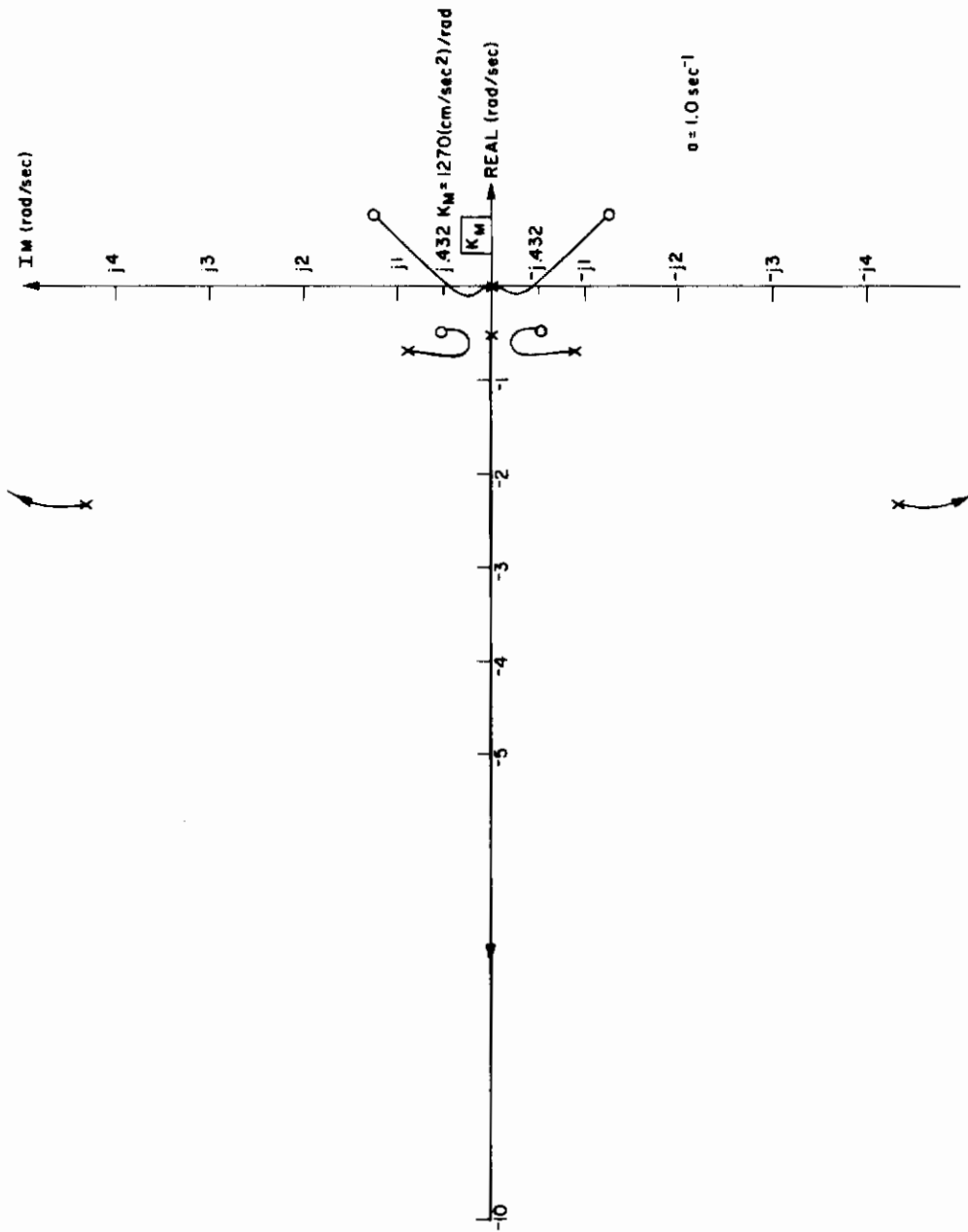
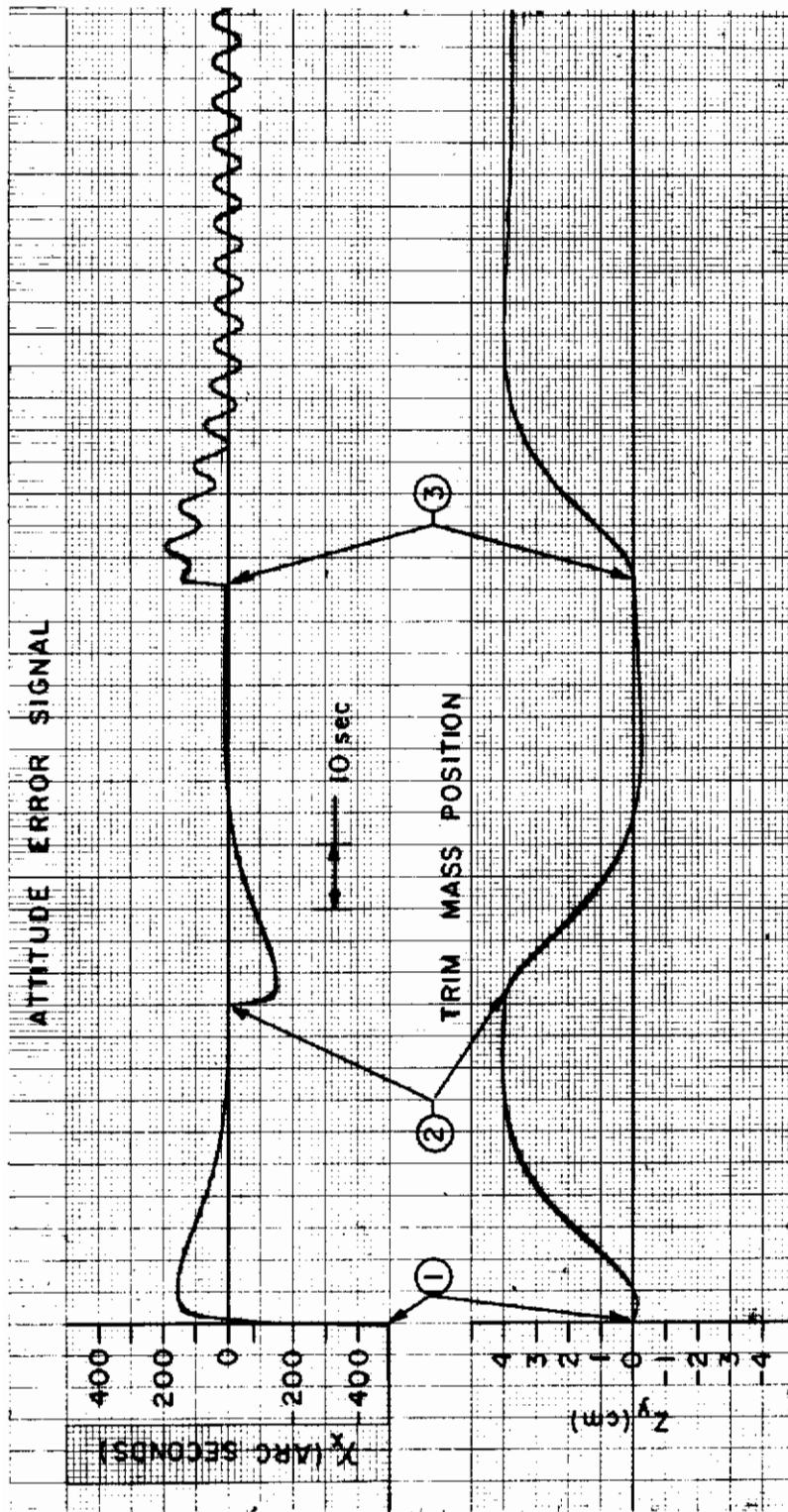


Fig. 12. ROOT LOCUS OF CHARACTERISTIC EQUATION OF (3.14) VS K_M .



① $\gamma_x (t=0) = -500$ ARC SECONDS, $M_{DB} = 5 \times 10^5$ dyne cm

② STEP RESPONSE, $M_{DB} = -5 \times 10^5$ dyne cm

③ STEP RESPONSE, $M_{DB} = 5 \times 10^5$ dyne cm, $M_{DI} = 2.5 \times 10^5$ dyne cm

Fig. 13. AUTOMATIC MASS TRIM SYSTEM RESPONSE.

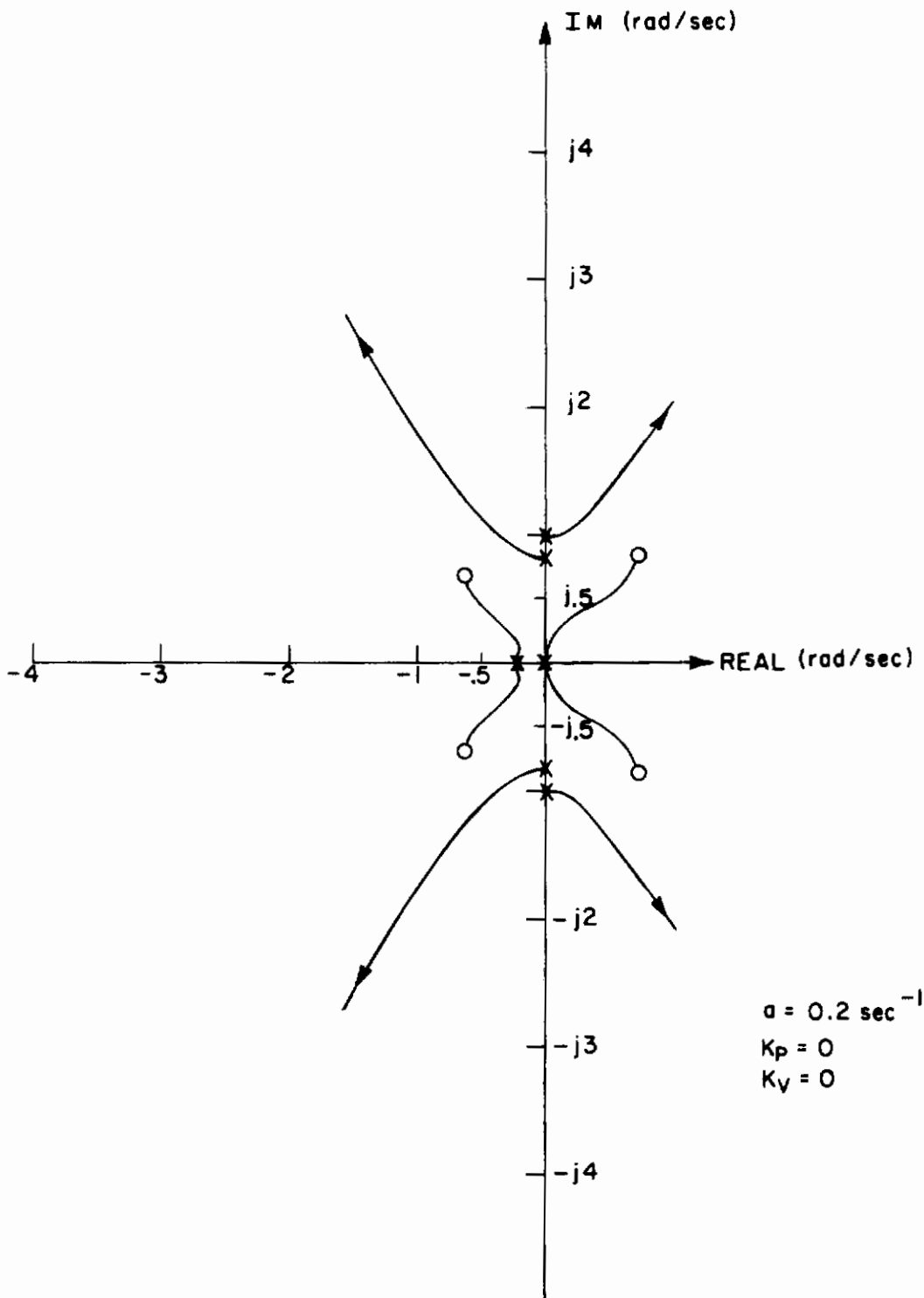


Fig. 14. ROOT LOCUS OF CHARACTERISTIC EQUATION OF (3.14) VS K_M WITHOUT ATTITUDE CONTROL LOOP. An AMTS, using the control law of Eq. (3.12), is unstable for $K_M > 0$ if there is no active control.

C. Controller Stability with Saturation Nonlinearities

In addition to the seven simplifying assumptions listed in Chapter II.A, the linear controller described above assumes that unlimited control torque is available. Although this assumption may be satisfactory for many control systems, it is not generally valid for the SVS. With $K_p = 14.4 \text{ sec}^{-2}$, the torquers on the Kearfott T4101 gyro used as a CMG are in saturation for $\gamma > 20$ arc seconds. During the damping of initial conditions, γ may be greater than 4000 arc seconds.

Limiting the control torque is equivalent to lowering the loop gain. Figure 15 shows the relationship between effective K_p and γ for a nonlinearity of this type. The effects on the system are the following.

- (1) Steady-state errors are much larger for the nonlinear system (without the use of automatic mass trimming).
- (2) Inertial torques larger than the maximum available control torque cause the system to become uncontrollable.
- (3) Gains chosen for an AMTS used with a linear controller may be unstable for the torquer-saturation case because of the inherent instability of an AMTS (from the locus in Fig. 14).

Figures 16 and 17 are root loci similar to those in Figs. 9 to 12 except that K_p has been reduced to approximate the response of a controller with torque saturation at $\gamma = 200$ and 2000 arc seconds, respectively. This is an inexact method to determine system response, however, and is used here solely to illustrate the possibility of instabilities. Final selection of gains should be based on the results of an analog or digital simulation that includes the appropriate saturation functions. Note that, for $a = 0.2 \text{ sec}^{-1}$, the system is unstable for $K_M > 15 \text{ (cm/sec}^2\text{)/rad}$ at 200 arc seconds and $K_M > 0$ at 2000 arc seconds. As before, the instability results from both the phase lag and the $Q_{T_{x,y}} \ddot{z} / \beta^2$ terms as the trim system tracks spin-frequency oscillations.

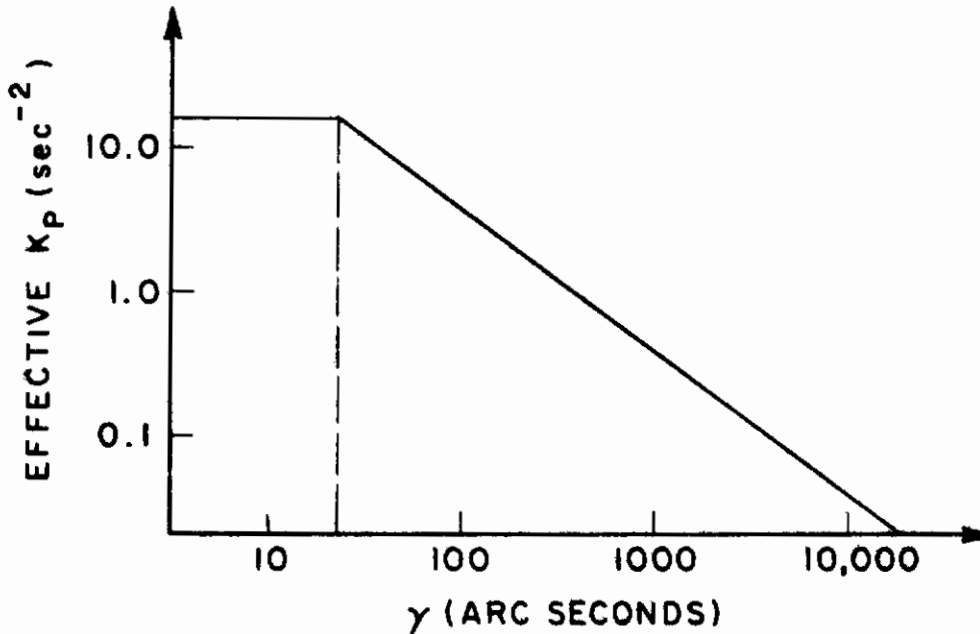


Fig. 15. EFFECT OF TORQUER SATURATION ON K_p .

Three methods can be employed to extend the region of stability.

- (1) Lengthen the time constant of the β -filter (decrease a). The sensitivity of the AMTS to oscillations at spin frequency is reduced, but response time is increased as a result.
- (2) Limit the maximum velocity of the masses, thereby limiting acceleration torques. There is little effect on system quasi-steady-state response because mass motion during steady-state operation is very slow.
- (3) Use multiple gains, changing them as the rms error signal changes. Best overall performance would be obtained but implementation is more complex.

Figure 18 is a locus vs K_M for $a = 0.1 \text{ sec}^{-1}$. An analog simulation (Fig. 19) verifies the selected values of K_M and a and indicates that, with the addition of item (2) above, the system remains stable. Figure 20 is a simulated response to initial conditions and disturbing moments for $K_M = 2 \text{ cm-sec}^{-2}/\text{rad}$, $a = 0.1 \text{ sec}^{-1}$, and $|\dot{z}_{x,y}| \leq 0.312 \text{ cm/sec}$.

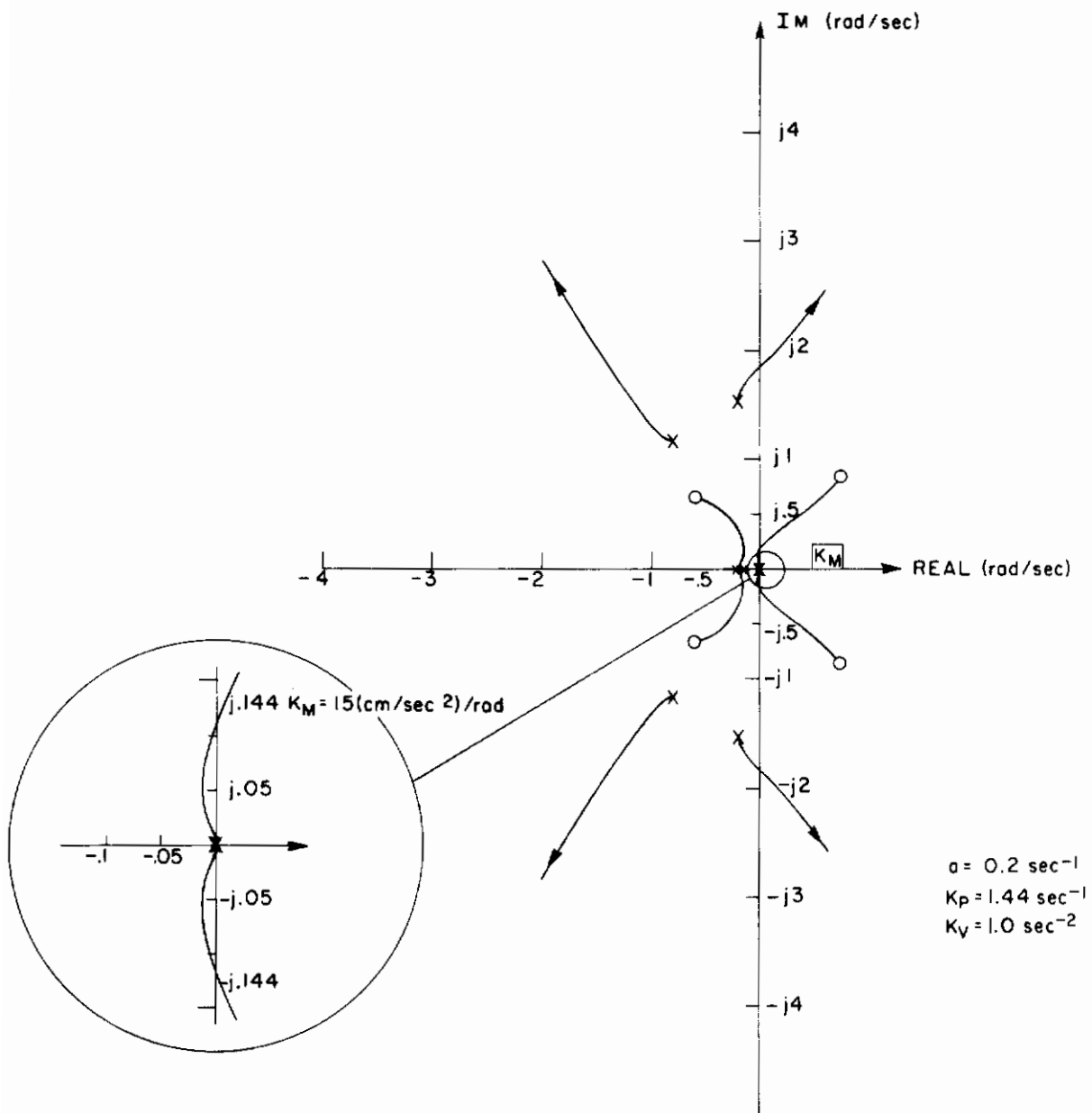


Fig. 16. ROOT LOCUS OF CHARACTERISTIC EQUATION OF (3.14) VS K_M WITH $K_P = 1.44 \text{ sec}^{-1}$ TO APPROXIMATE CONTROLLER TORQUE SATURATION AT $\gamma = 200$ ARC SECONDS.

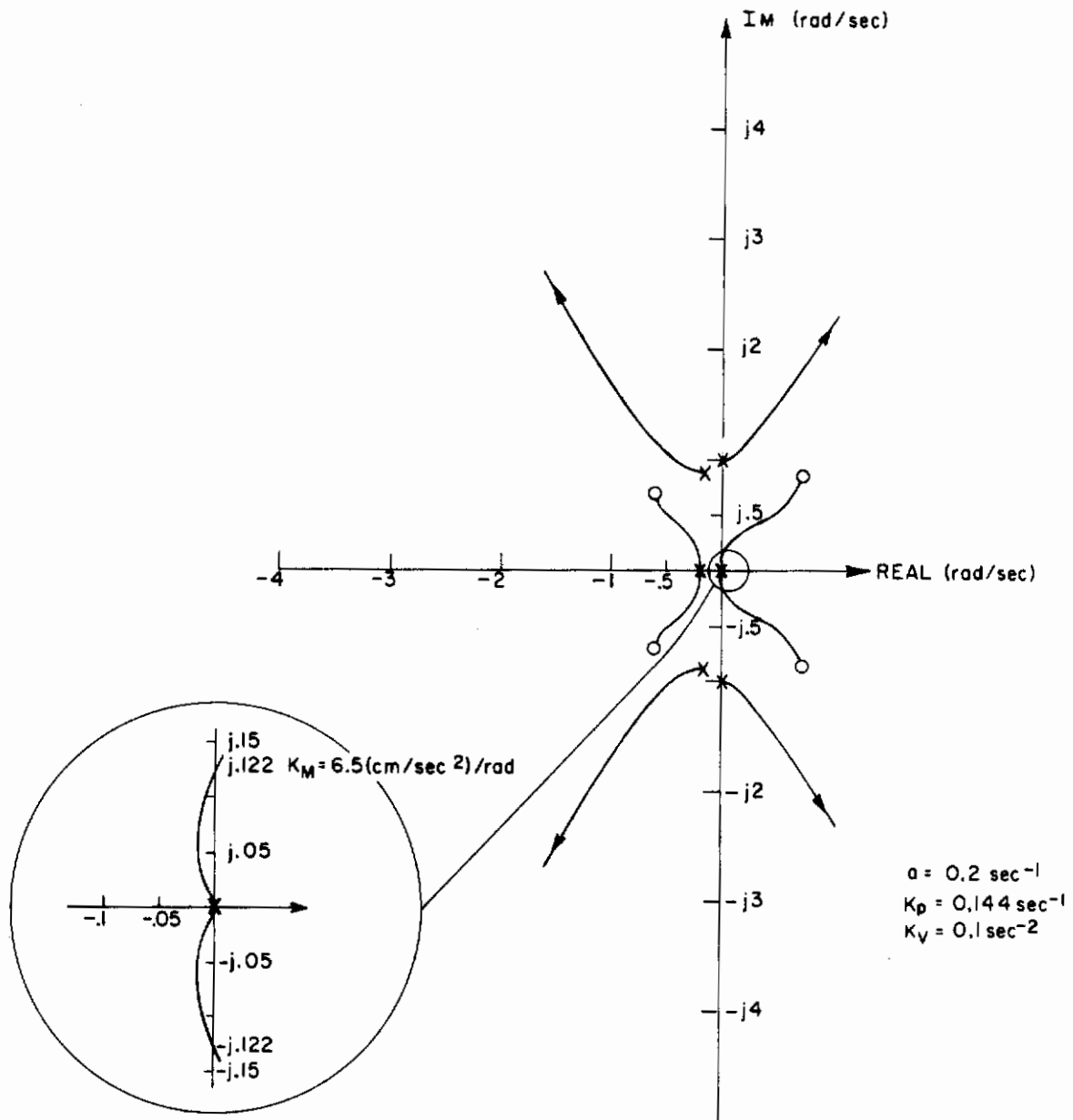


Fig. 17. ROOT LOCUS OF CHARACTERISTIC EQUATION OF (3.14) VS K_M WITH $K_p = 0.144 \text{ sec}^{-1}$ TO APPROXIMATE CONTROLLER TORQUE SATURATION AT $\gamma = 2000$ ARC SECONDS.

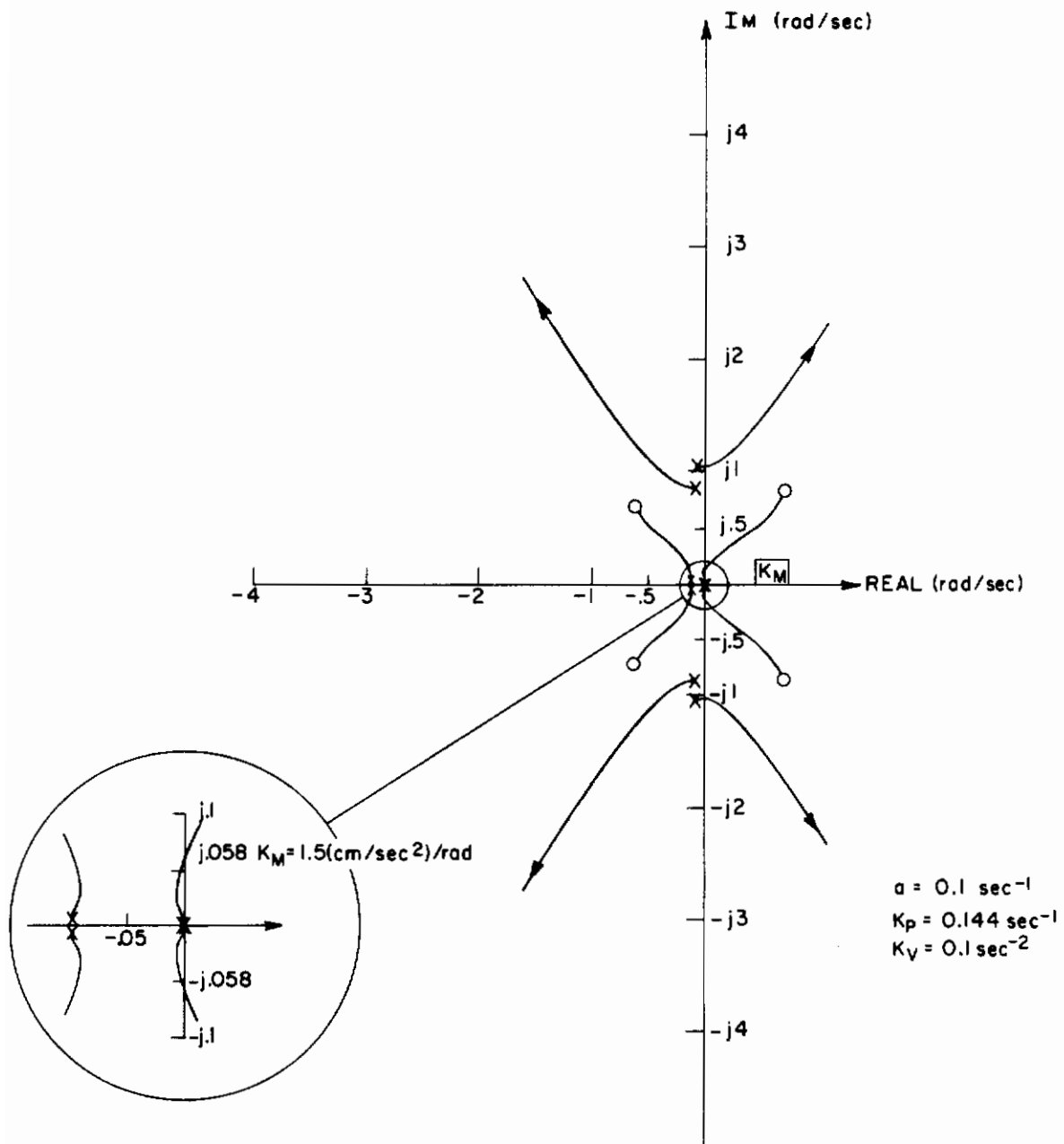


Fig. 18. ROOT LOCUS OF CHARACTERISTIC EQUATION OF (3.14) VS K_M WITH $K_p = 0.144 \text{ sec}^{-1}$. System is stable using smaller values of K_M and a .

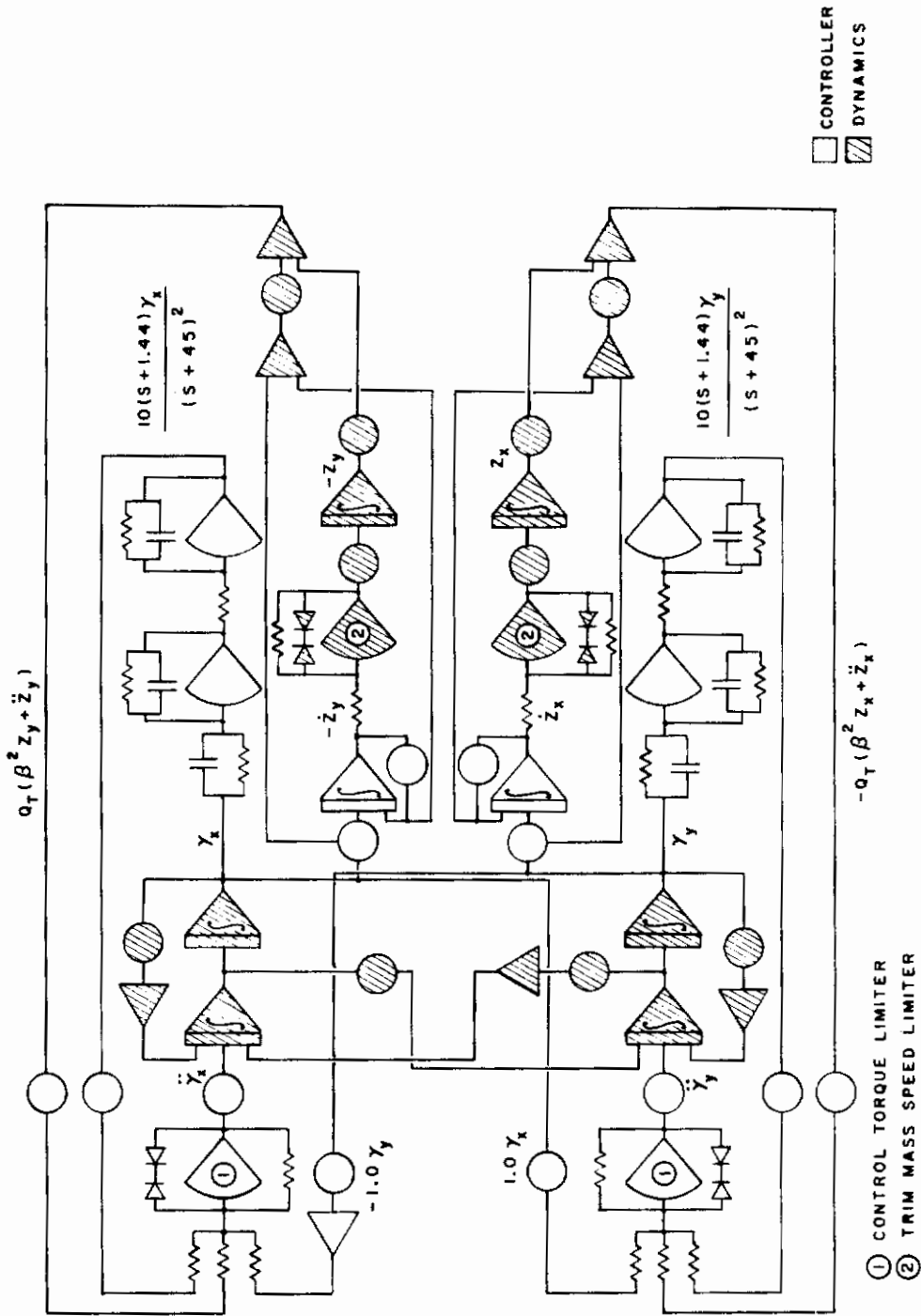
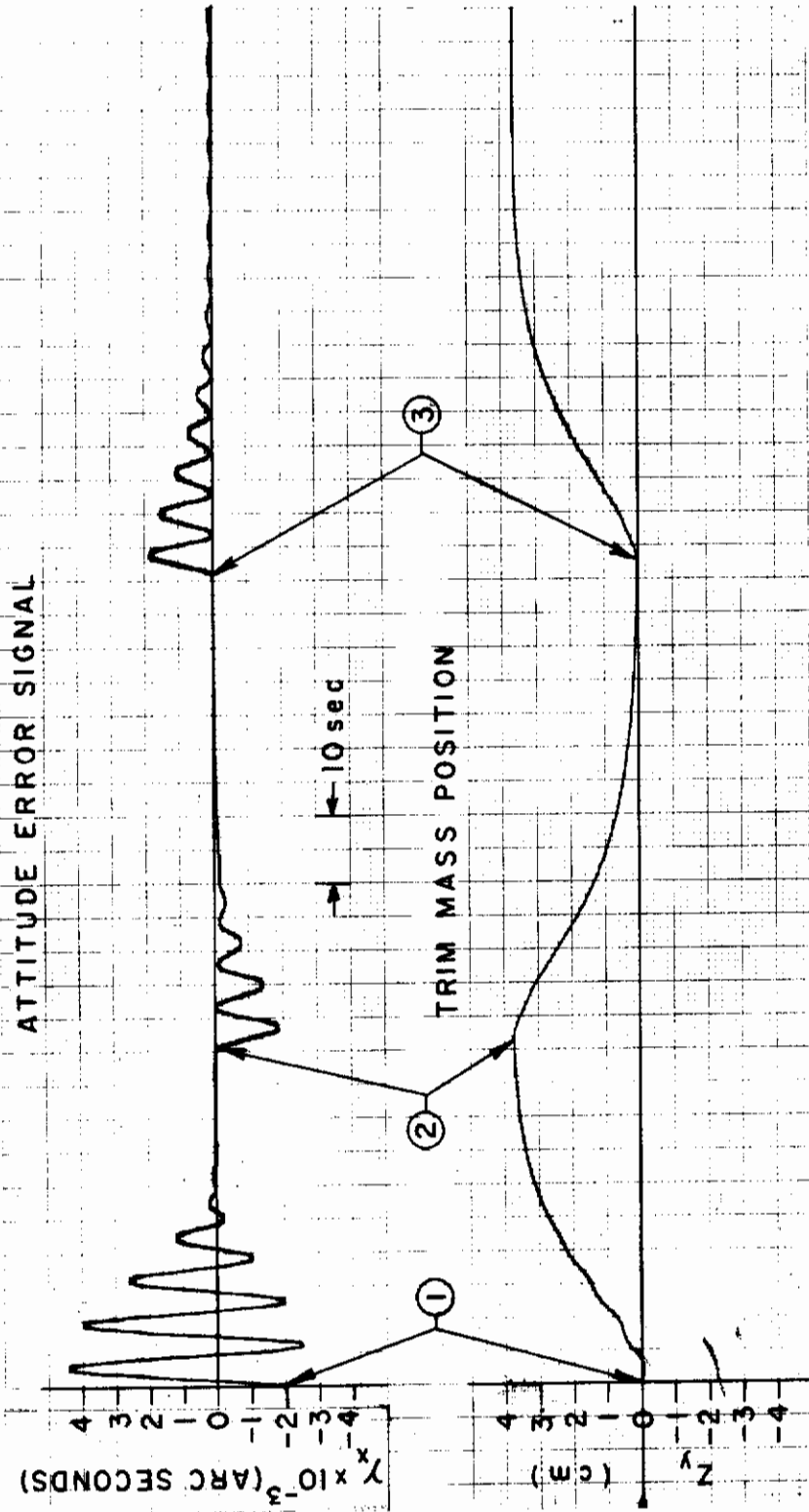


Fig. 19. NONLINEAR CONTROL-SYSTEM COMPUTER SIMULATION.



- ① $\gamma_x (t=0) = -2000$ ARC SECONDS, $M_{DB} = 5 \times 10^5$ dyne cm
- ② STEP RESPONSE, $M_{DB} = -5 \times 10^5$ dyne cm
- ③ STEP RESPONSE, $M_{DB} = 5 \times 10^5$ dyne cm, $M_{DI} = 5 \times 10^4$ dyne cm

Fig. 20. AUTOMATIC MASS TRIM SYSTEM RESPONSE.

Contrails

7

Chapter IV

DESCRIPTION OF EXPERIMENT

Analytical results described in Chapter II and control-system design and simulation discussed in Chapter III verified the feasibility of a precision attitude controller for a symmetric spinning body. For analytical convenience, many of the problems associated with an actual mechanization were simplified or bypassed. Thus, to assess the practicality of the mechanization scheme and to fully study control-system performance in the presence of unknown or difficult to model noise and environmental disturbances, a laboratory simulator was constructed and tested. Section A describes the simulator and the experimental setup; the remainder of the chapter describes the controller mechanization and components. Detailed specifications can be found in the Appendix.

A. Simulator Description and Experimental Setup

1. Description of Simulator

The Spinning Vehicle Simulator consists of a framework built around a central cylindrical core. The control-system components are mounted on both the frame and the hollow core. An externally pressurized spherical air bearing provides three degrees of rotational freedom. A mirror fixed in the laboratory acts as an inertial reference for the two-axis autocollimator used as an attitude sensor. The simulator and its components are illustrated in Figs. 21 and 22.

Care was taken to design the simulator as an inertially symmetric body about the spin axis. All components are located on the two control (intermediate moment of inertia) axes, on a line 45° to these axes, or along the cylinder centerline. Referring to Fig. 21, the symmetry of the design is apparent. When multiple units of a component were employed (such as AMTS units (6), control jets (7), gas tanks (5), and batteries (4)), the control axes were a natural location. One-of-a-kind units (such as the CMG (11), pressure regulator (10), and electronics package (3)) were placed on the 45° lines. The autocollimator

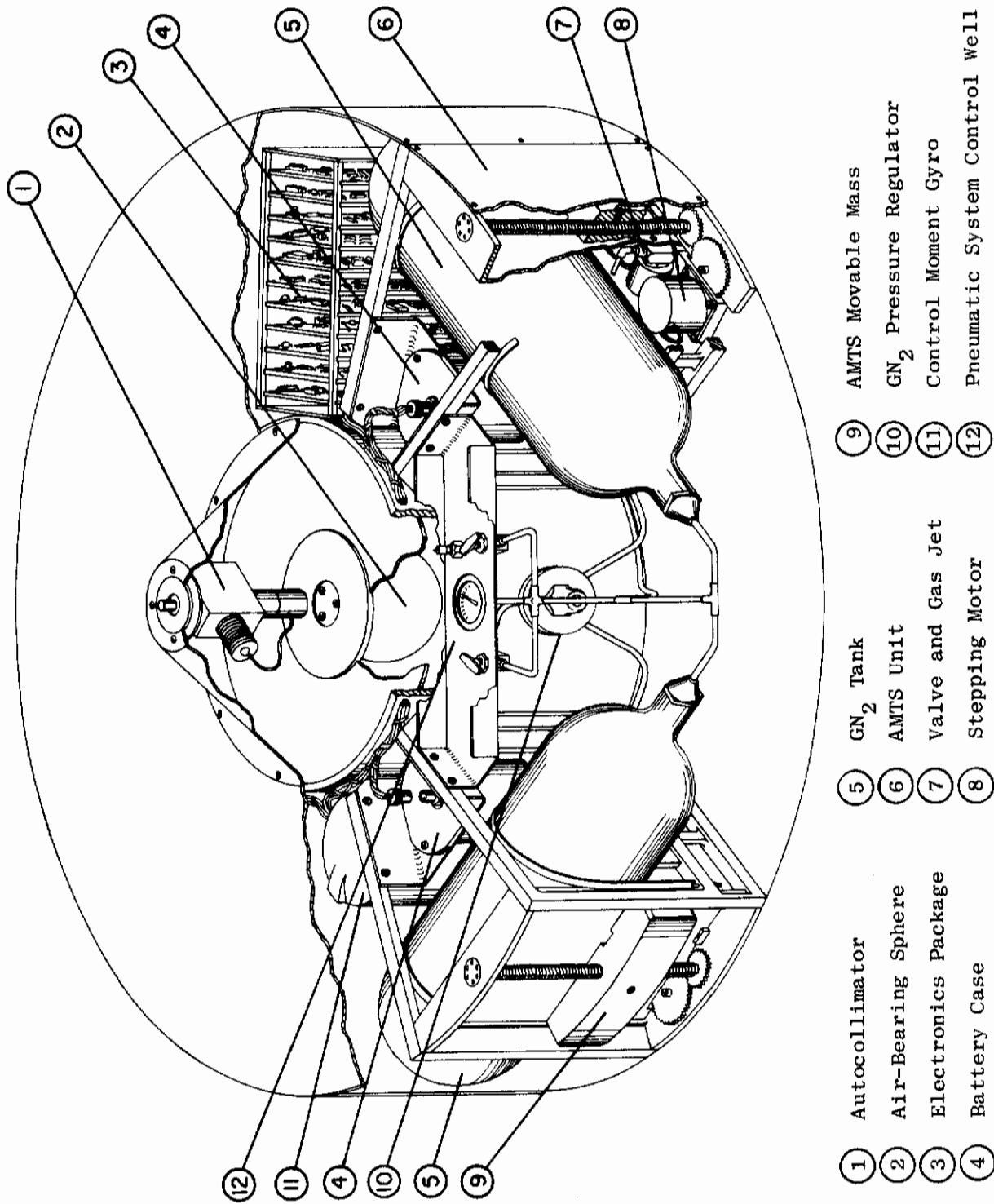


Fig. 21. CUTAWAY VIEW OF SPINNING VEHICLE SIMULATOR.

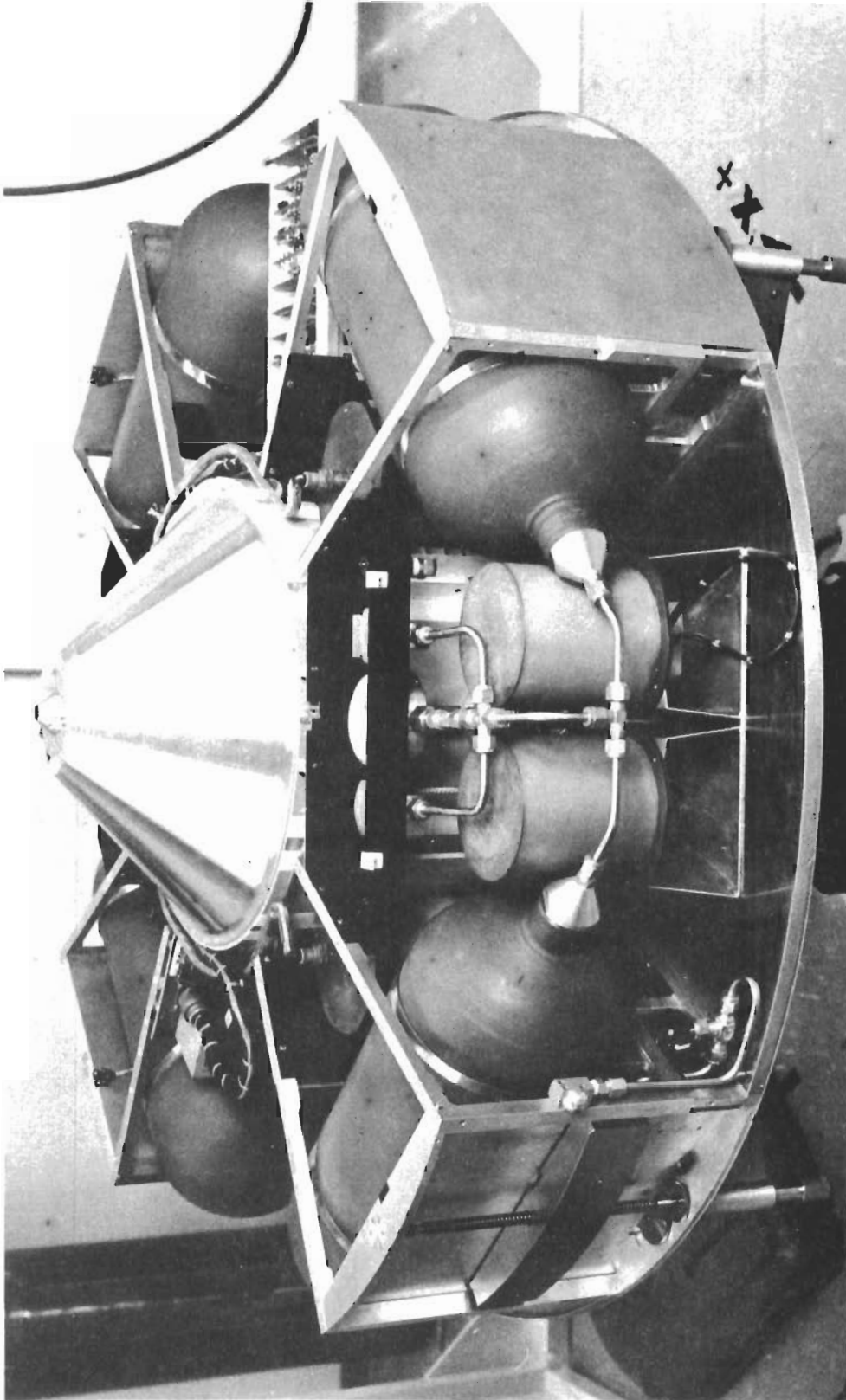


Fig. 22. SPINNING VEHICLE SIMULATOR.

① was most conveniently located on the vehicle centerline. The assumption that $I_{xx} = I_{yy}$ was verified by measurement to better than 1 percent.

Duplication of the low level of orbital disturbing moments, particularly the lack of gravitational or aerodynamic torques, is impossible in the laboratory environment. These problems were considered in the design of the simulator, and they were minimized in the following ways.

- (a) The center of mass can be located as close as 0.08 mm to the center of support (along the Z_B -axis). By operating within 0.01 rad of vertical, gravity torques can be reduced to as little as 8.70×10^3 dyne cm.
- (b) The vehicle has a streamlined outer skin and is located inside a plastic tent so that air currents in the laboratory will not affect operation.

The simulator is operated from a small control panel located in a well just below the upper skin; connectors for external control and power, battery charger, and test points are also located on this panel. Fill and control valves for the nitrogen used as spin and control jet propellant are in an identical well on the opposite side of the vehicle.

2. Experimental Setup

Figure 23 is a photograph of the laboratory simulator and support equipment. To operate the simulator and to obtain performance data, the following additional equipment is required.

- (1) Air-bearing cup and pedestal: Pedestal can be tilted to null the air-bearing turbine torques. The apparent torque caused by the earth's rotation also can be eliminated by tilting the bearing.
- (2) Air-bearing supply filters and pressure regulator.
- (3) Laboratory autocollimator reference mirror: Mirror mount has a two-axis micrometer adjustment and a bubble level to locate the local horizontal. This procedure is necessary if gravitational torques are to be minimized.

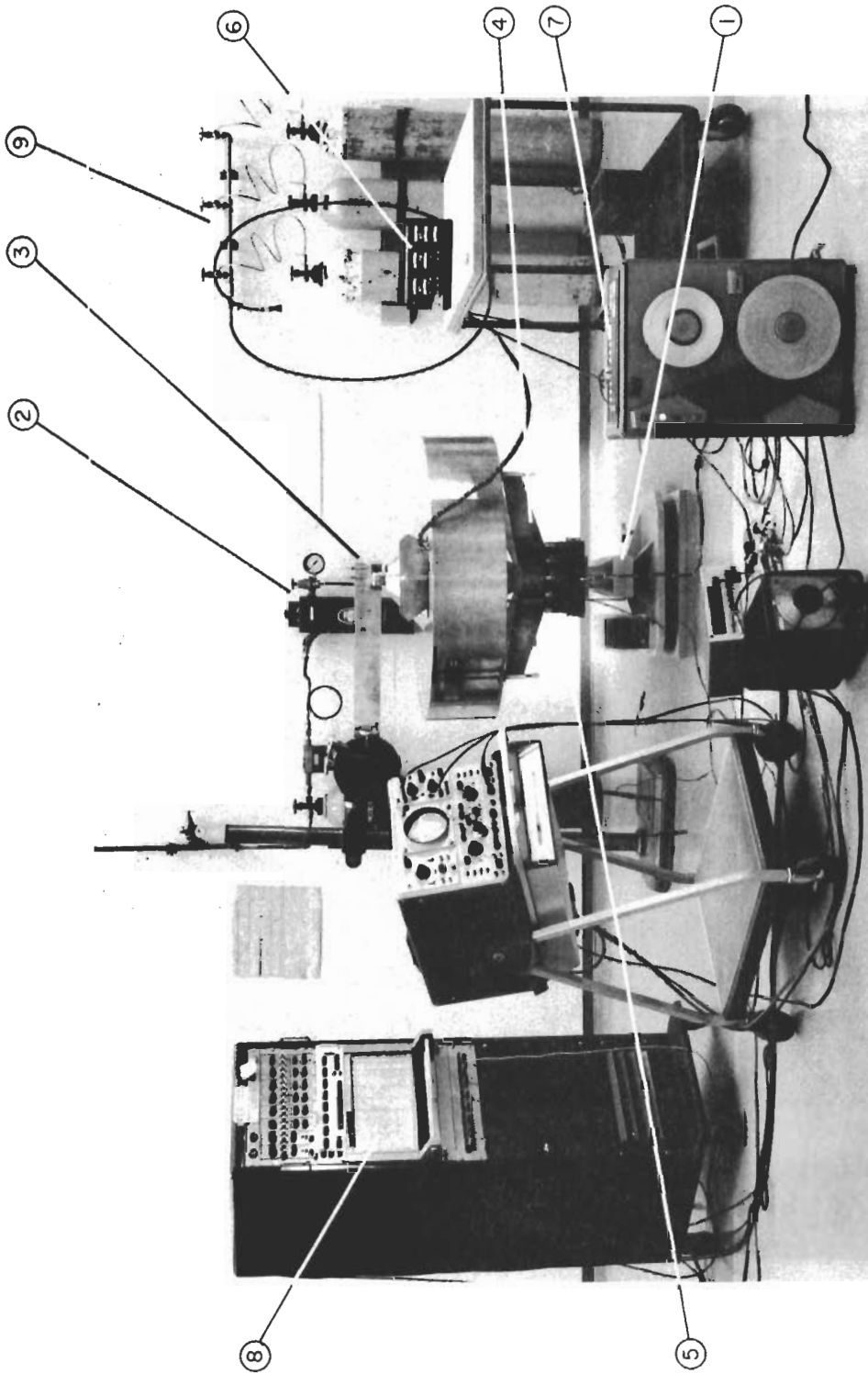


Fig. 23. SPINNING VEHICLE SIMULATOR AND SUPPORT EQUIPMENT.

Contrails

- (4) Vehicle support arms: The simulator is supported off the air bearing when not in use. Alignment of the gyro (as a vertical reference) and autocollimator with the reference mirror is accomplished by micrometers at the ends of the arms.
- (5) Five-channel FM-AM telemetry system: Coarse (100 arc seconds/V) and fine (2 arc seconds/V) autocollimator signals plus gyro gimbal angles are transmitted.
- (6) External control box: Spin-up and caging of gyro, indexing of AMTS, monitoring of autocollimator signals during pre-run alignment, external power, and battery charger are controlled through this device.
- (7) Seven-channel FM-FM magnetic tape recorder: Data from the telemetry plus a reference sine wave are recorded for computer use (power spectral density computation).
- (8) Eight-channel strip-chart recorder: Permanent record of telemetry output is made on this recorder.
- (9) Nitrogen supply: 2500 psi nitrogen bottles and manifold to fill the on-board nitrogen system.
- (10) Plastic enclosure (not shown): Protection from air currents caused by air-conditioning vents directly overhead and by normal laboratory activity is provided by a 7 x 7 x 6 ft wooden frame covered with 2 mil clear mylar.

B. Controller Mechanization

1. Dynamic Range and Multiple Control-Loop Operation

The wide dynamic range of the attitude error, varying from initial conditions of 0.1 rad to a steady-state value of 10^{-5} rad, was the primary problem encountered in the control-system mechanization. Multiple actuators and sensors required for mass trim capability, coarse and fine control, and removal of stored angular momentum from the CMG were a further complication. The mechanization problem is summarized by

- (a) a need to sense angles between 0.2 and 5×10^{-6} rad
- (b) the necessity to damp large initial rate and position errors (the low torque capability CMG used for precision control is unsuitable)

- (c) a requirement to operate two or three control loops simultaneously (the actuators and sensors for which are not independent)[†]

A solution was found by dividing the controller into five modes of operation (see Table 1). Automatic switching between the various sensors and actuators occurs when the state of the system is such that the new sensor or actuator can be employed without loss of control. The criteria used to automatically sequence the mode changes are selected so that operating ranges overlap and the transition is smooth.

2. Controller Components

The large initial rate and position errors cannot be controlled by the autocollimator and CMG. The maximum useful autocollimator angle is ≈ 0.02 rad, 5:1 below initial conditions; CMG torquers can deliver a maximum of 17.85×10^4 dyne cm. Although this eventually would damp the initial conditions, the amplitude of the vehicle attitude excursions would exceed the available air-bearing clearance.

The Kearfott T4101 gyro was designed originally as a vertical reference. The SVS employs it in this mode during the initial erection phase when it is not needed as a CMG and when precision attitude information is unnecessary. A single high-thrust gas jet is used as an actuator. Because precise control is not required, a full four-jet system is superfluous.

When the autocollimator has acquired the laboratory reference mirror, the gyro is no longer needed as a vertical reference and is available for use as a source of control torque. The attitude error is still relatively large, however, usually exceeding 4×10^3 arc seconds. By conservation of angular momentum, the gimbal motion of a CMG

[†] Attitude control-loop operation simultaneous with AMTS is always necessary (see Chapter III.B). AMTS, attitude control, and CMG momentum-dumping loops operate during the gyro unload mode.

Table 1

SPINNING VEHICLE SIMULATOR, MODE DEFINITIONS

Mode	Sensor	Actuator(s)	Transition Requirement	Electronic Subsystems Required [†]
1 Coarse Erection	gyro synchros	single high-thrust gas jet	120 sec time out	A 1,2 E B G D 1 I
2 Coarse Erection	gyro synchros (autocollimator required for transition)	single high-thrust gas jet and AMTS	autocollimator indicating ≤ 6000 sec for 60 sec time out	A 1,2 E B G C H D 2 I
3 Fine Erection	autocollimator	4 low-thrust gas jets and AMTS	autocollimator indicating ≤ 500 sec for 60 sec time out	A 1,2 E B G C H D 2 I
4 Fine Control	autocollimator	gyro torquers and AMTS	gyro synchros exceed 6°	A 1,2,3 G C H F I
5 Gyro Unload	autocollimator gyro synchros	gyro torquers 4 low-thrust gas jets and AMTS	returns to mode 4 when gyro synchros are below 0.25°	A 1,2,3 G B H C I F
2, 3, 4, 5	---	---	return to mode 1 IF synchros exceed 12°	---

[†] ELECTRONIC SUBSYSTEMS

- | | |
|--|--|
| <p>A. Gyro Power Supply</p> <ol style="list-style-type: none"> 1. motor: 115 V 400 Hz 2. synchro excitation: 26 V 400 Hz 3. torquer fixed phase: 57.5 V 400 Hz <p>B. Valve Driver Circuitry</p> <p>C. Stepping Motor Circuitry (V-to-F converter)</p> | <p>D. 60 or 120 Sec Timer Initiated by</p> <ol style="list-style-type: none"> 1. vehicle start-up 2. autocollimator signal <p>E. PWPF Circuitry</p> <p>F. Torquer Power Amp and Modulator</p> <p>G. Synchro Demodulator</p> <p>H. Autocollimator Summing and AGC Functions</p> <p>I. Appropriate Transfer-Function Circuitry</p> |
|--|--|

is proportional to the ratio between the vehicle and gyro angular momenta; thus, a 0.02 rad vehicle motion results in 0.24 rad of gimbal motion. An angle this large is unacceptable because torquer overheating and loss of control torque caused by nonorthogonal gimbals become significant for angles greater than 0.1 rad.

Control torques for autocollimator angles between 4×10^3 and 5×10^2 arc seconds are provided by the four low-thrust gas jets which also are used to unload angular momentum from the CMG. These jets operate from the same nitrogen system as the high-thrust and spin jets; their throat diameters are reduced to give lower thrust. The CMG does not begin torquing until the attitude error is below 5×10^2 arc seconds.

The Automatic Mass Trim System operates independently from and concurrent with the coarse and fine erection loops. The counteraction of body-fixed moments and sensor-vehicle misalignments by the AMTS has been shown experimentally to smooth the transition between the initial erection and fine-control phases.

3. Modes of Operation

The simulator operates in five automatic modes and one manual mode. Table 1 summarizes the control mechanization. The following is a brief description of each of the control modes.

Mode 0. Not an operating mode because the vehicle is stationary and uses external power. Its purpose is to spin up the gyro and align it with the autocollimator so that it becomes an attitude reference; the spin-up would put too much drain on the vehicle batteries if an external power supply was not used. The autocollimator is aligned with the perpendicular to the reference mirror by adjusting the micrometer screws at the ends of the vehicle stand. Mode 1 is begun by switching to internal power, putting the mode sequence switch in the "automatic" position, and disconnecting the external control box cable.

Contrails

- Mode 1. The large rate and position initial conditions are damped. As discussed in Chapter III.C, use of the AMTS during large attitude excursions may cause the system to become unstable; as a result, the trim system does not operate during this mode. Mode 2 begins after a 120 sec time out.
- Mode 2. The vertical gyro and single high-thrust gas jet are used, as in mode 1, but the attitude error has been reduced enough so that the AMTS can operate. Mode 3 begins when the autocollimator has acquired the laboratory reference mirror, indicated when the lamp voltage remains at less than its maximum value for 60 sec.
- Mode 3. The autocollimator is now the attitude reference and the four low-thrust gas jets supply the control torque. The gyro has no function during this mode. Mode 4 begins when the autocollimator signal is less than 500 arc seconds in both axes for 60 sec continuously.
- Mode 4. The vehicle operates in this mode almost continuously after the initial erection phase. Control is maintained by torquing against the gyro. The AMTS is operating. If the gyro gimbal angles exceed 0.15 rad which is the threshold for CMG momentum dumping, mode 5 will be initiated.
- Mode 5. Full attitude control, including CMG torquing and AMTS operation identical to mode 4, is maintained. In addition, the low-thrust gas jets and gyro torquers are pulsed simultaneously so that the gyro gimbal angles are driven to zero. Because the jets and torquers apply equal and opposite torques to the vehicle, a net zero moment results. When both gimbal angles have been reduced to 0.005 rad, the controller returns to mode 4.

During mode 5, the gyro torquers receive signals from the autocollimator for attitude control and from the gyro synchros for unload torquing. Because the unload torque is somewhat below the maximum capability of the torquers (9.45×10^4 dyne cm for unload, 17.85×10^4 maximum), attitude control torque is still available. Normally, the simulator requires ≈ 20 sec to unload the gyro; however, if inertial disturbing moments are applied to the vehicle in mode 5, unloading will take considerably longer because the attitude control signals can swamp the unload signals. If an inertial moment equal to the unload torque is applied, the controller will remain in mode 5 until the moment is removed; if the disturbing moment exceeds 9.45×10^4 dyne cm, the gimbal angles will continue to grow until they reach 0.2 rad. At this threshold, the controller automatically returns to mode 1 to prevent thermal damage to the gyro torquers and power amplifier.

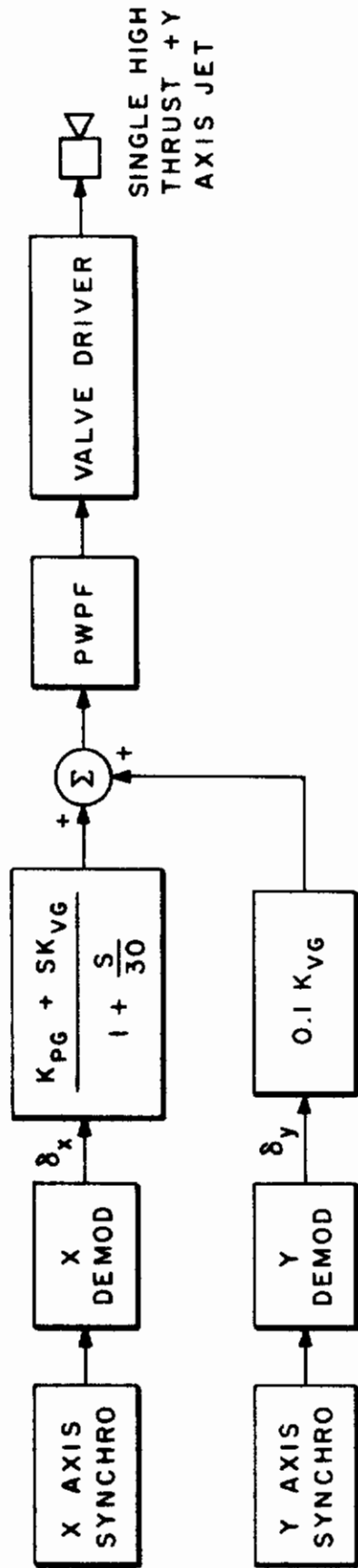
Figures 24 to 28 are block diagrams of the control loops employed in each mode. Values for the gains in the transfer-function blocks and notation regarding which modes the loop is used in also are included.

C. Two-Degree-of-Freedom Control Moment and Vertical Reference Gyroscope

1. Attitude Sensing

The Kearfott T4101 vertical gyro is utilized in the vertical reference mode and as a CMG, as discussed above and in Chapter III.B. Vehicle-attitude information is obtained by two three-phase synchro transmitters, one on each gimbal. Because all gyro power is at 400 Hz, synchro output must be synchronously demodulated to read the gimbal angle. The gyro is mounted in the vehicle, with the synchro axes parallel to the control axes. The gyro \vec{H} at the synchro null is also aligned with the autocollimator null axis; the error is less than 0.01 rad.

In mode 0, the autocollimator signal, referenced to the laboratory mirror, is nulled by adjusting the simulator attitude with the vehicle stand micrometers (Fig. 23, item (4)); consequently, the caged



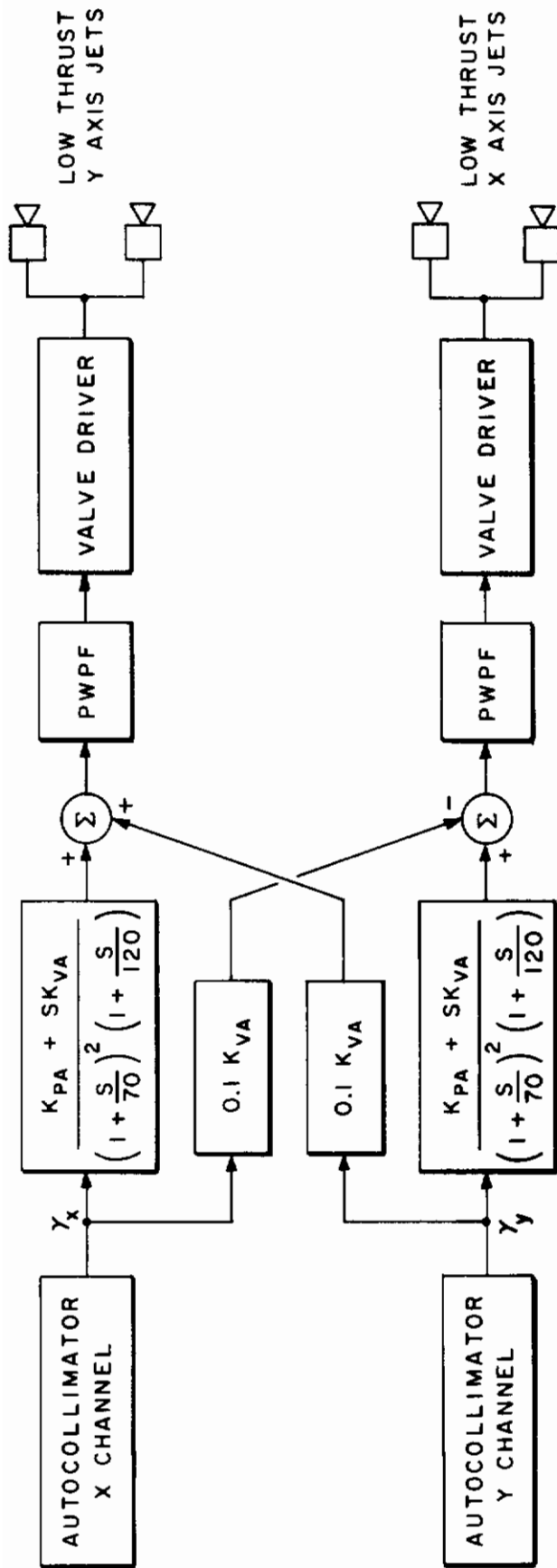
$$K_{PG} = 4.56 \times 10^6 \text{ (dyne cm) / rad}$$

$$K_{VG} = 4.56 \times 10^7 \text{ (dyne cm) / (rad/sec)}$$

MAXIMUM AVAILABLE TORQUE 4.45×10^7 dyne cm

MODES : 1, 2

Fig. 24. COARSE ERECTION LOOP.



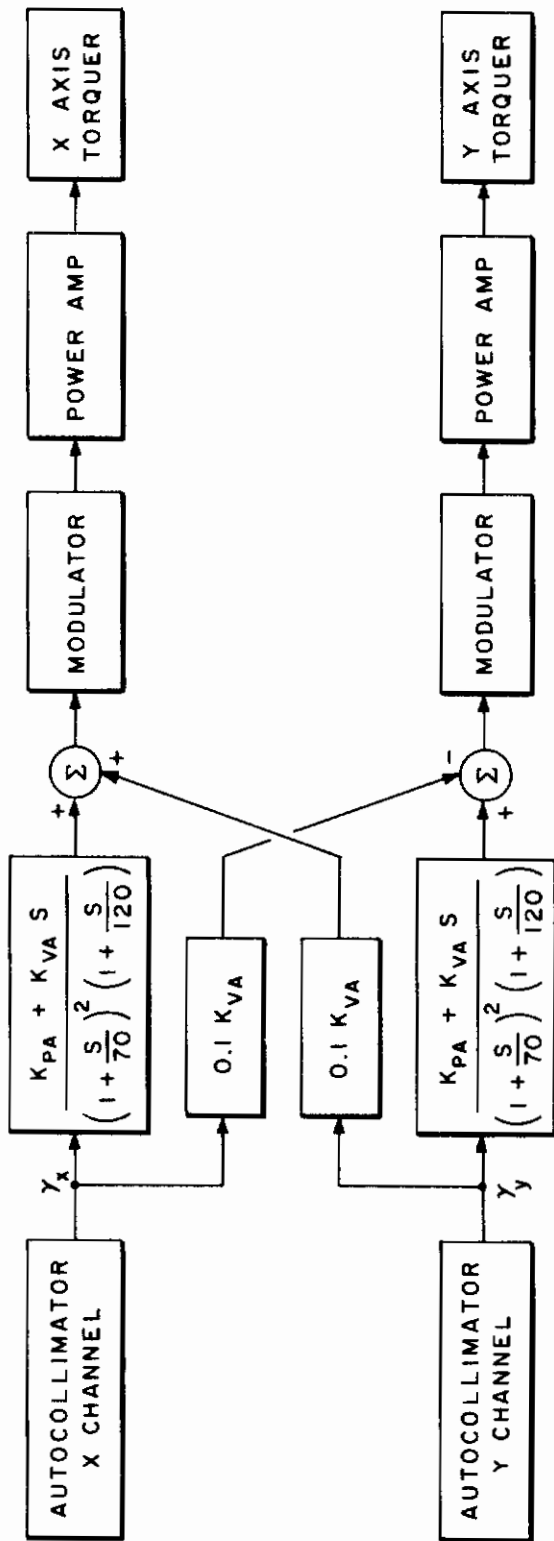
$$K_{PA} = 14.5 \times 10^8 \text{ (dyne cm) / rad}$$

$$K_{VA} = 10.4 \times 10^8 \text{ (dyne cm) / (rad/sec)}$$

MAXIMUM AVAILABLE TORQUE 9.45×10^4 dyne cm

MODE 3

Fig. 25. FINE ERECTION LOOP.



$$K_{PA} = 14.5 \times 10^8 \text{ (dyne cm) / rad}$$

$$K_{VA} = 10.4 \times 10^8 \text{ (dyne cm) / (rad/sec)}$$

MAXIMUM AVAILABLE TORQUE 17.85×10^4 dyne cm

MODES : 4, 5

Fig. 26. FINE CONTROL LOOP.

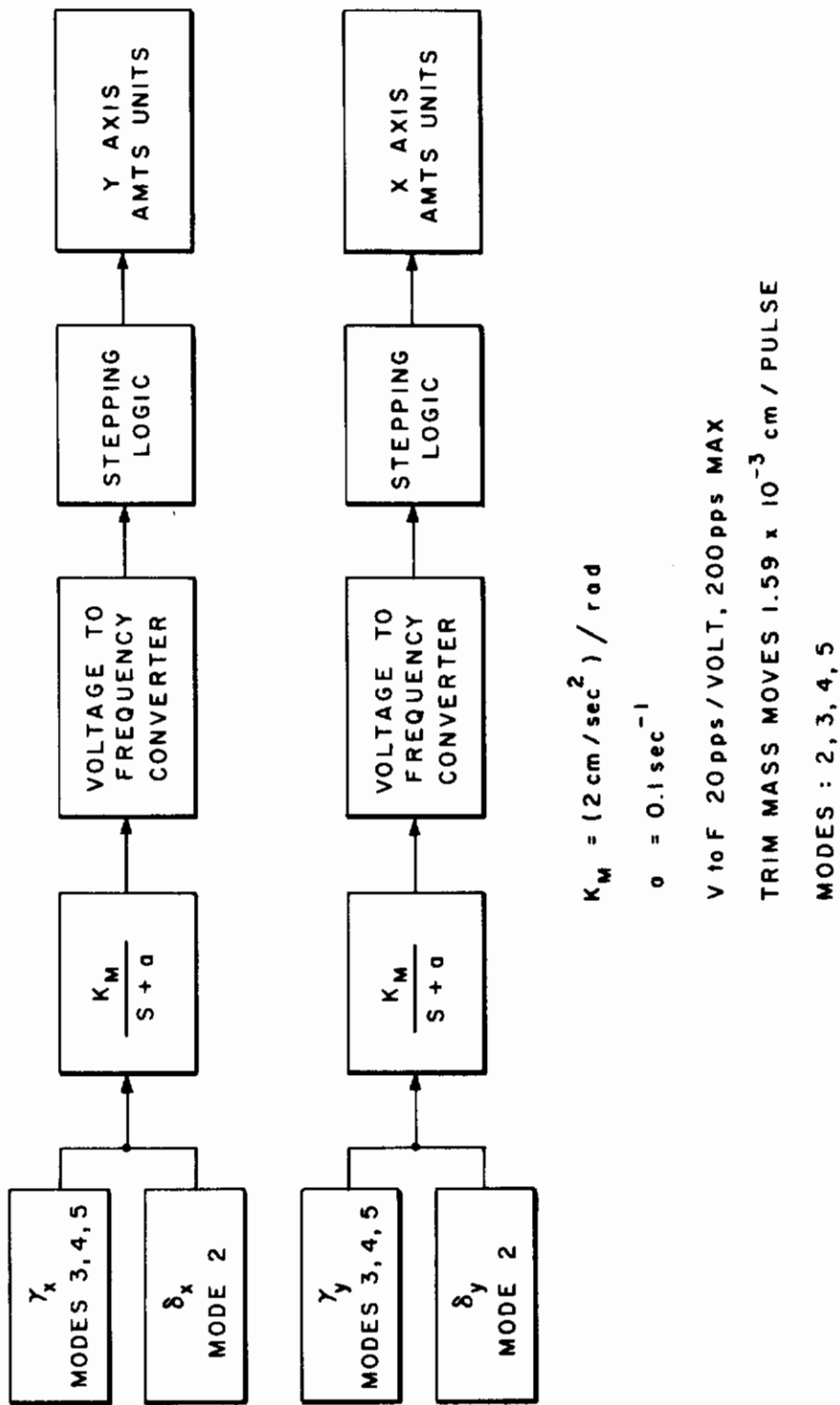
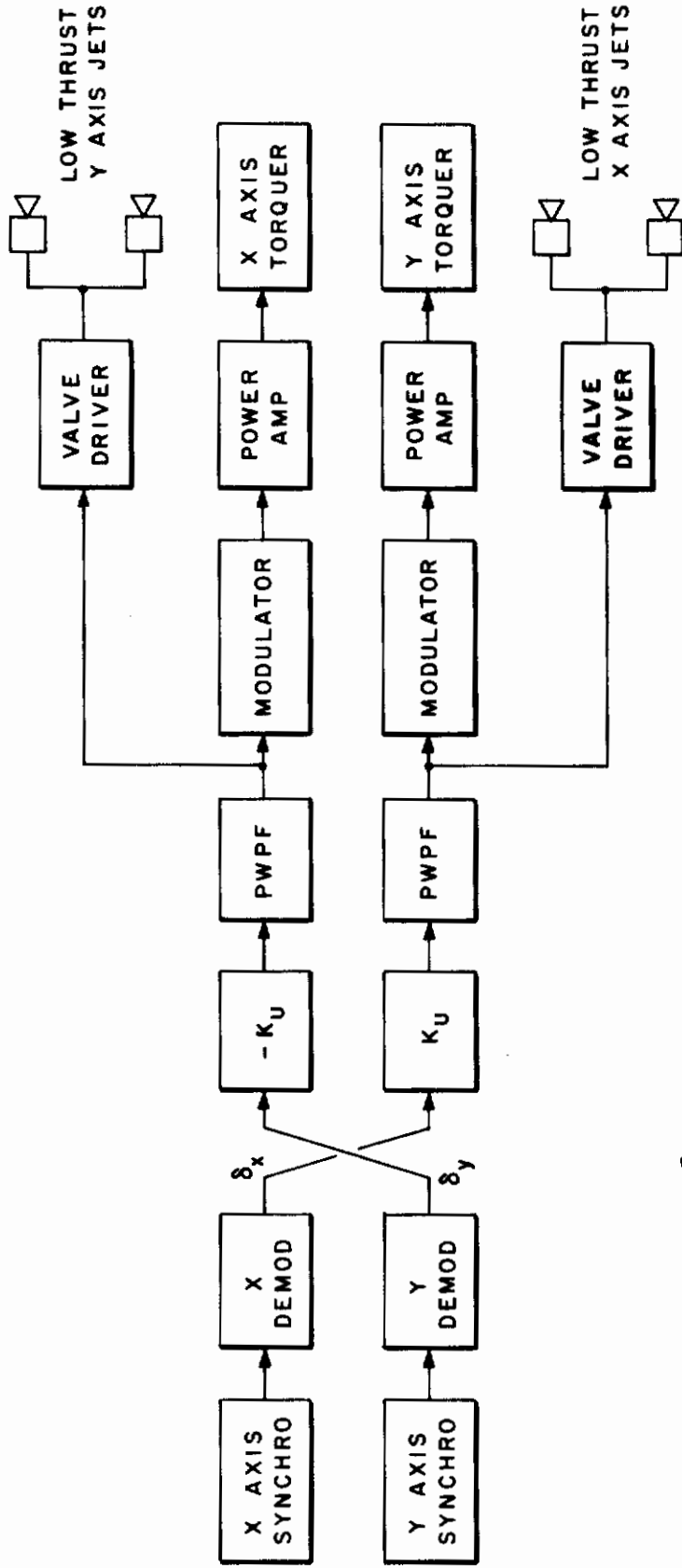


FIG. 27. AUTOMATIC MASS TRIM SYSTEM CONTROL LOOP.



$K_U = 4.28 \times 10^7 \text{ (dyne cm) / rad}$

MAXIMUM AVAILABLE TORQUE $9.45 \times 10^4 \text{ dyne cm}$

MODE 5

Fig. 28. GYRO UNLOAD LOOP.

gyro is made to point at the mirror. In modes 1 and 2, when the autocollimator is not within range of the mirror, the demodulated synchro output provides attitude information.

The gyro drift characteristics (≈ 10 arc seconds/sec free drift at 25°C) is small enough for an attitude reference because the vehicle erects in less than 200 sec; however, bearing-friction effects, as shown in Eqs. (2.27), add an additional drift. If the vehicle initial conditions are below 0.1 rad, it has been found experimentally that attitude reference will not be lost. If the simulator takes longer than 200 sec to damp initial conditions or large attitude excursions occur causing increased bearing drag, autocollimator acquisition is not certain (see Chapter II.B).

2. Control Torquing

Located on the opposite side of each gimbal from the synchro is a two-phase induction motor torquer. Two inputs per torquer are required; one is fixed at 57.5 Vac and the other is variable. Control signals, amplitude modulated at 400 Hz, are sent to power amplifiers whose 0 to 115 Vac variable output drives the torquers which, like the synchros, are aligned parallel to the control axes.

Wheel angular momentum is 8.5×10^6 gm-cm²/sec. Maximum control effort against an inertial torque will cause the gimbals to exceed the mode 4 unload threshold in 5 sec. The disturbance torque environment in the laboratory is such that unloading is required only every 150 to 200 sec.

During precision control in mode 4, gyro drift is a source of disturbing torque. The combined free drift and that caused by bearing friction applies an effective torque to the simulator of 280 dyne cm. For space-flight applications, this would be a significant number; in the laboratory it accounts for less than 2 percent of the disturbance torque.

Figure 29 is a photograph of the gyro and power amplifiers in the simulator. More detailed specifications can be found in the Appendix.

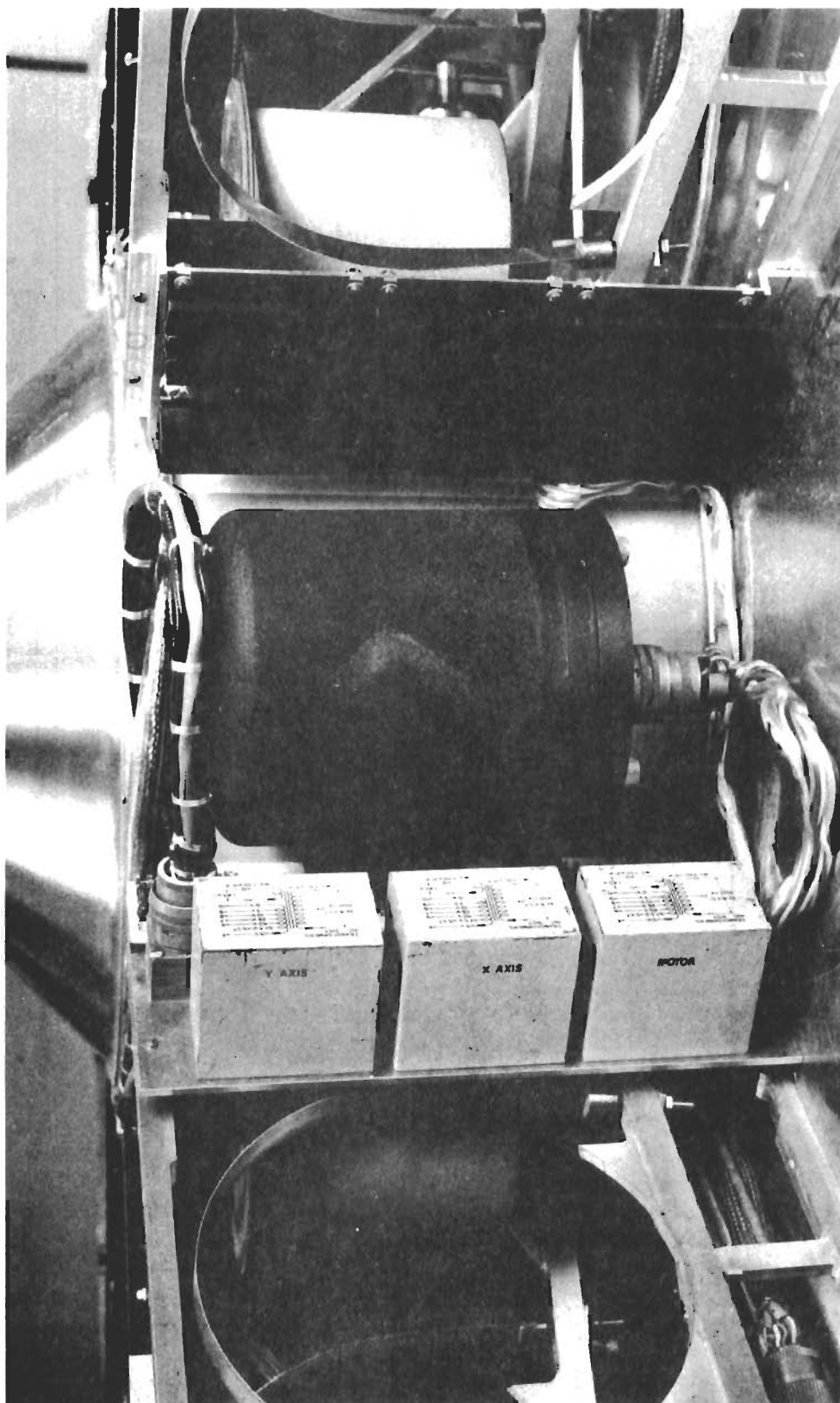


Fig. 29. KEARFOTT T4101 VERTICAL GYRO AND POWER AMPLIFIER.

D. Two-Axis Autocollimator

1. Requirements

In addition to the ability to measure angles precisely, several other features are required of an autocollimator used on a device such as the SVS. They are

- (a) small size and light weight
- (b) low power consumption (less than 5 W)
- (c) moderate (5 Hz) bandwidth
- (d) high dynamic range (5×10^3)
- (e) low noise equivalent angle (less than 0.01 arc seconds in the 5 Hz bandwidth)
- (f) linearity and precision ($\pm 1\%$ to 500 arc seconds; 0.1 arc second desired, 1 arc second acceptable)

Because commercial units meeting these requirements were not available, one was developed by the author (see Fig. 30). The instrument does not have the accuracy ultimately necessary for sub arc second performance; however, given the limitations of the rest of the system, it performs satisfactorily.

2. Optics

The autocollimator operates by sensing the position of a spot of light on a ground-glass surface. As seen in Fig. 31, a light source (6) uniformly illuminates an aperture (9) located at the focal point of the collimating lens (1); thus, the aperture image is focused at infinity (parallel rays). The laboratory reference mirror reflects the parallel-ray beam back through the collimating lens. The refocused image of the aperture passes through the partially silvered mirror (2) and appears on the ground-glass surface of the sensing head (4).

The sensing head is a quadrant of four optically independent light pipes, with a phototransistor attached to the end of each pipe. The light from the image is received by the phototransistors in proportion to the fraction of the image area on the particular light-pipe face.

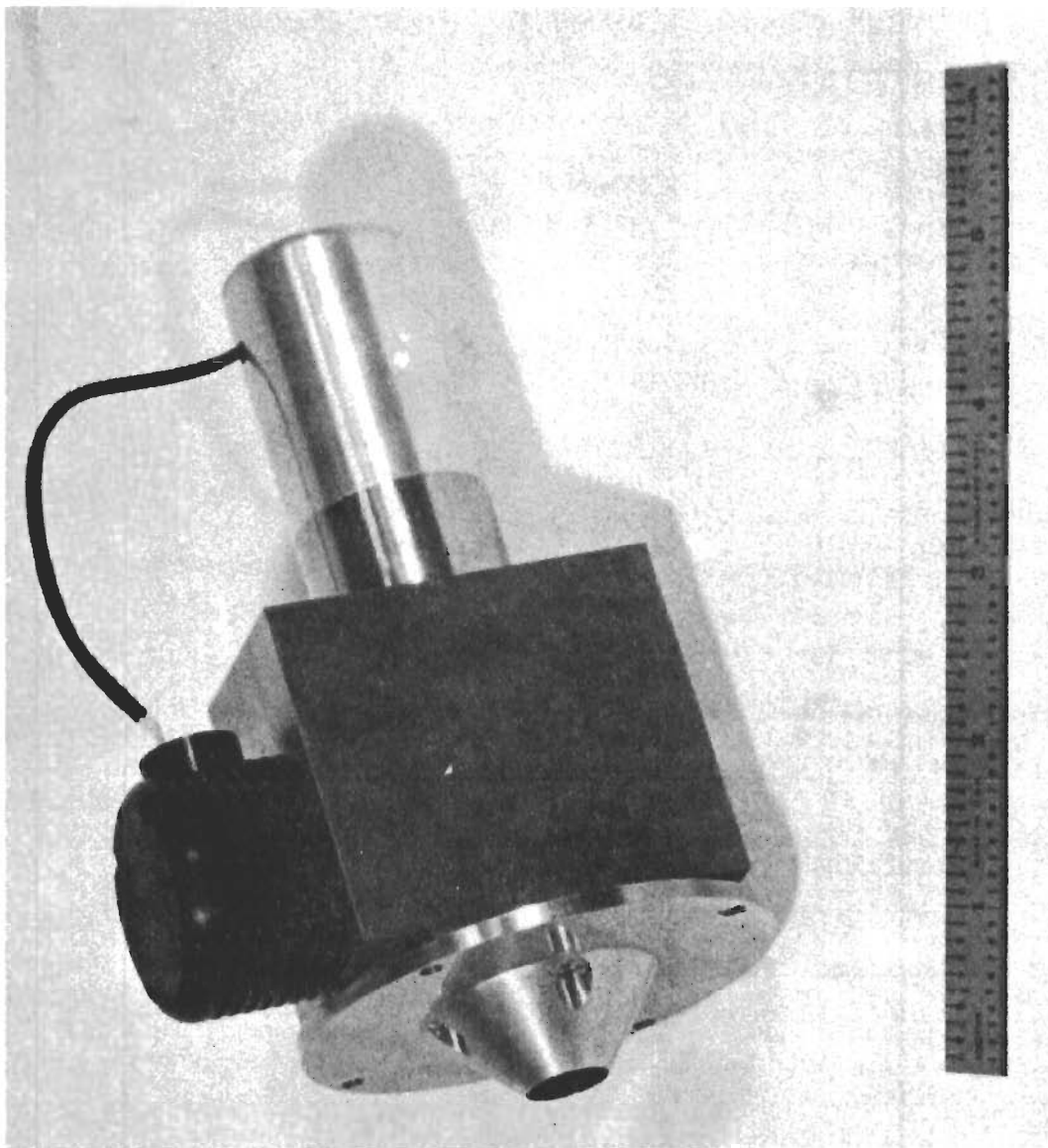


Fig. 30. AUTOCOLLIMATOR USED ON THE SPINNING VEHICLE SIMULATOR.

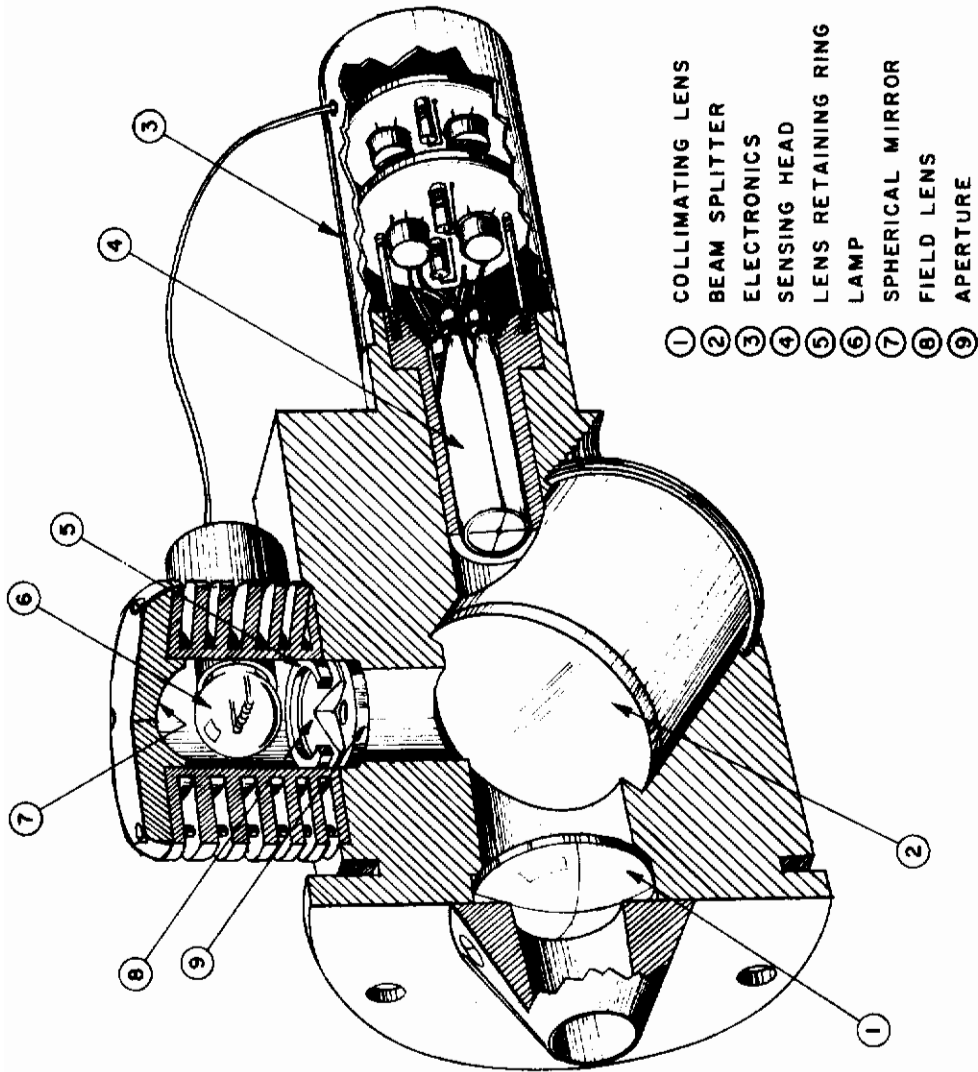


Fig. 31. CROSS SECTION OF AUTOCOLLIMATOR.

If the mirror is not normal to the beam, the image will not be centered on the quadrant and the light distribution will be unequal.

In Fig. 32, the spot is shown on the face of the light pipes. Motion of the autocollimator about a horizontal axis will cause the spot to move vertically; motion about a vertical axis results in horizontal motion.

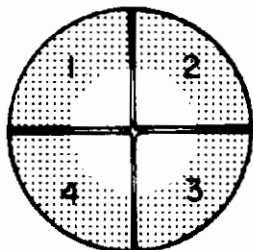


Fig. 32. END-ON VIEW
OF AUTOCOLLIMATOR
SENSING HEAD.

Thus,

$$\gamma_x = K_{ac} (J_1 + J_2 - J_3 - J_4)$$

$$\gamma_y = K_{ac} (J_2 + J_3 - J_1 - J_4)$$

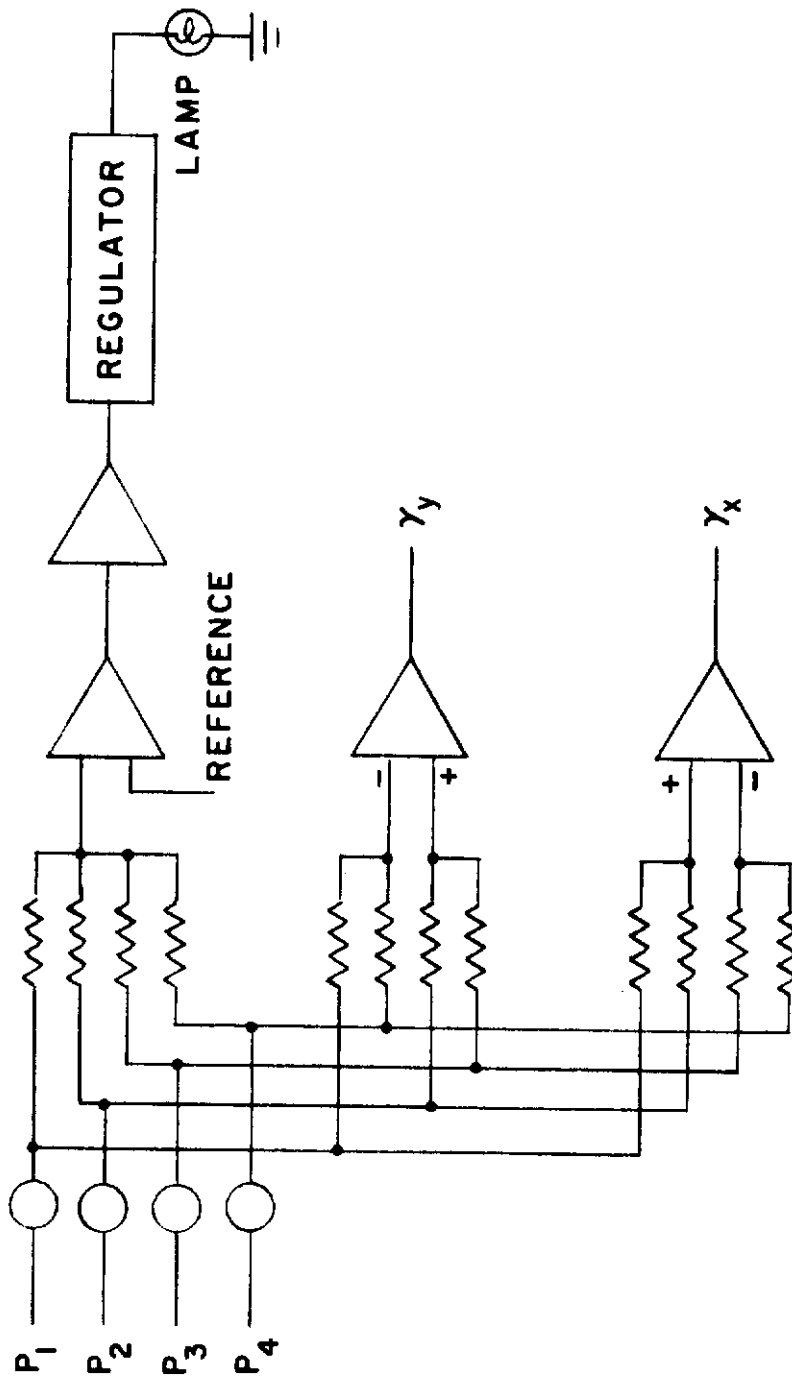
where $J_{1,2,3,4}$ represents the light intensity at each pipe, and K_{ac} is a scale factor which is independent of the distance between the mirror and the autocollimator because the transmitted light rays are parallel.

3. Electronics

The phototransistor signals are preamplified in the autocollimator body (Fig. 31, item (3)). The preamplifier signals necessary to compute γ_x and γ_y are summed in the main electronics rack with operational amplifiers.

An automatic gain control (AGC) is provided for the source lamp. By comparing the sum of the four phototransistor outputs with a reference voltage, the total amount of light falling on the sensing head is held at a constant value. Thus, any degradation of the lamp or change in distance between the mirror and the autocollimator will not affect K_{ac} . Figure 33 is a schematic of the electronics.

A noise equivalent angle of ± 0.75 arc second at 5 Hz bandwidth was attained. Resolution is 1 arc second, with 1 percent linearity to 500 arc seconds and 2-1/2 percent to 1000 arc seconds. The scale factor is 10 mV/arc second.



SCALE FACTOR 10 mV / (ARC SECOND)
P_{1,2,3,4} = PHOTOTRANSISTOR PREAMP OUTPUTS

Fig. 33. BLOCK DIAGRAM OF AUTOCOLLIMATOR ELECTRONICS.

E. Gas-Jet System

The nonconservative property of gas-jet control usually eliminates it from a long-term orbital mission. Particularly for a spinning vehicle, in which a body-fixed moment would cause continuous thrusting, gas jets may be impractical. The Spinning Vehicle Simulator does use gas jets, however, as a secondary part of the control system in the following applications.

- (1) A high-thrust jet is used to damp initial conditions (modes 1 and 2).
- (2) Four low-thrust jets supply torque to remove stored angular momentum from the CMG in mode 5. The thrust of the jets and gyro torques are matched.
- (3) Jets used for CMG unloading also provide control torque in mode 3 when the attitude error is too large to use the gyro torquers.
- (4) A constant spin speed is maintained by a gas jet thrusting tangentially to the simulator circumference.

The working gas is nitrogen stored in four tanks inside the simulator (Fig. 21, item (5)) at 100 atm. A pressure regulator (item (10)) reduces the pressure to 3.3 atm, and the gas is distributed to the six jets.

The five control jets (item (7), four low-thrust, one high-thrust) are located on the ends of the control axes. Thrusting is controlled by electrically operated valves which are either closed or fully open. Intermediate values of thrust are obtained by pulse-width/pulse-frequency modulation. This technique provides an average thrust that is linearly proportional to the control signal. In mode 5 operation (Fig. 28), the valve modulators drive both the valves and the gyro torquers and, as a result, the nonlinear thrust characteristic is compensated for, making the approximation to linear control unnecessary.

When the regulator is pressurized, the spin maintenance jet operates continuously. A needle valve is used to adjust the thrust.

A description of the PVPF modulator, control valves, and jet specifications can be found in the Appendix.

F. Automatic Mass Trim System

1. Mechanical Components

The AMTS consists of two identical pairs of movable masses; the members of each pair are located at opposite ends of the control (intermediate moment of inertia) axes. The masses move vertically, and their line of motion is parallel to the vehicle symmetry (nominal spin) axis.

Each AMTS unit contains the following components (numbers refer to Fig. 21):

- (a) 2.72 kg mass, movable through ± 10 cm (9)
- (b) 0.125 pitch lead screw which moves the mass as it turns
- (c) 200 step/revolution drive motor (8) coupled by gears to the lead screw
- (d) lightweight housing (6) which holds motor, gears, lead screw and bearings and is attached to the simulator frame
- (e) electrical connector to interface unit with electronics rack
- (f) attitude control valve and jet (7)[†]

2. Electronics

The electronic portion of the AMTS has four sections.

- (a) Sensor: either the gyro synchros (mode 2) or the auto-collimator (modes 3,4,5) provide error signals.
- (b) Filter: the sensor input is filtered to obtain the zero-frequency component of the error signal.
- (c) Voltage-to-Frequency Converter: drive motors are of the stepping variety. Analog signals must be converted to constant-voltage pulses.

[†] Although the gas jets are not part of the AMTS, the housing is a convenient mounting location to place them on the control-axis centerline. Valve electrical connections are made through the AMTS connector.

- (d) Stepping Logic: motor coils are pulsed in sequence, 4 pulses/step. V-to-F output is converted into the correct pulse train.

All the electronics for the AMTS are located in the main electronics rack.

3. Operation

The AMTS is utilized in two ways: first, as a means to manually trim the location of the vehicle center of mass along the Z_B -axis and second, to automatically trim body-fixed moments, products of inertia, and sensor-vehicle misalignments.

The first function is performed before each experimental run, as discussed in Section A. The masses move in common mode and are adjusted to minimize the center-of-support/center-of-mass separation by maximizing the period of pendulous oscillation (the vehicle is not spinning).

During automatic operation, the masses in a mass pair move only differentially. As seen in Figs. 13 and 20, there is minimal AMTS activity once initial conditions have been corrected, unless a large disturbance is encountered.

The system used on the SVS has the following performance characteristics:

maximum trim moment	2.72×10^6 dyne cm
minimum incremental moment	424 dyne cm
maximum angular deflection of maximum axis of inertia	0.028 rad/axis
minimum incremental deflection	0.84 arc seconds

G. Electronic Subsystem

Electronics for the SVS are divided into four sections:

Contrails

- (1) main electronics rack containing circuitry necessary to mechanize the control loops (Section B and Figs. 25 to 29), battery, and control panel
- (2) gyro power amplifiers (Section C) used to drive gyro motor and torquers
- (3) external control box and power supply
- (4) telemetry system consisting of V-to-F converters and an AM transmitter located on-board the vehicle and five AM radios and F-to-V converters mounted on the air-bearing pedestal

1. Main Electronics Rack

The main electronics rack (Fig. 34) contains thirteen 4-1/2 x 6-1/2 in. removable circuit cards. Additional components (such as heat-sunk power transistors and an enclosed dc-to-dc converter) also are included. The rack is fully removable from the simulator by means of five cable connectors and two wing-nuts.

The following is a brief description of the function of each of the cards.

<u>Card Number</u>	<u>Function</u>
1	±12 V regulator and battery undervoltage protection
2,3	four V-to-F converters and stepping logic circuits (two each/card) for AMTS motors
4	three PWPF (one for each low-thrust pair and one for the single high-thrust) and five valve drivers
5	two 400 Hz AM modulators for gyro torquers
6	precision frequency base used to obtain 400 Hz for modulators and demodulators; time-delay circuits also use the frequency base
7	mode-sequencing logic
8	interface circuitry to match analog inputs to digital logic on card 7
9	V-to-F converters for telemetry

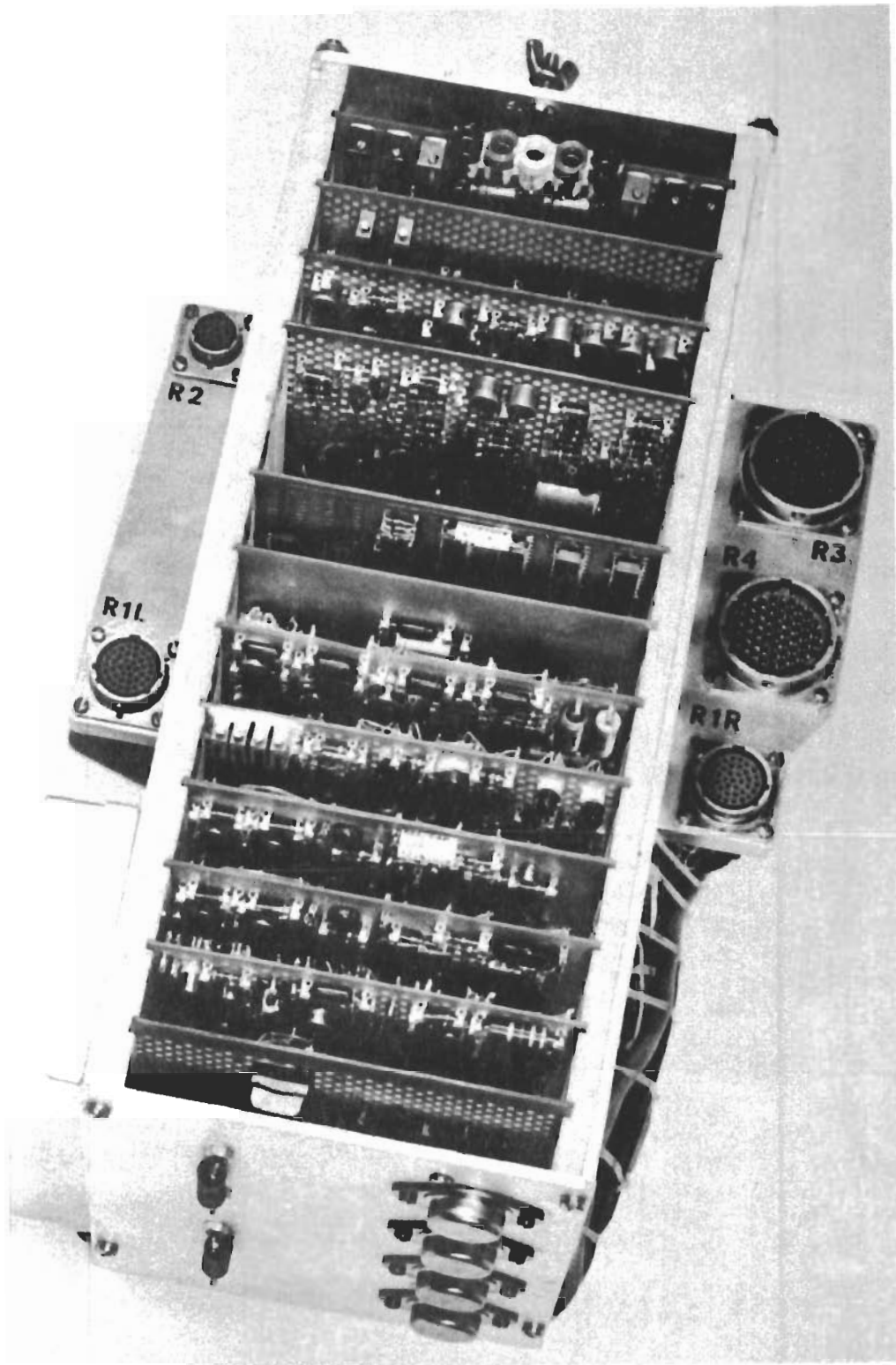


FIG. 34. MAIN ELECTRONICS RACK.

Contrails

<u>Card Number</u>	<u>Function</u>
10	spare
11	AMTS filters
12	two 400 Hz synchronous demodulators for reading gimbal angles
13	autocollimator summing electronics, lamp automatic gain control, and lead-lag compensation

2. Power Supplies

During operation, the simulator is powered by two 17 V NiCad batteries. Each battery consists of 28 size "F" cells, two sets of 14 cells in parallel. The nominal capacity is 14 A-hr which is enough for 70 to 80 min. The batteries are protected by a 10 A fuse and an under-voltage relay. If the voltage on either battery drops below 1 V/cell, the system automatically shuts itself off.

Regulated power supplies on card 1 provide ± 12 V used for the operational amplifiers in the system. A dc-to-dc converter, added for efficient utilization of available battery energy, supplies 5 V for integrated logic circuits and -8 V for the autocollimator AGC.

For gyro spin-up and autocollimator alignment in mode 0, an external power supply is used. Switched through the external control box, it supplies ± 18 V at 10 A (maximum).

3. External Equipment

Electronics external to the simulator include the external control box, telemetry receivers, and F-to-V converters. The control box monitors the gyro, autocollimator, AMTS, and power supplies while the vehicle is in mode 0 (Section B.3). It also contains a battery charger for the NiCad batteries.

The external telemetry equipment is located just below the vehicle underside, on the pedestal (Fig. 23, item (5)). The telemetered signals, frequency and amplitude modulated on the vehicle, are received by the five commercial broadcast band AM receivers and converted to their original form by the F-to-V converters. A power supply is also included.

Contrails

Additional details of the controller circuitry, vehicle and external control stations, and telemetry are presented in the Appendix.

Chapter V

EXPERIMENTAL RESULTS

Section A presents the results of laboratory testing of the Spinning Vehicle Simulator. Operation with and without automatic mass trimming demonstrates the necessity of this feature. Sources of noise and disturbing torques that limit performance are discussed in Sections B and C, respectively. An analog simulation of vehicle dynamics connected to the simulator control electronics is employed to analyze electronic noise. Extrapolating the results of the first three sections, satellite performance in the orbital environment is predicted in Section D.

A. SVS Performance in the Laboratory Environment

1. Normal Operation

Figure 35 displays telemetry output for the simulator operating in all five modes. AMTS operation in modes 2, 3, and 4 is clearly visible as the zero-frequency offset error is reduced. A slight increase in attitude error caused by a mismatch between the thrust of the unload jets and the gyro torque is seen during mode 5. Although the inertial disturbing torque is somewhat larger than usual ($\approx 1.76 \times 10^4$ dyne cm in this example, normally ≈ 0.8 to 1.0×10^4 dyne cm), only three spin periods are required to unload the gyro.

Mode 4 output on an expanded time scale is shown in Fig. 36. The sinusoidal oscillation at spin frequency can be detected in the otherwise random noise of the signal. The γ_y trace indicates a 2 arc second offset from null, caused by a combination of two factors.

- (a) Bias in the AMTS V-to-F converters: a finite autocollimator signal (in this case ≤ 2 arc seconds) is required to offset the bias.
- (b) Telemetry bias: the relatively simple design of the telemetry F-to-V converters makes null stability somewhat less than desired. Although the telemetry is zeroed just prior to a data run, drift (here less than 500 mV) over a period of 30 to 40 min does occur.

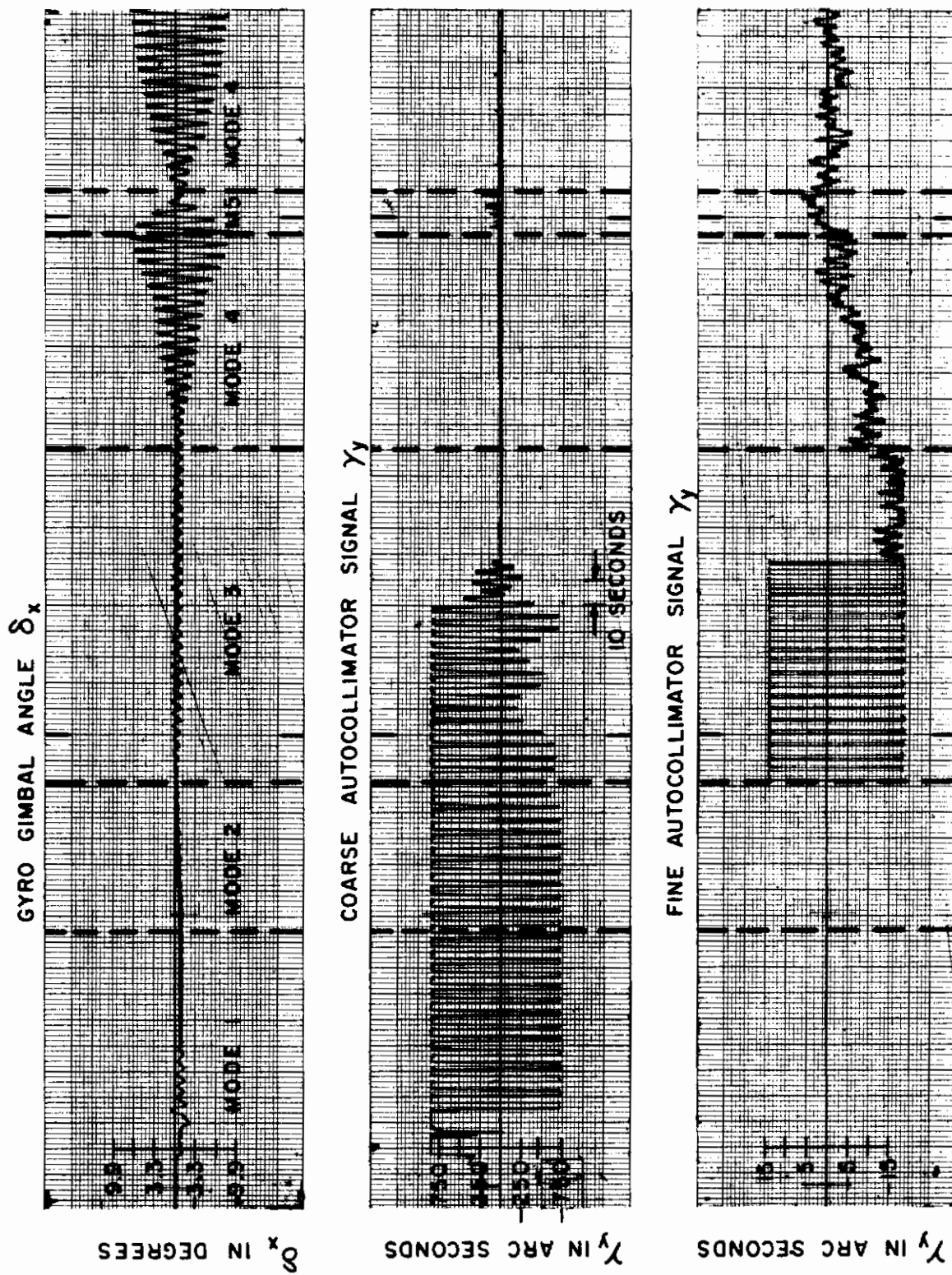


Fig. 35. TELEMETRY OUTPUT DURING TYPICAL SVS OPERATION.

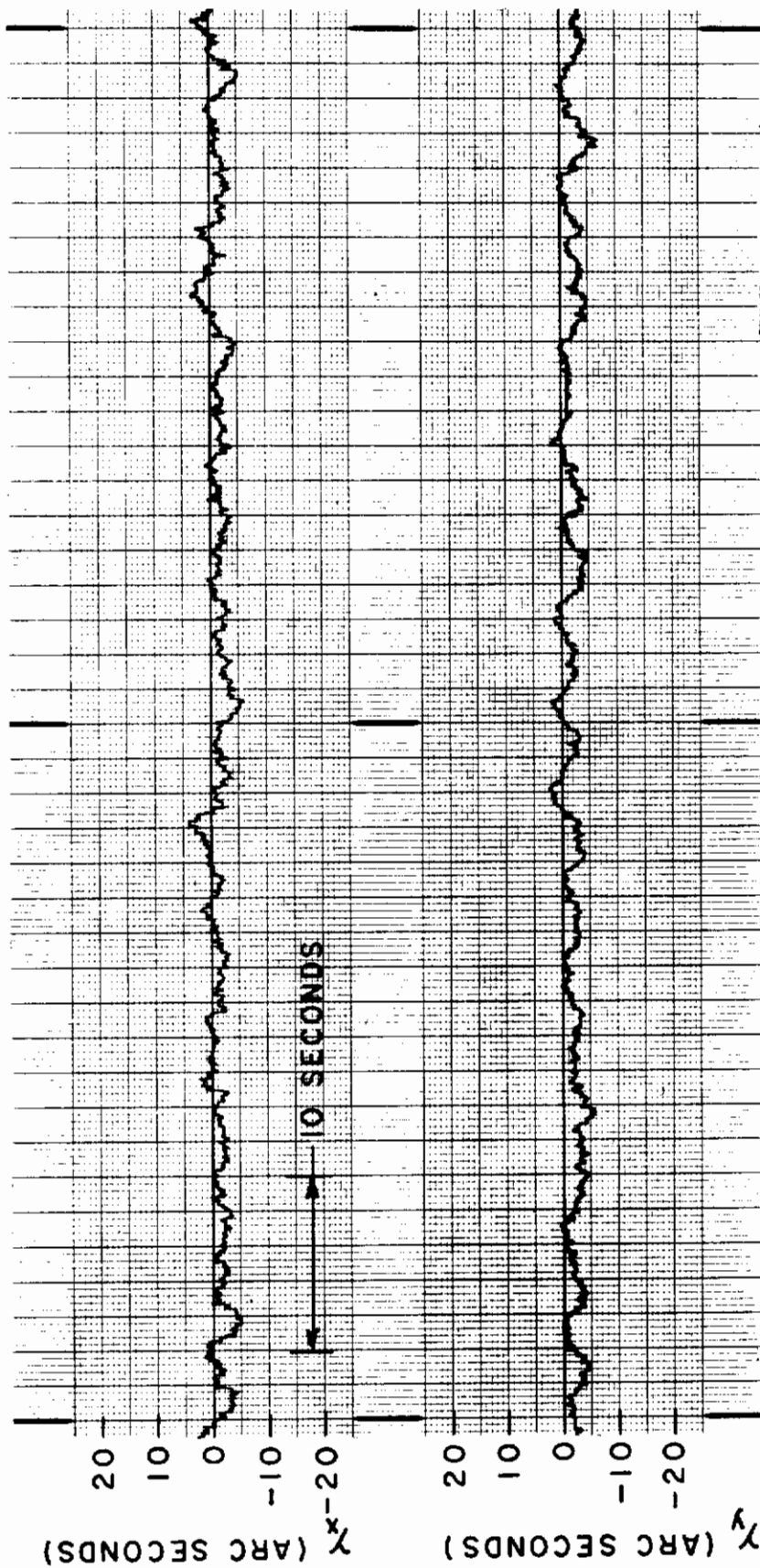


Fig. 36. TELEMETERED AUTOCOLLIMATOR OUTPUT DURING SVS MODE-4 OPERATION.

2. Operation without Automatic Mass Trimming

The utility of automatic mass-trim capability is illustrated in Fig. 37. After the AMTS is turned off, a drift of 3 arc seconds/min can be observed. This effect is caused by the mass of the vehicle changing as nitrogen is used by the spin and unload jets. Quantitatively, the cause could be either (1) a 3.6×10^{-4} cm/sec shift in the body X-Y plane of the center of mass relative to the center of support, or (2) a 0.72 arc second/sec motion of the maximum axis of inertia away from the autocollimator null axis. Autocollimator drift is ruled out because null stability has been independently measured at 0.1 arc seconds/hr.

The probable cause is a misalignment in the X-Y plane of a line between the centers of mass of nitrogen in two opposing tanks and the corresponding intermediate axis of inertia. If the center-to-center line is parallel to the axis but offset by as little as 0.8 cm, the gas-expulsion rate of 0.125 gm/sec/tank will produce a moment large enough to cause the observed drift. Other sources of moments resulting from tank misalignments (either vertically or radially) produce drifts too small to be seen.

The above discussion illustrates the necessity of automatic mass trimming when the vehicle mass is changing. A flight vehicle using thrusters to unload a CMG would be subject to a similar effect but reduced by one to two orders of magnitude (because of less frequent unloading and better tank geometry). Some type of trim system, possibly one in which the sensor is gimballed to eliminate the need for trim masses (see Chapter VI.B), would be required.

3. Conclusions

Experimental evidence indicates that the analytical and design techniques discussed in Chapters II and III are valid and resulted in

- (a) precision attitude control with an average error of 2.5 arc seconds in the laboratory environment
- (b) verification of the automatic mass-trim concept and its necessity for precision attitude control in the laboratory

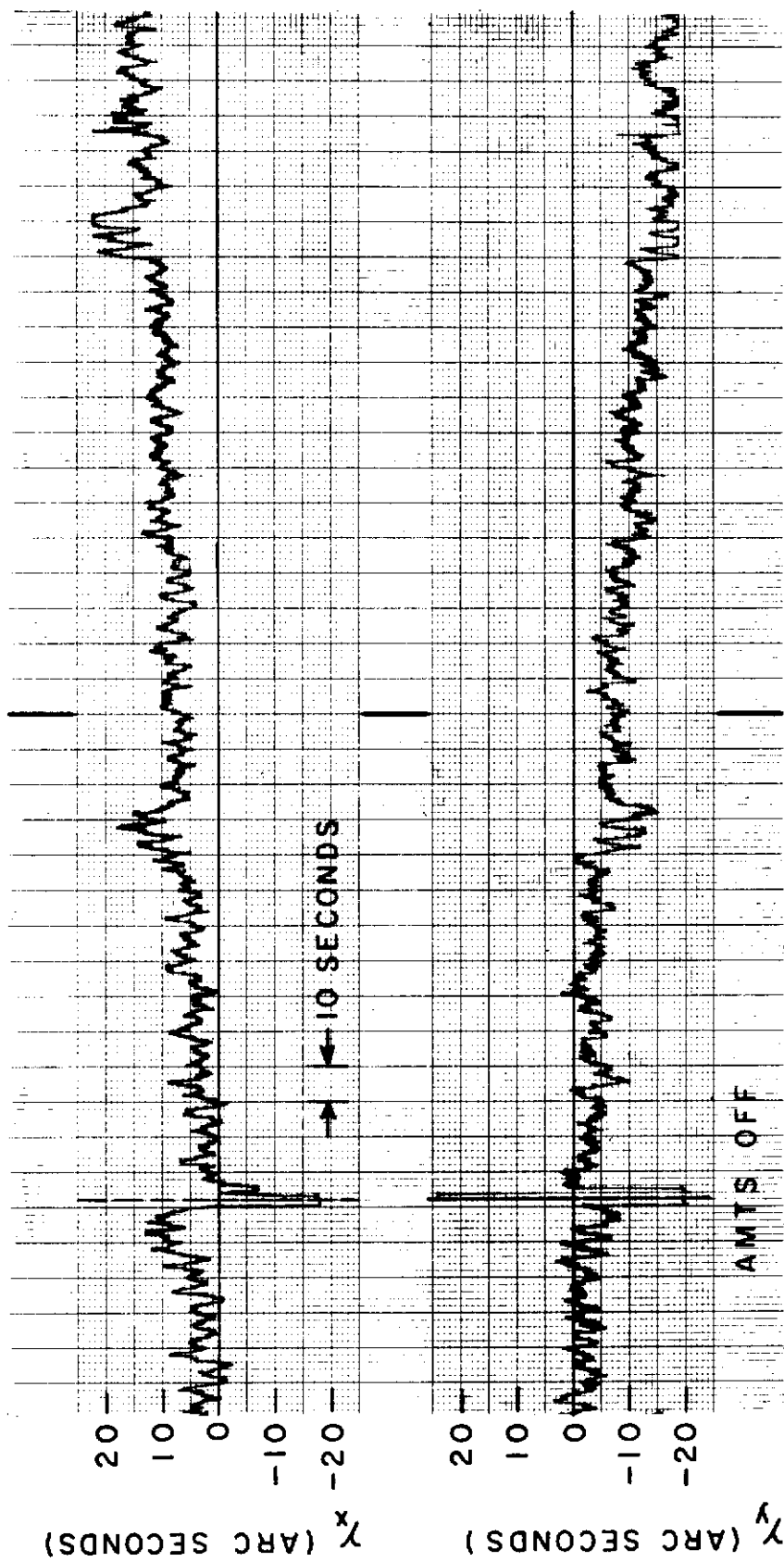


FIG. 37. TELEMETERED AUTOCOLLIMATOR OUTPUT DURING SVS MODE-4 OPERATION; AMTS OFF.

- (c) practical demonstration of a multimode controller, with a large dynamic range in the error signal, whose performance is only slightly degraded during CMG momentum dumping

B. Electronic Noise

1. Autocollimator Noise

A fundamental limitation on control-system precision is the noise equivalent angle of the sensor. Figure 39 is a sample of autocollimator output and indicates this angle to be ± 0.75 arc seconds for a 5 Hz bandwidth. Figure 38 displays the power spectrum of the autocollimator signal, made by tape recording the output on an FM-to-FM recorder and using a Sigma V computer to process the data. The spectrum is relatively flat in the region between 0.1 and 1.0 Hz. Because the control system (as noted in Chapter III.A) is sensitive to disturbances at spin frequency, noise power near β is a potential error source. Although some increase is observed near β , the additional energy is not significant.

2. Combined Electronics and Autocollimator Noise

The combined effect of the electronic system and sensor noise was measured, using a hybrid simulation. A small analog computer, programmed with vehicle and trim-system dynamics, was connected to the electronics package, as shown in Fig. 41. Because the only source of driving noise was that provided by the autocollimator and electronics, the effects of laboratory disturbing moments (Section C) were eliminated. The measured attitude error (Fig. 40) was ± 1 arc second.

3. Conclusions

Based on data presented in Figs. 39 and 40, noise generated by the autocollimator and the electronics was not a limiting factor in the laboratory performance when compared to environmental disturbances. If these disturbing moments could be reduced to the level of the orbital environment (Section D), the noise equivalent angle of the autocollimator

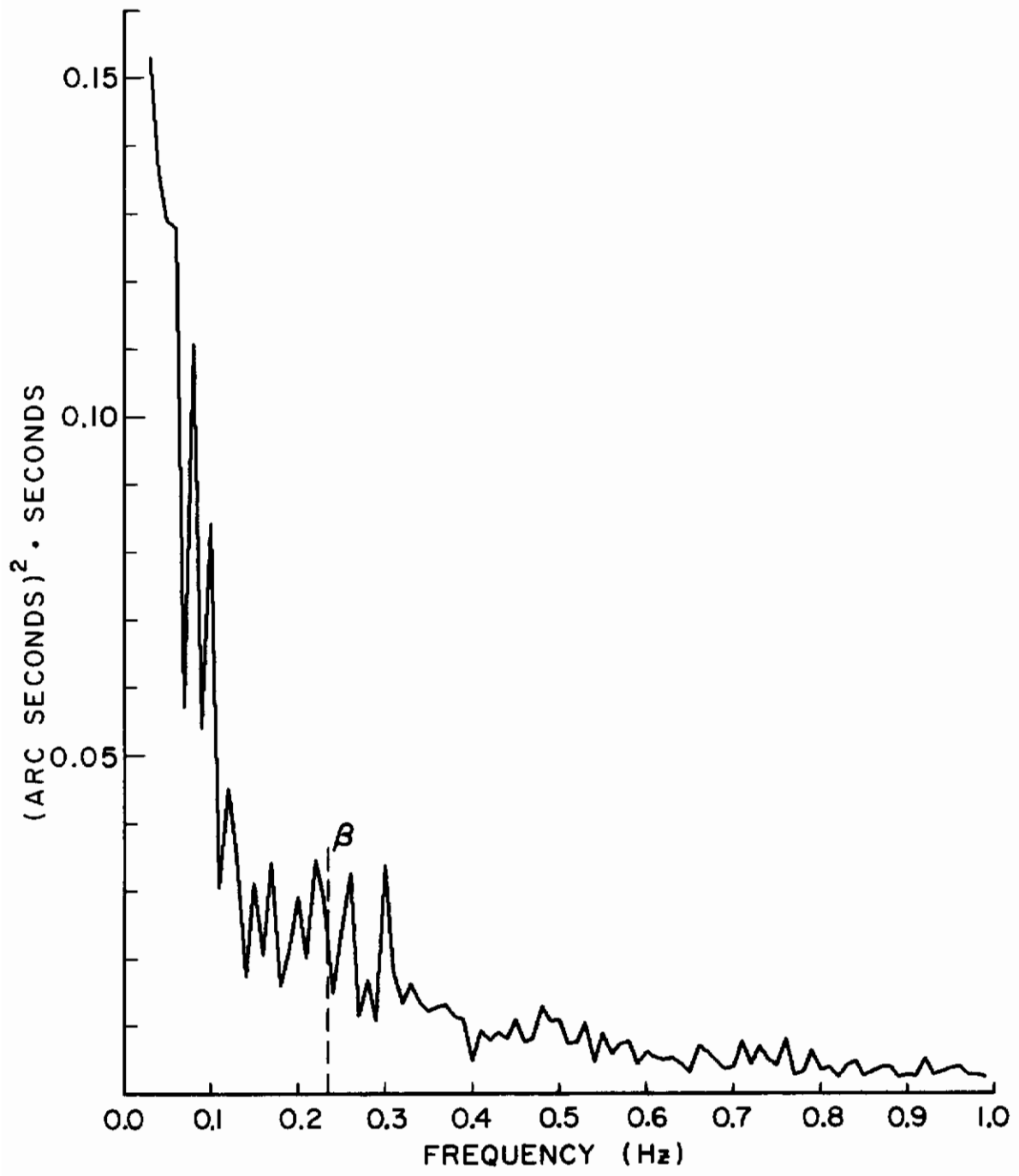


Fig. 38. POWER SPECTRUM OF AUTOCOLLIMATOR SIGNAL.

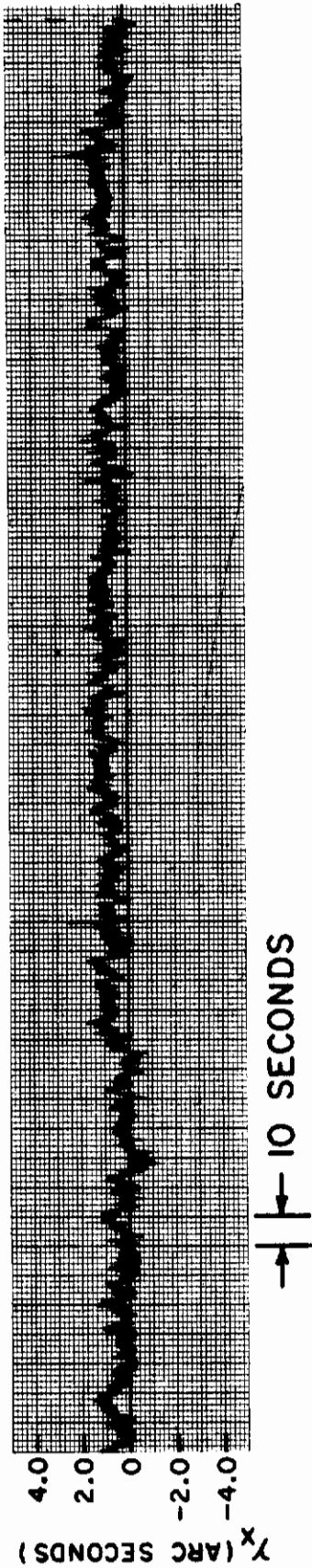


Fig. 39. AUTOCOLLIMATOR NOISE EQUIVALENT ANGLE.

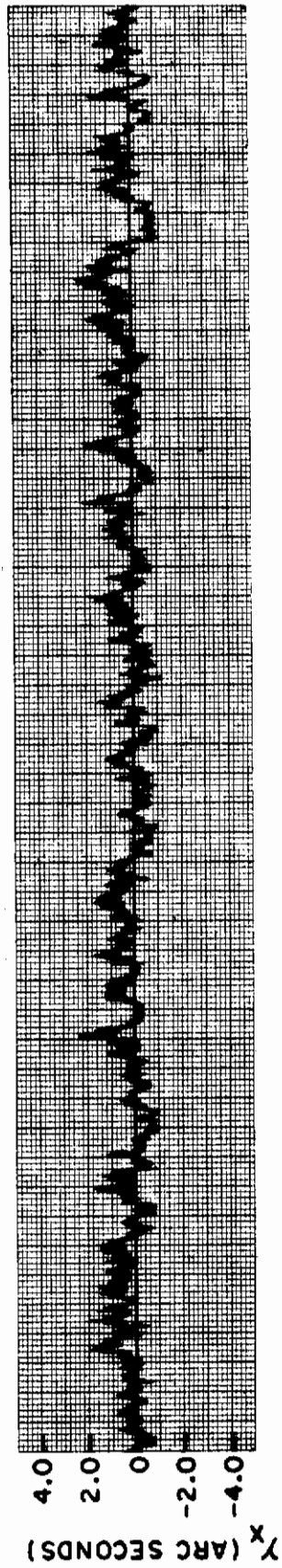


Fig. 40. ATTITUDE ERROR SIGNAL, NO ENVIRONMENTAL DISTURBANCES.

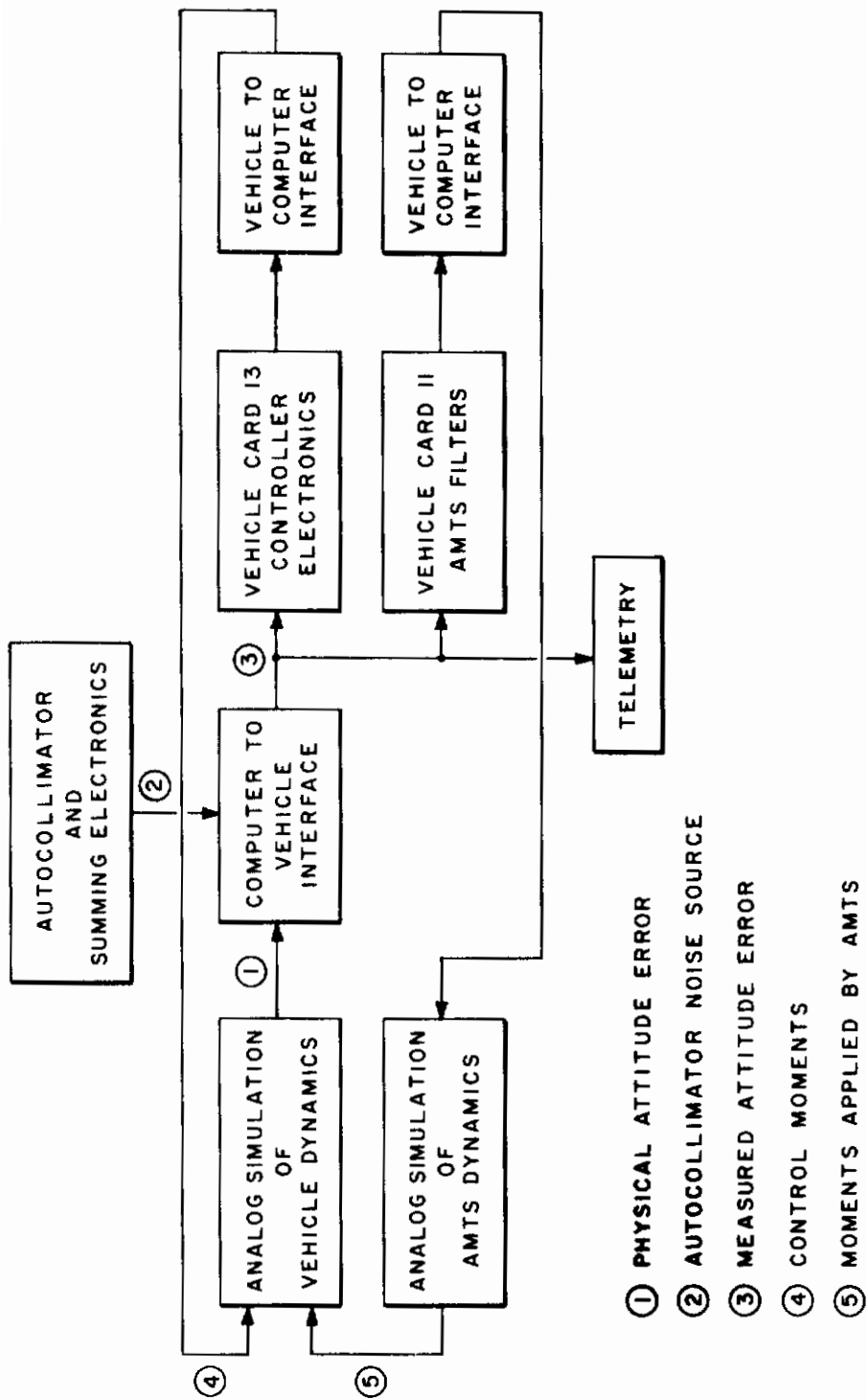


Fig. 41. HYBRID SIMULATION.

would become the lower bound on pointing accuracy. The control electronics appear to have only 30 to 40 percent of the noise equivalent angle of the sensor and thus would not limit performance.

C. Environmental Disturbances

1. Sources of Disturbing Moments

Four basic sources of disturbing moments are associated with laboratory testing of a satellite simulator. In order of importance, they are

- (a) gravitational torques
- (b) an apparent torque due to earth rate
- (c) air-bearing turbine torques
- (d) air currents in the laboratory

Minimization of gravity torques caused by center-of-mass/center-of-support separation was discussed in Chapter IV.A and F. The problem is twofold: locating the center of mass as close as possible to the center of support and leveling the reference mirror to the local horizontal. Using the present apparatus, the precision with which these two parameters can be adjusted is less than desired. The mirror can be adjusted by micrometers and a bubble level to within 0.01 rad of horizontal. By allowing the nonspinning simulator to oscillate pendulously and maximizing the period with common-mode trim-mass adjustments, the mass center can be located to within 0.08 mm of the center of support. For most applications, a 0.08 mm uncertainty in the mass-center position is adequate; however, in the case of the SVS, it becomes a major source of disturbing torque.

An automatic system added to the existing AMTS could eliminate the major portion of this disturbance. If the simulator is operated in a nonvertical orientation and if the trim masses are driven in common mode proportional to the magnitude of the spin-frequency component of error signal, a torque to compensate for gravitational disturbing

moments would be produced. Synchronous demodulation of γ and modification of AMTS drive circuits would be necessary.

Air-bearing turbine torques resulting from surface irregularities and bearing-cup tilt and an apparent torque caused by earth rate, produce similar inseparable effects in a spinning vehicle simulator. Their magnitude and direction can be estimated by observing vehicle spin-axis drift with no control torquing. Adjustment of the bearing tilt angle to minimize the drift corrects for both effects simultaneously; in addition, the automatic system described above would compensate for the residual of these torques.

Moments caused by air currents in the laboratory and vehicle-induced turbulence are difficult to measure. Qualitatively, they appear to affect the error signal randomly rather than solely at spin frequency. The addition of a housing around the simulator produced a small but perceivable improvement in control precision. Prior to its construction, activity of the experimenter near the simulator caused noticeable attitude disturbance.

2. Conclusions

Operation of the SVS in the absence of environmental disturbances was simulated, as discussed in Section B. By comparing a power spectrum made during an experimental run to one made from the simulation, a measure of the effects of the laboratory environment on control-system performance can be obtained.

Equations (3.11) and Figs. 8, 13, and 20 indicate that torques fixed in the laboratory cause the system to oscillate sinusoidally at spin frequency; thus, a spike at β is predicted in the power spectrum of the simulator affected by laboratory-fixed torques. Figure 42 presents power spectra of the simulator, with (solid line) and without (dashed line) environmental disturbances acting on it. The power in the laboratory spectrum at β is approximately 8 to 1 larger than that in the electronic-and-sensor-noise-only spectrum, indicating the strong influence of the laboratory torques. Because of the somewhat random nature of the disturbances, the averaging effect of the computation procedure used to obtain the spectrum, and the finite width of the controller "Q," the spike is wider than that of a pure sine-wave input.

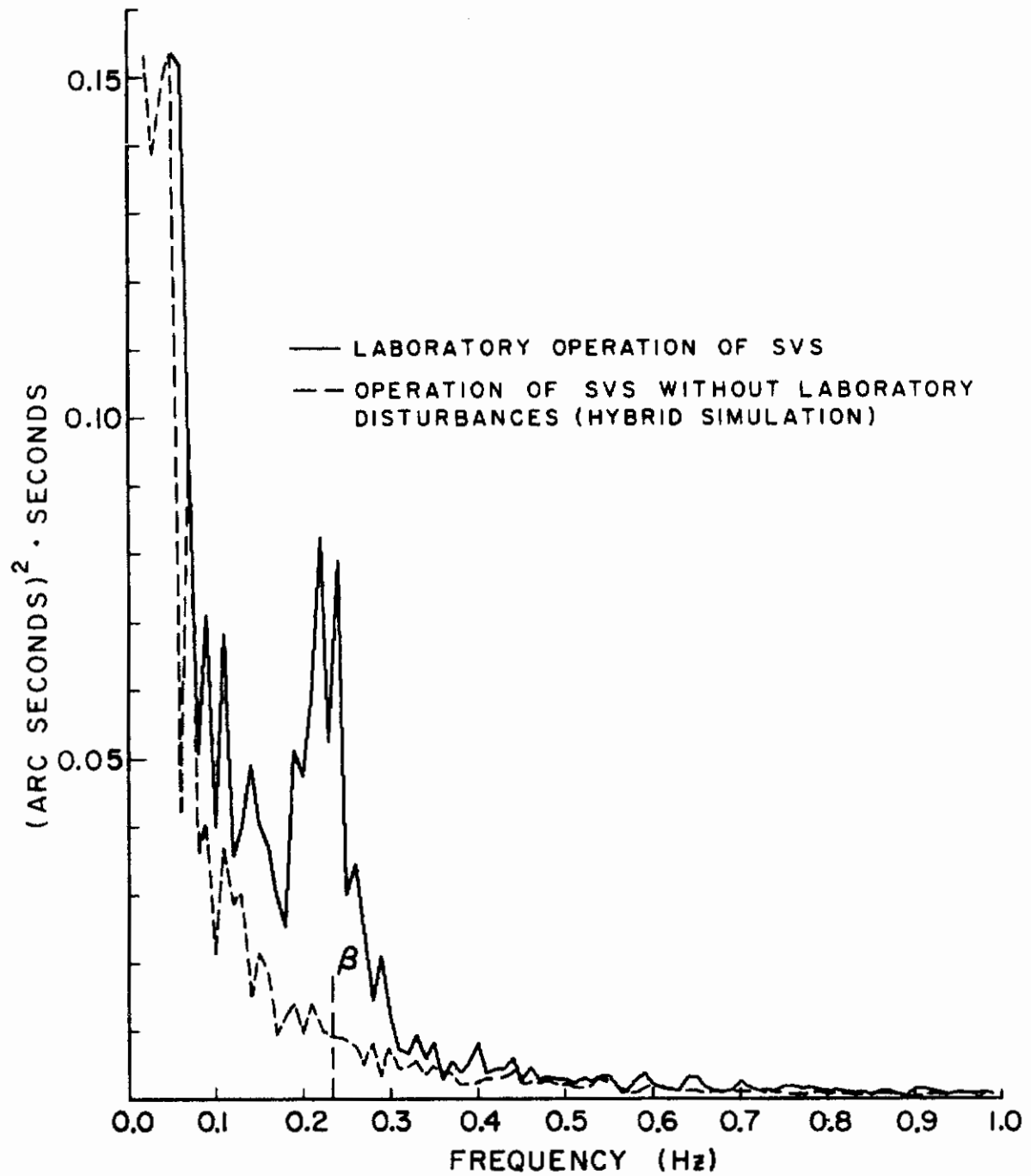


Fig. 42. POWER SPECTRA OF ATTITUDE ERROR SIGNALS.

Based on the comparison in Fig. 42, it can be concluded that the effects of the laboratory environment are the limiting factor in simulator performance. Table 2 lists the disturbance sources, their magnitude, and the resulting attitude error.

Table 2
LABORATORY DISTURBANCE SOURCES

Source	M_{DI} (dyne cm)	Q_{DI}/K_p (arc second)
Gravity Torque	8.70×10^3	1.16
Uncompensated Earth-Rate Torque	1.26×10^4	---
Uncompensated Turbine Torque	$\approx 5 \times 10^3$	---
Compensated Earth-Rate and Turbine Torques [3.34×10^{-5} (rad/sec) drift]	6.23×10^3	0.86
Air Currents and Turbulence (estimated velocities of 5 to 10 cm/sec)	$\approx 1.5 \times 10^3$	0.20

D. Extrapolation of Laboratory Results to Performance in the Orbital Environment

Orbital disturbance torques acting on a hypothetical Unsupported Gyroscope satellite [1,2] in a 700 km polar orbit were calculated by Sorenson [11]. The inertial and geometric properties of the vehicle in Ref. 11 are nearly identical to those of the SVS. Sorenson develops analytical models for the following sources of disturbance torques:

- (1) the atmosphere
- (2) radiation pressure
- (3) misaligned control jets
- (4) gravity gradient
- (5) magnetic effects
- (6) reference-frame kinematics

The maximum combined moment in either axis of the nonspinning orbit coordinates did not exceed 150 dyne cm.

It is assumed that state-of-the-art flight-quality hardware will be used; thus, the following assumptions concerning sensor resolution, gyro performance, and electronic noise equivalent angle will be made.

- (1) The attitude sensor is a high-precision autocollimator tracking a flat located perpendicular to the rotor axis of maximum inertia. It has a resolution of 0.025 arc seconds [2].
- (2) The CMG is of inertial-instrument quality with an $|\vec{H}| = 4 \times 10^7$ gm-cm²/sec. Drift torque applied to the vehicle is <100 dyne cm.
- (3) CMG torquers have $\geq 1.4 \times 10^6$ dyne cm maximum torque. Low-noise electronics allows K_p and K_v to be increased, thereby improving steady-state offsets and AMTS performance. $K_p = 100$ sec⁻¹ and $K_v = 69.4$ sec⁻².
- (4) Combined attitude-sensor and control-system electronics noise equivalent angle is less than 0.04 arc seconds.

Under these assumptions, the total disturbing moment applied to the vehicle is less than 250 dyne cm and the performance is predicted to be

- (1) an attitude error caused by combined disturbance and noise sources of 0.05 arc seconds or less
- (2) duration of mode 4 operation (time between CMG unloadings) of 1.6×10^4 sec
- (3) an estimated 9.25 gm of N₂ to be used per 24 hr period if an N₂ thruster system similar to the one on the SVS is employed to unload the CMG; 14 liters required for a 1 yr mission if the gas is stored at 200 atm

Because 0.1 arc seconds is an acceptable performance for the Unsupported Gyroscope experiment [1], some of the above requirements may be relaxed. Assuming an effect not considered in the analysis of Ref. 11 or assuming that another effect masked in the laboratory by the large disturbing forces is not present, sub-arc-second pointing accuracy can be expected.

Chapter VI

CONCLUSIONS

Conclusions regarding the design and performance of a precision attitude control system for a symmetric spinning body are summarized in Section A. Recommendations for further research are presented in Section B.

A. Conclusions

1. Design of Precision Attitude Controllers for Spinning Vehicles

An attitude controller that includes an automatic system to trim sensor-vehicle misalignments and body-fixed moments was developed. The Frequency Symmetry technique used to synthesize the attitude controller was shown to produce results equivalent to the classical gyrost design approach. Employing a root-locus analysis combined with the Frequency Symmetry technique, the design criteria for an Automatic Mass Trim System were investigated. Because the trim system, operating alone, was found to be unstable, an attitude control loop was required to maintain stability.

Control torque saturation nonlinearities were used to model the CMG characteristics and led to regions of instability not previously found in the linear system. Gain adjustments in the AMTS, verified by root-locus analysis and analog simulation, were required to stabilize the nonlinear controller.

2. Laboratory Performance of the Control System

Performance of an experimental control system, studied using the Spinning Vehicle Simulator, indicated that the laboratory environment was a major factor in limiting pointing accuracy. Careful trimming of the SVS was necessary to minimize torques created by center-of-mass/center-of-support separation. The effects of the air bearing and the rotation of the earth produced additional disturbing moments. Combined

with the noise generated by the autocollimator and the electronics, these sources limited the control system to a precision of ± 2.5 arc seconds.

The AMTS was found to be necessary for arc-second pointing accuracy in the laboratory. The changing mass of the vehicle, caused by gas expulsion from the spin and CMG unload jets, resulted in a time-dependent body-fixed moment that was impossible to trim manually. This moment was found to result in a 3 arc-second/min drift if the AMTS were not operating.

B. Recommendations

1. Improvements in Existing Techniques and Equipment

There are four main components which, with moderate improvement, would substantially better simulator performance.

- (a) A higher capacity CMG: Larger maximum torque and $|\vec{h}|$ would permit better steady-state and AMTS performance and longer time between gyro unload cycles.
- (b) Higher resolution lower noise equivalent-angle auto-collimator: A chopper-stabilized quad photomultiplier tube instead of the phototransistor sensor is a possible solution.
- (c) Improved air bearing: Present air-bearing technology can produce a bearing with only 10 or 20 percent of the torques observed with the bearing now in use [22]. However, the improvement here should be made with the addition of the following item.
- (d) An accurate coordinate transformer: The ability to observe attitude-error and spin-axis motion in laboratory coordinates yields the magnitude and direction of disturbing torques. Trimming with mirror and bearing adjustments is then possible.

2. Areas for Further Investigation

Operation of the simulator in a nonvertical position with automatic common-mode mass trimming is an important experimental and theoretical area of investigation, and it includes the design of

Contrails

appropriate control laws and/or state estimator. In addition, instrumentation of the trim system to telemeter the position of at least one trim mass would be desirable.

State estimation as a technique to obtain error rates and to estimate the apparent misalignment of the maximum axis and the autocollimator could be useful to eliminate the AMTS entirely. By electronically biasing the autocollimator output, as is effectively done in the analog simulation, the offset caused by misalignments and body-fixed moments would disappear.

Another form of AMTS in which the autocollimator is gimbaled to mechanically eliminate the offset is also a possibility. It is no more complex than the present system, and it's light weight would be attractive in a flight vehicle.

Contracts

Appendix

SPECIFICATIONS OF THE SPINNING VEHICLE SIMULATOR

A. Vehicle Specifications

Diameter	53.25 cm
Height	25.4 cm
Cone Height	14.0 cm
Mass	
frame	15.9 kg
trim system	25.0
trim weight	14.5
gyro	4.1
electronics rack	3.6
batteries	13.7
nitrogen tanks	23.6
miscellaneous	<u>11.4</u>
	111.8 kg

Moments of Inertia

$$I_s = 18.7 \times 10^7 \text{ gm-cm}^2$$

$$I_t = 10.4 \times 10^7 \text{ gm-cm}^2$$

$$(I_{xx} = 10.34 \times 10^7$$

$$I_{yy} = 10.41 \times 10^7)$$

$$\left. \begin{aligned} m &= \frac{I_s - I_t}{I_t} = 0.804 \\ n &= \frac{I_s}{I_t} = 1.804 \end{aligned} \right\} m + 1 = n$$

$$\beta = 1 \text{ rad/sec}$$

Air Bearing

sphere diameter	12.7 cm
operating gap	0.05 mm
supply pressure	3.2 atm

B. Kearfott T4101--C704101 Vertical Gyroscope Specifications

Diameter	13 cm
Height	16.1 cm
Mass	4.1 kg
Power Requirements	
motor starting	25 W
motor running	6 W
torquers	26 W each, max
synchros	4.5 W each
Amplifier Efficiency	50%
Synchro Scale Factor	206 mV/deg
Torquer Scale Factor	1.55×10^3 dyne-cm/V
Maximum Torquer Output	17.84×10^4 dyne cm
Degrees of Freedom	
pitch	$\pm 85^\circ$
roll	360°
Free Drift	0.005 rad/min
Angular Momentum	
wheel speed	2.5×10^3 rad/sec
$ \vec{H} $	8.5×10^6 gm-cm ² /sec
Moments of Inertia	
I_{IGx}	4750 gm-cm ²
I_{IGy}	6090
I_{IGz}	3550
I_{OGx}	4070
I_{OGy}	3750

I_{OGz}	4440
I_{wt}	860
I_{ws}	3400

C. Pneumatic System

1. Specifications

Maximum Thrust

spin jet	8.73×10^3 dyne
low-thrust jets	1.89×10^3 (average)
high-thrust jet	8.90×10^5

Valve Characteristics

power required	6 W each
minimum pulse	20 msec
maximum pressure	5.1 atm
operating pressure	3.26 atm

Tanks

volume	10.32 liters each at STP
maximum design pressure	136 atm
operating pressure	100 atm

2. Control Jet Calibration

To reduce the net moment applied to the vehicle during CMG momentum dumping, a technique was developed to calibrate jet thrust and gyro-torquer output. In addition, this method allowed the moment caused by bearing-cup tilt to be measured.

The procedure requires that the spin jet be turned off, the cross-coupling terms in the control law be disconnected, and the vehicle be trimmed carefully. By operating with automatic mode sequencing, the simulator will attempt to null the autocollimator signal as it cycles between modes 4 and 5.

In mode 4, the torques applied to the vehicle are

Contrails

$$I_t \ddot{\gamma}_x = 0 = M_{gx} + M_{bx} + M_{Cx4}$$

$$I_t \ddot{\gamma}_y = 0 = M_{gy} + M_{by} + M_{Cy4}$$

Torques applied to the gyro are

$$M_{Cx4} = h \dot{\delta}_{y4}$$

$$M_{Cy4} = -h \dot{\delta}_{x4}$$

The mode is indicated by the subscript.

In mode 5,

$$I_t \ddot{\gamma}_x = 0 = M_{gx} + M_{bx} + M_{Cx5} - M_{Jy} + M_{Ux}$$

$$I_t \ddot{\gamma}_y = 0 = M_{gy} + M_{by} + M_{Cy5} - M_{Jx} + M_{Uy}$$

and

$$M_{Ux} + M_{Cx5} = h \dot{\delta}_{y5} \quad M_{Ux} = -G_p \delta_y$$

$$M_{Uy} + M_{Cy5} = -h \dot{\delta}_{x5} \quad M_{Uy} = G_p \delta_x$$

Thus,

$$M_g + M_b = -M_{C4}$$

and

$$M_g + M_b = -M_{C5} + M_J - M_U$$

Therefore,

$$(M_{C5} + M_U) - M_{C4} = M_J$$

Contrails

which can be obtained from

$$h(\dot{\delta}_5 - \dot{\delta}_4) = M_J$$

If the vehicle is rotated π radians and mode 4 readings are compared,

$$0 = M_g + M_b + M_{C4_0}$$

$$0 = M_g - M_b + M_{C4_\pi}$$

then

$$M_g = \frac{-\left(M_{C4_\pi} + M_{C4_0}\right)}{2}$$

and

$$M_b = \frac{M_{C4_\pi} - M_{C4_0}}{2}$$

The gravity and bearing moments are calculated from the gyro gimbal-angle rates as before:

$$-\frac{h}{2} \left(\dot{\delta}_{4_\pi} + \dot{\delta}_{4_0} \right) = M_g$$

$$\frac{h}{2} \left(\dot{\delta}_{4_\pi} - \dot{\delta}_{4_0} \right) = M_b$$

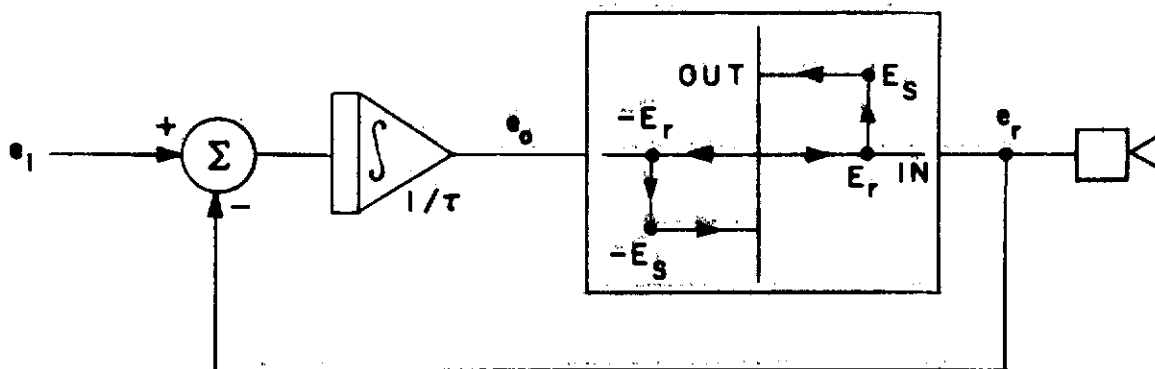
The unload torque applied by the torquers along the + and - directions of both axes can be controlled individually. After the torque for each jet has been measured, the gyro is adjusted until each torquer produces the correct $\dot{\delta}$:

<u>Moment due to</u>	<u>Moment</u>
+X axis jet	8.14×10^4 dyne cm
-X axis jet	9.56×10^4
+Y axis jet	10.0×10^4
-Y axis jet	10.2×10^4

3. Pulse-Width/Pulse-Frequency Modulator

To obtain a force linearly proportional to the control signal by using a valve that is either closed or fully open, some type of modulation scheme must be employed. The technique used on the SVS is PVPF modulation and was chosen for its simplicity.

The modulator, illustrated in the schematic below, consists of a Schmitt trigger and an integrator. The analog input increases the integrator output until it exceeds the Schmitt trigger ON threshold. The fixed-magnitude trigger output fires the valve and resets the integrator. The trigger remains in the ON state until the integrator output returns to zero.



- | | |
|--|--|
| $e_i \triangleq$ input signal | $E_s \triangleq$ trigger pulse magnitude |
| $1/\tau \triangleq$ integrator time constant | $e_r \triangleq$ trigger output |
| $E_T \triangleq$ trigger ON threshold | |

The average value of the Schmitt trigger output \tilde{E} is

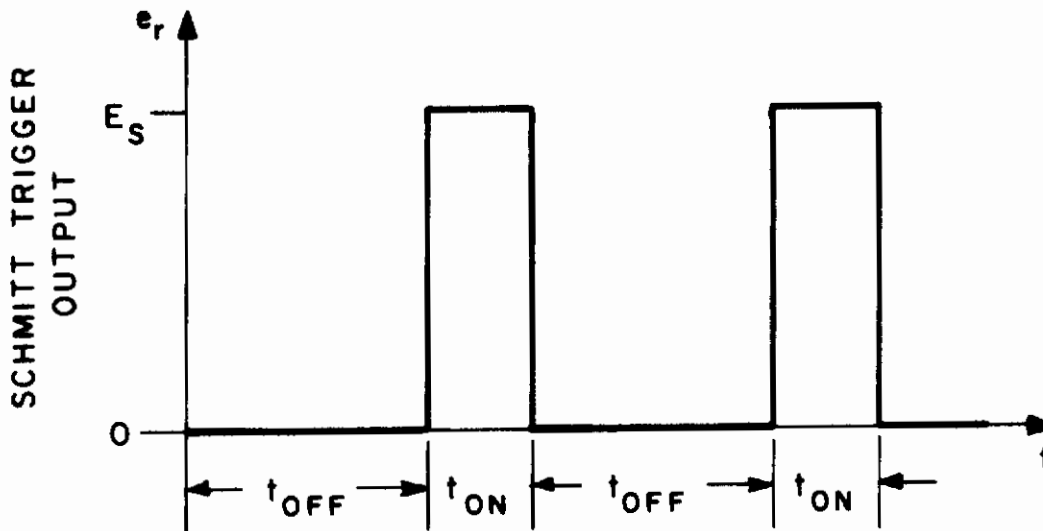
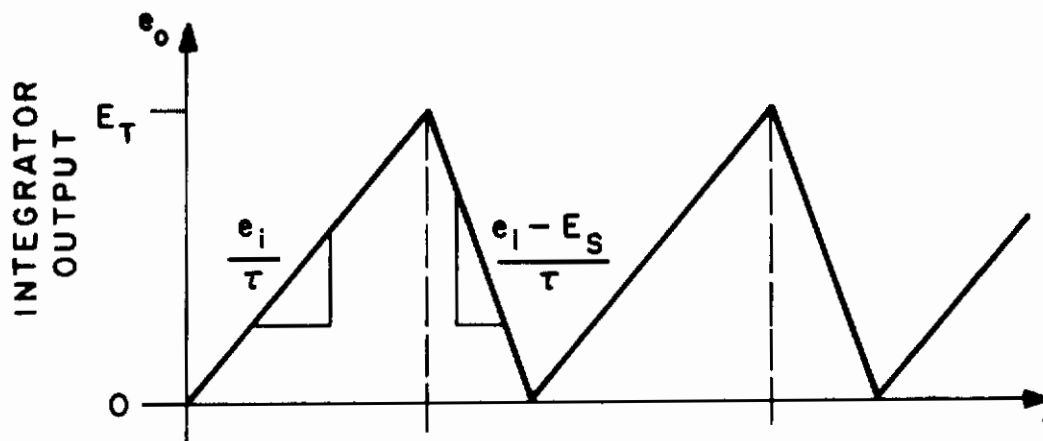
Contrails

$$\tilde{E} = \frac{E_s t_{ON}}{t_{ON} + t_{OFF}}$$

Because the frequency ν is $1/(t_{ON} + t_{OFF})$ and the pulse width W is $W \triangleq t_{ON}$, the average output is

$$\tilde{E} = E_s W \nu$$

The response of the modulator to a constant input is shown below.



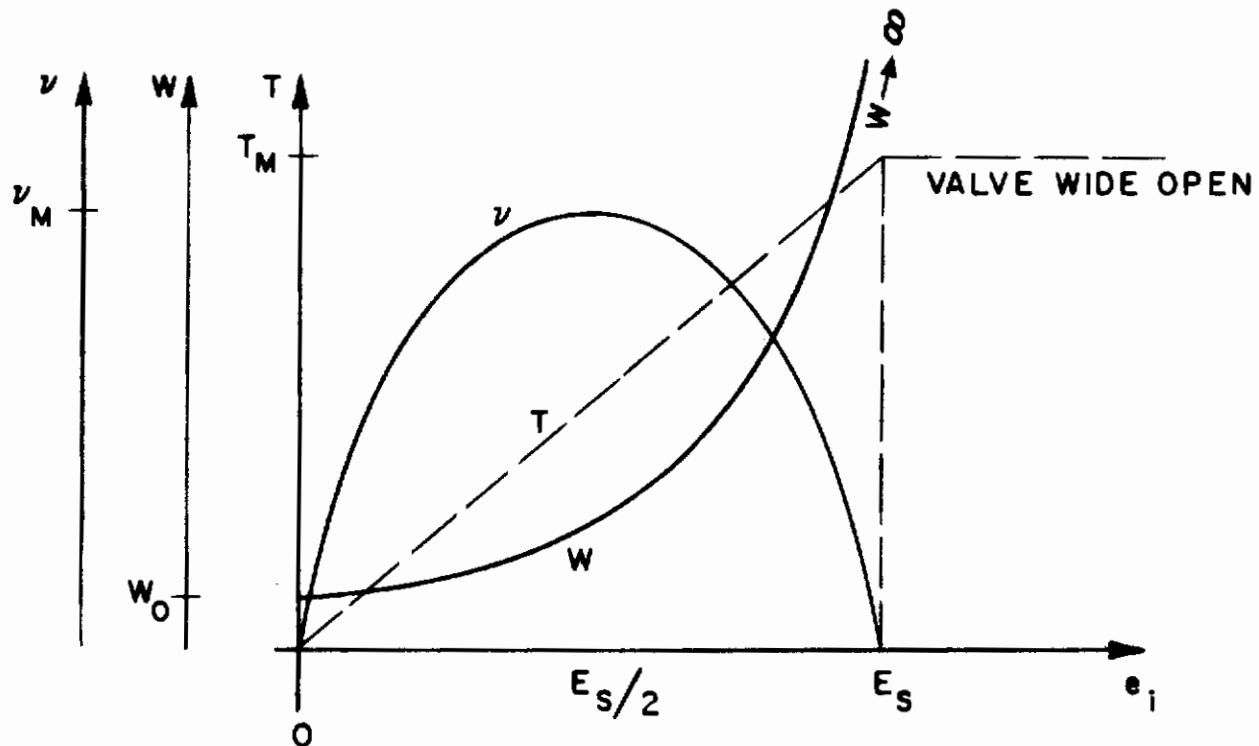
$$\left. \begin{aligned} \nu &= \frac{1}{(\tau E_T / e_i) - [\tau E_T / (e_i - E_s)]} \\ W &= \frac{-\tau E_T}{e_i - E_s} \end{aligned} \right\} \text{therefore, } \tilde{E} = \frac{-[(e_i - E_s)^{-1} E_s]}{[(e_i - E_s - e_i) / (e_i - E_s)]}$$

Contrails

and $\tilde{E} = e_i$, or the average output is linear with the input. The graph below shows how W , v , and thrust vary with the input e_i :

$$W = \frac{\tau E_T}{(E_S - e_i)} \quad v = \frac{e_i E_S - e_i^2}{\tau E_T E_S} \quad T = K_T \tilde{E}$$

where $K_T \triangleq$ scale factor.



$$v_m = \frac{E_S}{4\tau E_T} \quad W_o = \frac{\tau E_T}{E_S} \quad T_m = K_T E_S$$

D. Auxiliary Equipment

1. External Control Box

The external control box (Fig. 43) performs the following functions.

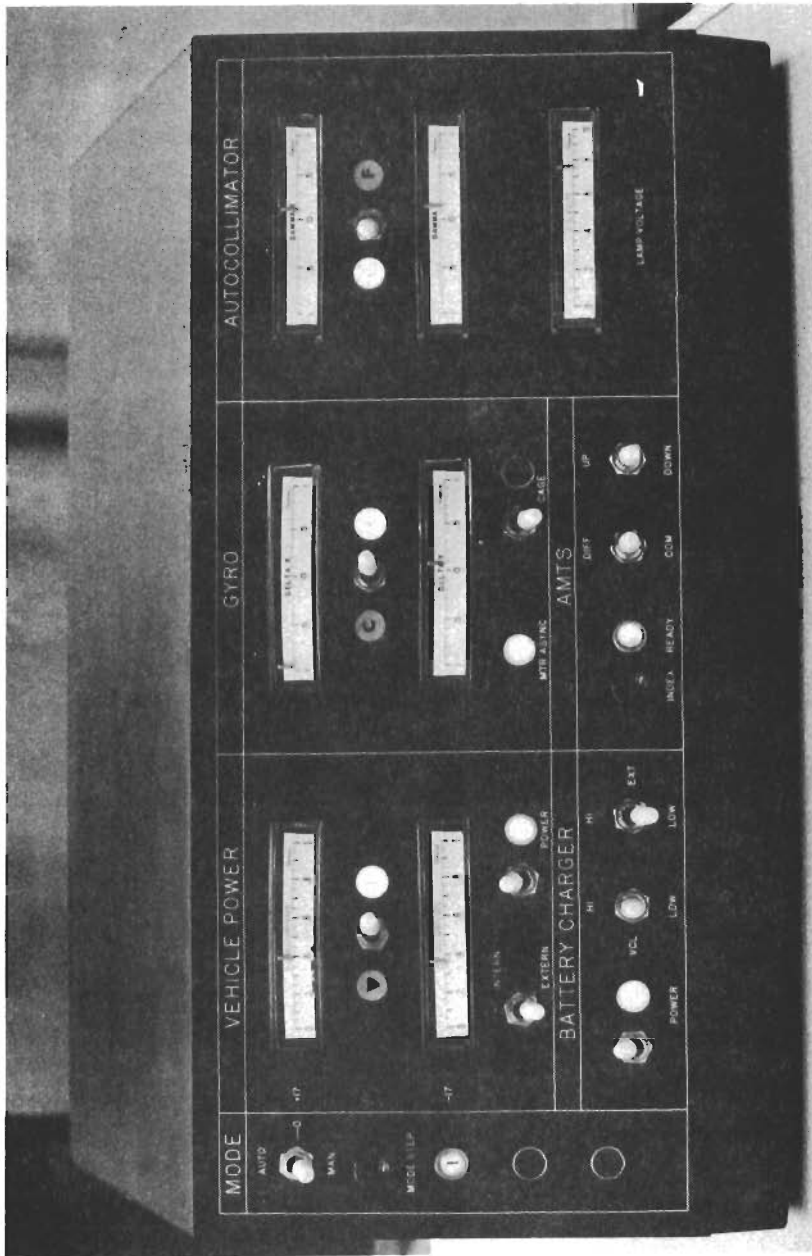


Fig. 43. EXTERNAL CONTROL BOX.

Contrails

- External Power: power on-off, external or internal power select, battery charger power, and high-low charge rate select
- Control:
 - Mode Control: auto, manual or mode 0, manual mode step or automatic sequencing, mode step command
 - AMTS Control: mass position index, mass motion differential or common mode, mass motion up or down
- Display:
 - Lamps: mode number, gyro motor running asynchronously, AMTS indexed, external power supply on, battery charger on
 - Meters: power supply (external or internal) voltage and current, autocollimator angles, autocollimator lamp voltage, gyro gimbal angles

The vehicle is prepared for an experimental run, using external power in mode 0. After the gyro is up to speed and the autocollimator and gyro are aligned, the run is started from the control box. Mode 1 automatic is selected, the vehicle is switched to internal power, and the external control cable is disconnected.

2. Reference Mirror and Vehicle Stand

The autocollimator reflects light off a 5 cm optical flat mounted on a two-axis gimbal in the laboratory. The adjustment of the gimbals is controlled by two micrometer screws. A bubble level which can be rotated 360° is fixed to a flat plate resting on the upper surface of the mirror. By comparing the bubble position on 180° rotations of the level, the mirror can be adjusted to the local horizontal within 0.01 rad in each axis. As previously discussed, this is important in minimizing gravitational disturbing moments.

When not in use, the SVS is supported by four arms that contact it at each AMTS unit location. The stand and vehicle can be raised or lowered by using a large lead screw; thus, the bearing is protected from accidental bumping or gouging by foreign particles. The arms are lowered to a position that does not interfere with attitude motion during operation.

To align the autocollimator and gyro with the reference mirror, two micrometer screws and two spring-loaded tips are provided on the support arms. The vehicle, supported by the air bearing, is pushed against the micrometer screw by the spring load on the opposite arm. Alignment is performed by adjusting the screws and observing the control-box autocollimator meters.

E. Electronics

1. Gyro Power Amplifier

The gyro amplifier is divided into three sections: one for wheel motor, synchro excitation, and torquer fixed phase, and one each for the two torquer variable-phase inputs. The first two sections (A and B) are identical and amplify the modulator output to drive the X- and Y-axis torque motors; the power-amplifier output varies between 0 and 115 Vac at 400 Hz. The output transformer of the third section (C) has taps at 115, 57.5, and 28 V, which are used for motor drive, torquer fixed phase, and synchro excitation, respectively; this section input is a 400 Hz square wave generated by the precision time base.

In addition, a current-measuring circuit is included to determine if the wheel motor is running at synchronous speed. The sequencing logic disables the torquer inputs unless the wheel is running synchronously, thereby preventing torques from being applied to a de-spun gyro. A panel light indicates when the motor is asynchronous.

The amplifier is located next to the gyro, rather than in the same bay as the control electronics. Heat, electronic noise from the high currents, and lack of space for the bulky transformers and heat sinks were reasons for selecting this location.

2. Control Panel

All simulator control-system components are operated from a panel (Fig. 44) located in a well just under the upper skin. Lights display the state of the controller and indicate if the system is functioning properly. This panel contains the following features.

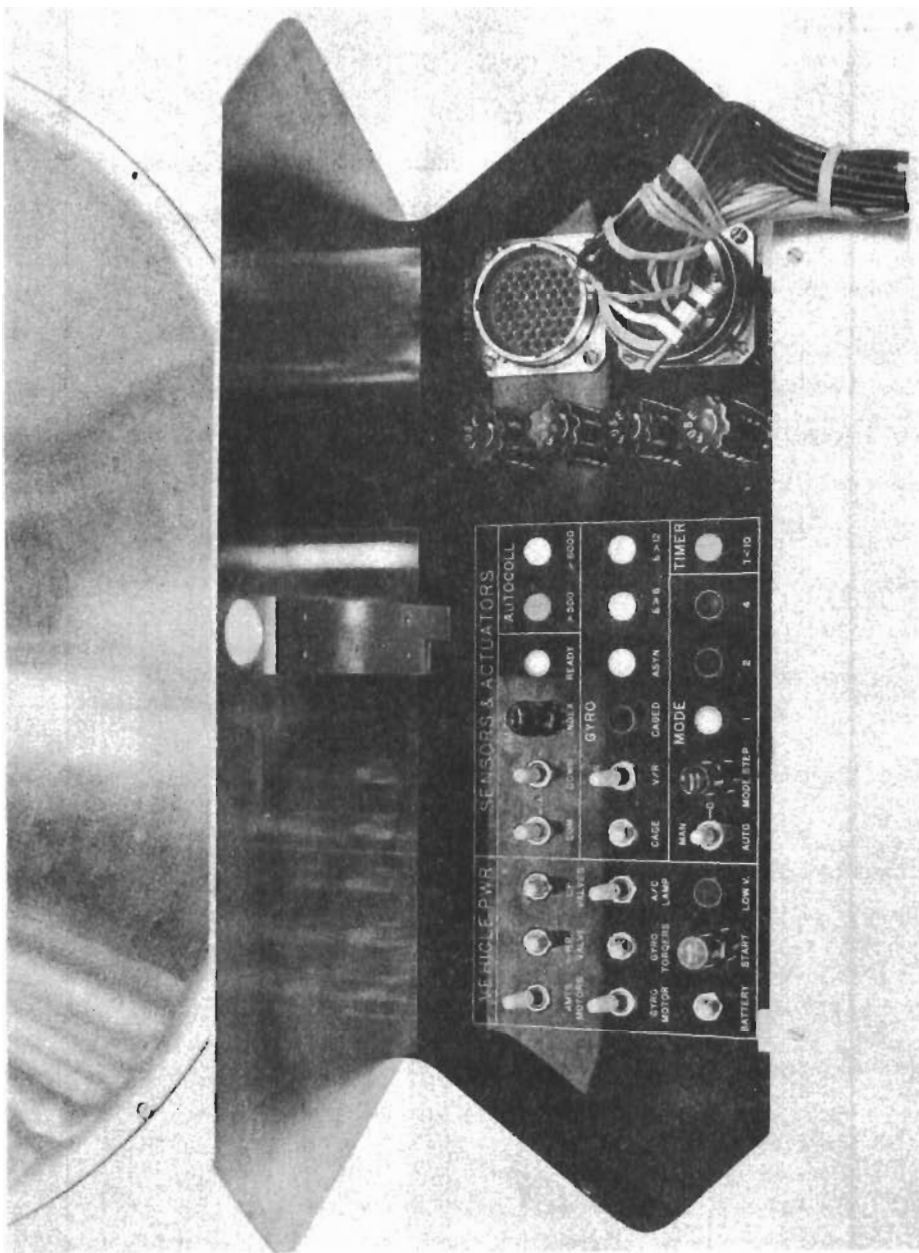


Fig. 44. VEHICLE CONTROL PANEL.

Contrails

- On-Off Switches: high- and low-thrust jets, AMTS motors, gyro motor and torquers, battery, and autocollimator lamp
- AMTS Control: mass motion common mode or differential, mass motion up or down, and index command
- Gyro Control: synchro or vertical reference select and cage command
- Mode Control: manual, automatic or mode 0 select, and manual mode step command
- Indicator Lamps: AMTS indexed, autocollimator >500 arc seconds and >6000 arc seconds, gyro motor asynchronous, gyro caged, synchros >6° and >12°, mode number, timer <10 seconds, and battery undervoltage
- 52-pin test-point connector
- 52-pin external-control connector
- Two 10 A fuses for the ±17 V batteries
- Two 2 A fuses for electronics rack

3. Telemetry

The data-telemetry system consists of four principal parts. On board, there are five V-to-F converters and an AM transmitter. Located just below the vehicle on the pedestal, there are five AM receivers and F-to-V converters with a common power supply. The V-to-F converters are in the electronics rack and are connected easily to any signal to be telemetered. The modulator (AM transmitter) is connected by cable to the rack and is located just below the control well. A loop antenna is fixed parallel to the vehicle bottom.

The system contains five data channels and operates by producing an audio tone whose frequency is proportional to the analog input. The FM range is 1 to 2 kHz, corresponding to -10 and +10 V, respectively. This tone amplitude-modulates a carrier frequency in the AM broadcast band. Five commercial AM receivers, each tuned to one of the carrier frequencies, reconvert the signals to audio tones; F-to-V converters reconstruct the original analog signal. Because frequencies encountered in simulator operation never exceed 2 Hz, minimum distortion occurs in the modulation-demodulation process.

Calibration and zeroing are performed by the common-mode differential switch on the control panel. The switch positions not only change the AMTS functions, but they switch 1 and 2 kHz tones to all channels. Gain and zero pots on the F-to-V converters provide the necessary adjustments.

Telemetry range is approximately 3 m; the close proximity of the antenna and receivers blocks commercial AM stations. The harmonics from the five carrier frequencies are severe enough so that any additional channels are interfered with and unusable.

4. Controller Mechanization

Table 3 lists the notation for the sequencing-logic flow chart shown in Fig. 45. The logic diagram is derived from the switching criteria discussed earlier (see Table 1) and is implemented on card 7, using integrated-circuit logic components.

Details of the controller (including scale factors, intercard connections, transfer functions, and mode switching) are presented in Figs. 46-49. Each figure shows the control loops associated with one of the actuators; Figs. 24-28 (shown earlier) are block diagrams for each of the loops.

Table 3

NOTATION FOR SEQUENCING LOGIC

Notation	Definition
A	automatic mode sequencing
M	manual mode sequencing
	} switch position
CA	manual command for a mode advance
I	M <u>and</u> CA = incremental mode pulse
STY	60 sec (or 120 in mode 1) since last reset of timer (see RESET 60)
S12	angle of $>12^\circ$ on at least one synchro
S6	angle of $>6^\circ$ on at least one synchro
S 1/4	angle of $>0.25^\circ$ on at least one synchro
M_i	mode i
LAMPMAX	autocollimator lamp voltage at max value (>6000 arc seconds)
AC500	autocollimator output >500 arc seconds on at least one channel
RESET 60	reset of the 60 sec timer; STY appears 60 sec after last RESET 60 input
\dot{M}_i	start of mode i
RESET 60	\dot{M}_1 <u>or</u> \dot{M}_2 <u>or</u> \dot{M}_3 <u>or</u> (M_2 <u>and</u> LAMPMAX) <u>or</u> (M_3 <u>and</u> AC500)

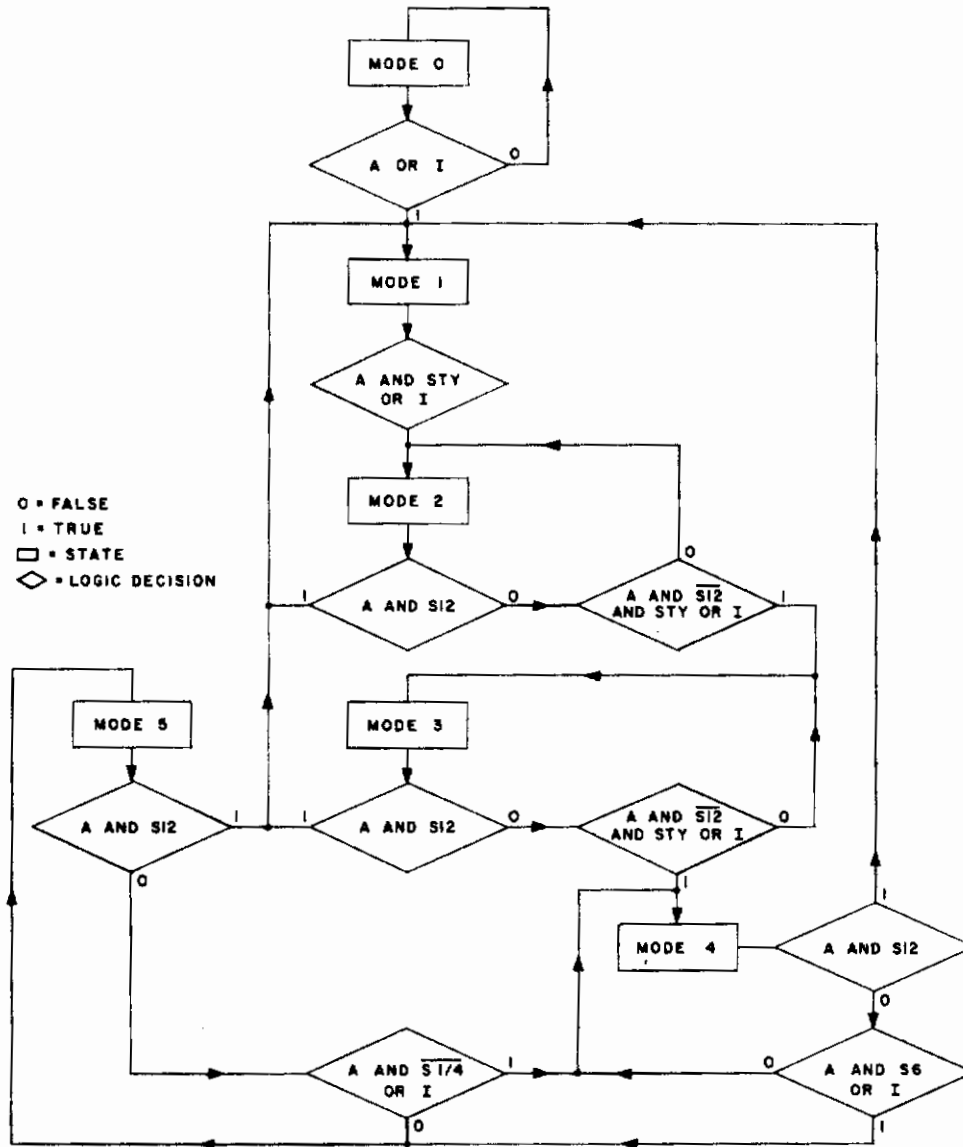
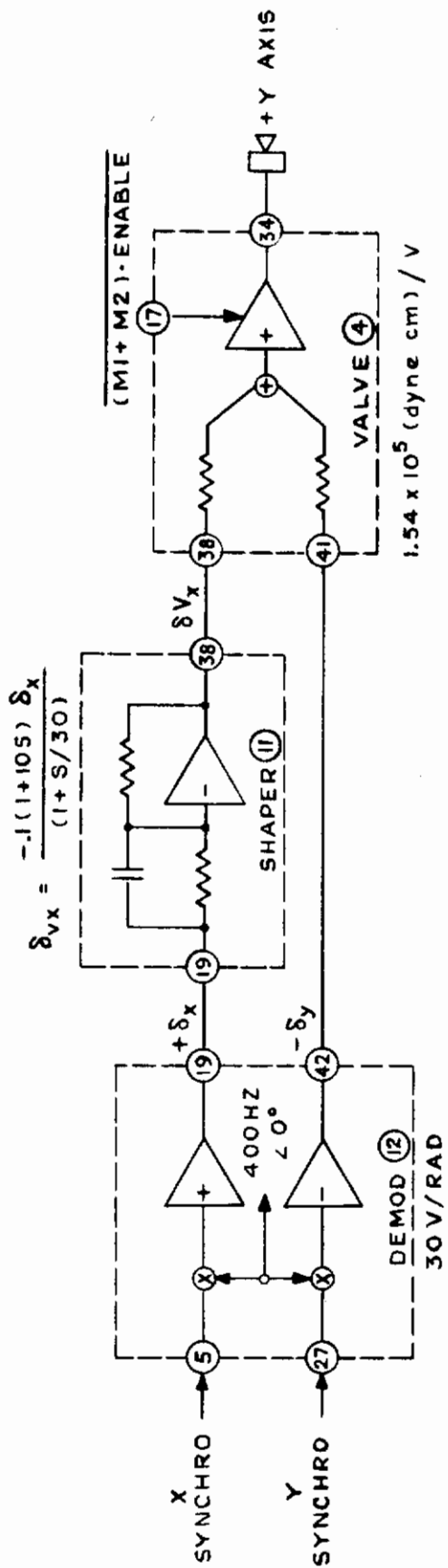


Fig. 45. SEQUENCING LOGIC.



$$\delta_{Vx} = \frac{-j(1+10s)\delta_x}{(1+s/30)}$$

1.54×10^5 (dyne cm) / V

LEGEND FOR MECHANIZATION FIGURES

- (4) CARD PIN NUMBER
- (7) CARD NUMBER
- (+) SUMMATION
- (X) MULTIPLICATION
- (M1+M2)-ENABLE "SEQUENCING LOGIC INPUT"
- (11) SHAPER
- (12) DEMOD
- (17) (M1+M2)-ENABLE
- (19) SUMMATION
- (36) SUMMATION
- (38) SHAPER
- (41) VALVE & JET
- (4) VALVE & JET
- (5) X SYNCHRO
- (27) Y SYNCHRO
- (42) SUMMATION
- (4) VALVE & JET
- (17) (M1+M2)-ENABLE
- (36) SUMMATION
- (38) SHAPER
- (41) VALVE & JET
- (4) VALVE & JET

Fig. 46. HIGH-THRUST LOOP.

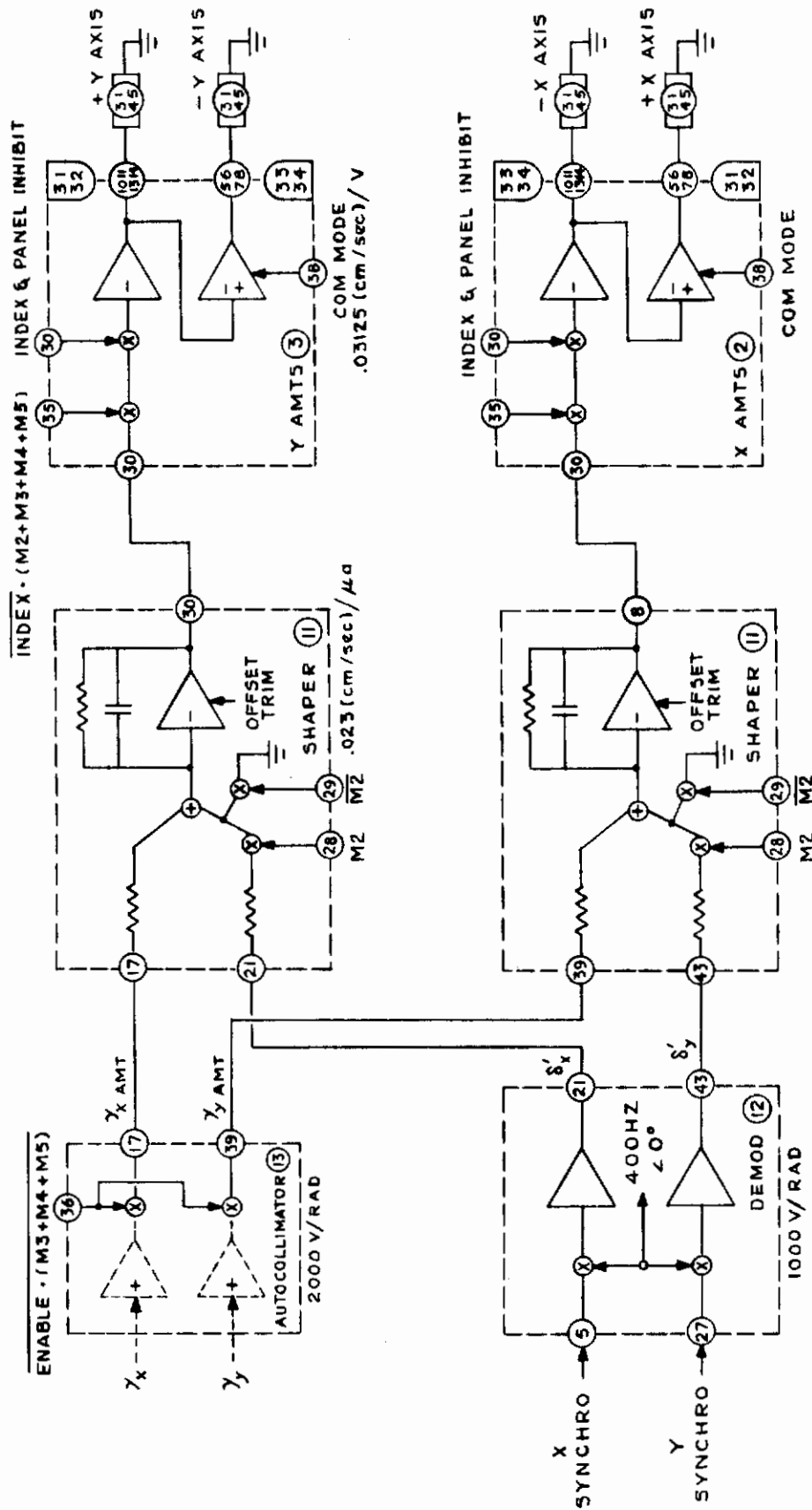


Fig. 47. AMTS LOOPS.

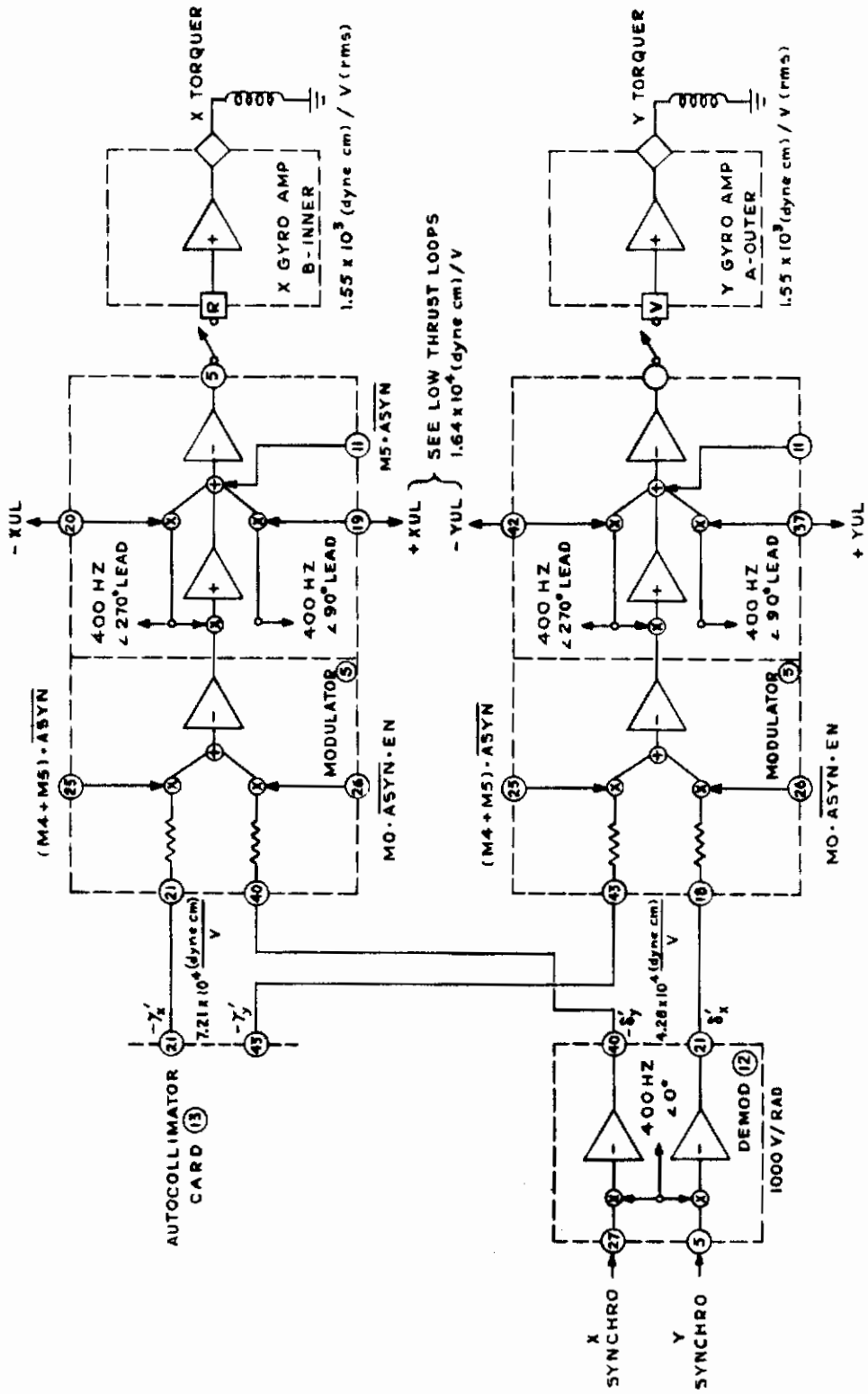


Fig. 49. GYRO LOOPS.

REFERENCES

1. B. O. Lange, "The Control and Use of Drag-Free Satellites," SUDAER No. 194, Stanford University, Stanford, Calif., Jun 1964.
2. "Final Engineering Report on the First Phase of a Continuing Program of Advanced Research in Guidance, Control, and Instrumentation," Contract No. AF33(615)-1411, Research and Technology Division of the Air Force Systems Command, and the Guidance and Control Laboratory, Stanford University, Stanford, Calif., Jan 1967.
3. R. D. Cole, M. E. Ekstrand, and M. R. O'Neil, "Attitude Control of Rotating Satellites," ARS Journal, Oct 1961, pp. 1446-1447.
4. T. R. Kane and P. M. Barba, "Attitude Stability of a Spinning Satellite in an Elliptic Orbit," Western Conference of the Applied Mechanics Division, Los Angeles, Calif., 1965.
5. Frank B. Wallace, Jr. and Leonard Meirovitch, "Attitude Instability Regions of a Symmetric Spinning Satellite in an Elliptic Orbit," presented at the 5th Annual AIAA Aerospace Sciences Meeting, New York, Jan 1967.
6. W. G. Hughes, "Attitude Control: Spin Stabilization," ESRO Spacecraft Technology, 11, Jul 1966.
7. B. O. Lange, A. W. Fleming, and B. W. Parkinson, "A Special Technique for Spinning Vehicle Control Synthesis," SUDAAR No. 249, Stanford University, Stanford, Calif., Mar 1966.
8. D. L. Mingori and T. R. Kane, "The Attitude Stabilization of Rotating Satellites by Means of Gyroscopic Devices," J. of the Astronautical Sciences, Jul-Aug 1967, pp. 158-166.
9. K. T. Chang and G. W. Yarber, "Application of Control Moment Gyros to Stabilization and Attitude Control in Space," presented at the 1st National Conference on Space Maintenance and Extra Vehicular Activities, Orlando, Fla., Mar 1966.
10. A. Dean Jacot and Donald J. Liska, "Control Moment Gyros in Attitude Control," J. Spacecraft and Rockets, Sep 1966, pp. 1313-1320.
11. John A. Sorenson, "Precision Magnetic Attitude Control of Spinning Spacecraft," SUDAAR No. 380, Stanford University, Stanford, Calif., Aug 1969.
12. J. J. Adams, "Study of an Active Control System for a Spinning Body," NASA Technical Note D-905, Langley Research Center, Langley Field, Va., Jun 1961.
13. Peter R. Kurzhals and James J. Adams, "Dynamics and Stabilization of the Rotating Space Station," Astronautics, Sep 1962, pp. 25-29.

14. John J. Fearnside, "Use of Control Moment Gyros for the Stabilization of Spinning Spacecraft," AIAA Journal, 8, Jul 1970, pp. 1365-1366.
15. A. J. Sarnecki, "An Automatic Attitude Control System for a Spinning Satellite: A Theoretical Assessment," Royal Aircraft Establishment Technical Report No. RAE-TR-66368, Nov 1966.
16. P. C. Wheeler, "Magnetic Attitude Control of Rigid Axially Symmetric Spinning Satellites in Circular Earth Orbits," SUDAAR No. 244, Stanford University, Stanford, Calif., Apr 1965.
17. J. J. Adams, "Simulator Study of an Active Control System for a Spinning Body," NASA Technical Note D-1515, Langley Research Center, Langley Field, Va., Dec 1962.
18. L. C. Rossi, R. Ghigliazza, and R. C. Michelini, "A Simplified Analytical Approach and Analog Simulation Results for the Attitude Perturbed Dynamics of a Spinning Satellite," Sciences et Industries Spatiales, 5, 5-6, 1969, pp. 21-30.
19. T. R. Kane and D. Sobala, "A New Method for Attitude Stabilization," AIAA Journal, 1, 6, Jun 1963, pp. 1365-1367.
20. Rinaldo C. Michelini, Alermo Lucifredi, and Dino Dini, "The Dynamics of a Non-Rigid Spinning Satellite Containing Oscillating Liquids," presented at 3rd Symposium on Automatic Control, International Federation of Automatic Control, Toulouse, France, Mar 1970.
21. W. H. Munk and G. J. F. MacDonald, The Rotation of the Earth, Cambridge University Press, N.Y., 1960.
22. Bunji Tomita, Kenichi Suzuki, Kuniyoshi Minami, Tadami Iwata, and Toshio Kawakara, "On the Spacecraft Simulator," Institute of Space and Aeronautical Science Bulletin, Tokyo University, Tokyo, Japan, 6, Apr 1970, pp. 404-415.

ADDITIONAL BIBLIOGRAPHY

Cannon, Robert H., Jr., Dynamics of Physical Systems, McGraw-Hill Book Co., N.Y., 1967.

"Final Engineering Report on a Continuing Program of Advanced Research in Guidance, Control, and Instrumentation," Contract No. AF33615-67-C-1245, Research and Technology Div. of the Air Force Systems Command, and the Guidance and Control Laboratory, Stanford University, Stanford, Calif., Apr 1970.

Contrails

- Fleming, Alan W., "Use of the Properties of Frequency Symmetry and Complex Symmetry in the Control of Linear Dynamical Systems," SUDAAR No. 266, Stanford University, Stanford, Calif., May 1966.
- Freed, L. E., "Attitude Control System for a Spinning Body," ARS Journal, Mar 1962, pp. 396-401.
- Goldstein, Herbert, Classical Mechanics, Addison-Wesley Publishing Co., Inc., Reading, Mass., 1959.
- Liska, Donald J., "A Two Degree of Freedom Control Moment Gyro for High Accuracy Attitude Control," J. of Spacecraft and Rockets, 5, 1, Jan 1968.
- Schlichting, Hermann, Boundary Layer Theory, McGraw-Hill Book Co., N.Y., 1960.

Contrails

UNCLASSIFIED

Security Classification

DOCUMENT CONTROL DATA - R & D

(Security classification of title, body of abstract and indexing annotation must be entered when the overall report is classified)

1. ORIGINATING ACTIVITY (Corporate author) Department of Aeronautics and Astronautics Stanford University Stanford, California 94305	2a. REPORT SECURITY CLASSIFICATION Unclassified
	2b. GROUP

3. REPORT TITLE
PRECISION ATTITUDE CONTROL OF SYMMETRIC SPINNING BODIES

4. DESCRIPTIVE NOTES (Type of report and inclusive dates)
SUDAAR No. 422, April 1971

5. AUTHOR(S) (First name, middle initial, last name)
Kenneth R. Lorell, Benjamin Lange

6. REPORT DATE April 1971	7a. TOTAL NO. OF PAGES 127	7b. NO. OF REFS 29
------------------------------	-------------------------------	-----------------------

8a. CONTRACT OR GRANT NO. F33615-70-C-1637 b. PROJECT NO. c. Task 510215 d.	9a. ORIGINATOR'S REPORT NUMBER(S) SUDAAR No. 422
	9b. OTHER REPORT NO(S) (Any other numbers that may be assigned this report) AFAL-TR-71-224

10. DISTRIBUTION STATEMENT
Approved for public release; distribution unlimited

11. SUPPLEMENTARY NOTES	12. SPONSORING MILITARY ACTIVITY United States Air Force Air Force Avionics Laboratory Wright-Patterson AFB, Ohio 45433
-------------------------	--

13. ABSTRACT

Motivated by the arc-second pointing requirement of the Unsupported Gyroscope experiment and other satellite applications, this research investigates the problems associated with the precision attitude control of symmetric spinning bodies. An attitude control system is synthesized and then is studied by analog simulation. Controller performance and limitations are evaluated, using a laboratory model called the Spinning Vehicle Simulator (SVS).

A technique devised at Stanford University in 1966 that simplifies the design of spinning-vehicle attitude controllers is used to select controller gains. The resulting system, simulated on an analog computer, produces excellent response characteristics and is insensitive to vehicle parameter or gain changes. The magnitude of the attitude error is shown to have zero-frequency and spin-frequency components proportional to the magnitude of body-fixed and inertially fixed moments, respectively.

An Automatic Mass Trim System (AMTS), consisting of two pairs of masses that move on axes parallel to the nominal spin axis, is proposed as a means of eliminating zero-frequency attitude errors caused by moments fixed in the body and sensor-vehicle misalignments. By correctly positioning the trim masses, a moment (or a product of inertia) is created to compensate for the disturbance (or misalignment). The equations of motion for a spinning rigid body with internal moving masses are developed and used to analyze the trim system. A series of root loci, plotted for the attitude-stabilized vehicle with an AMTS, is the basis for trim-system gain selection. (Continued on next page.)

14 KEY WORDS	LINK A		LINK B		LINK C	
	ROLE	WT	ROLE	WT	ROLE	WT
SPINNING VEHICLE PRECISION ATTITUDE CONTROL AUTOMATIC MASS TRIMMING CONTROL MOMENT GYRO						
<u>ABSTRACT (Continued)</u> The laboratory portion of the investigation deals with two problems: first, mechanization of the attitude controller and AMTS and second, determination of those factors that limit control-system performance. A spinning-vehicle attitude controller on a three-degree-of-freedom spherical air bearing was developed, which damps large initial conditions, acquires a laboratory reference mirror (for the autocollimator used as an attitude sensor), maintains precision attitude control during CMG momentum dumping, and automatically trims the effects of body-fixed moments and sensor-vehicle misalignments. The effects of sensor noise, electronic noise, and the laboratory environment on the control system were measured. A pointing accuracy of ± 2.5 arc seconds was achieved. An analysis of error sources indicates that the laboratory environment (including torques from gravity effects, air bearing, earth rate, and air currents) is the major factor in limiting the system. By extrapolating these results using previously developed disturbance torque models, the performance of a controller similar to that used on the SVS is predicted for the orbital environment.						